Investigation of Soot Formation by Optical Diagnostics: From Precursor Measurements to 3D Particle Sizing

Untersuchung der Rußbildung mittels optischer Messtechnik: Von Rußvorläufer-Messungen bis zur 3D Partikelgrößenbestimmung

Der Technischen Fakultät
der Friedrich-Alexander-Universität
Erlangen-Nürnberg

zur
Erlangung des Doktorgrades Dr.-Ing.

vorgelegt von
Florian Jakob Bauer
aus Augsburg

Als Dissertation genehmigt
von der Technischen Fakultät
der Friedrich-Alexander-Universität Erlangen-Nürnberg

Tag der mündlichen Prüfung:	**07.12.2022**
Gutachter:	**Prof. Dr.-Ing. Stefan Will**
	Prof. Dr. Per-Erik Bengtsson

Acknowledgement

Based on the assumption that these words write easiest after finishing the last sentences of the thesis I would like to express my gratitude to those who helped to make this possible. First, I want to thank my supervisor Stefan Will for giving me the opportunity and the trust to follow my research ideas. I would like to thank Professor Bengtsson for acting as a reviewer for this thesis. Next, I of course also want to thank Franz Huber, who first introduced me to LTT and was then an excellent group leader with an open ear towards any question, discussion and also smaller or larger obstacles. I had the pleasure to work with Professor Kyle Daun and Professor Weiwei Cai and want to thank them for sharing their tremendous expertise.

To all my dear colleagues: To avoid the impression of any form of ranking I want to stick to chronological order. I want to thank Julian Perlitz with whom I already spent my time in LTT's student room while writing our Master theses. Your generous support throughout any life situation from taking care of my plants, car, flat or current lab problem can hardly be expressed in a few lines. I want to thank Peter Fendt as my friend and office mate. Besides your support on IR absorption spectroscopy, I will never forget the millions of coffees, "Kaktuseis" and Club Mates we had together. I thank Sina Talebi Moghaddam for our shared lab time towards the beginning of my PhD - conducting LII and WALS measurements and learning jointly about the challenges related to reliable lab work. I want to thank Simon Aßmann for providing me with TEM images and sharing his knowledge on ELS as well as all the fun events we shared over the last years. I thank Markus Labus for his persistent support and the wonderful times at conferences in Dublin and Switzerland. Besides all my esteemed colleagues of "Partikelmesstechnik" I also want to thank Lars Zigan and his group. I thank Matthias Kögl and Ulrich Retzer, obviously for your research support but even more for all the fun times and ping pong matches we had. I thank Nikolas Schmidt and Jonas Bollmann for all the ongoing support in daily-institute life. I also want to address a big "Thank You" to Tao Yu with whom I shared a great time conducting the tomographic measurements. I wish you all the best towards your future research plans. I thank Phillipp Bräuer for every late-at-night discussion. Despite your "know-it-all" attitude, you are a tremendous support. I also want to thank Fabian Hagen from KIT for providing me with the HRTEM image. Most recently I want to thank Samuel Grauer for all the inspiring discussions and I am very happy regarding our joint work and look forward to upcoming research plans.

I especially want to thank all of the students: Nicola, Michael (twice), Maxi, Flo, Marius, Sebastian, Benni and Sebastian. Without your work, this thesis would not have been possible!

I finally want to thank my family and my girlfriend Franziska for your patience and understanding throughout the last years. This work is dedicated to you!

Abstract

Up to date, the soot evolution process during hydrocarbon combustion is not fully understood. This fact basically derives from the simultaneous interplay of numerous chemical reactions linked to rapid changes, complex physical processes such as heat and mass transfer or agglomeration, and a required size of observation in the nanometric down to the atomic scale. Laser diagnostics in many cases provide high temporal and spatial resolutions and are therefore ideal to provide insight into different stages of the soot evolution process.

In this work, the further development of two *in situ* diagnostic techniques is described. On the one hand, broadband absorption spectroscopy is applied to investigate the early stages of soot formation. Here, polycyclic aromatic hydrocarbons are considered as precursor molecules responsible for the nucleation and growth of solid soot particles. They reveal a characteristic absorption behaviour in the ultraviolet wavelength range. With the compilation of a database of the individual compounds and a simplified energetic model to account for the elevated flame temperatures, it becomes thus feasible to measure a possible species distribution *in situ*. The technique is further applied to observe changes in the optical properties linked to the maturity of soot particles. A change in the fine structural arrangement of the soot particles similar to graphitization tends to decrease the optical band gap value, which can be derived from broadband absorption measurements. Additionally, the type of transition is inferred from the measurements indicating towards an indirect allowed transition for mature soot particles.

On the other hand, time-resolved laser-induced incandescence allows to determine the size of soot primary particles. Here, one challenge derives from the fact that these primary particles cluster to dendritic fractal-like aggregates and therefore heat conduction of particles in the centre is reduced by those surrounding them. Bayesian inference is used to investigate how much knowledge about the morphology of these aggregates is required to reliably estimate primary particle size distributions. Laser-induced incandescence is further combined with a tomographic approach to obtain 3D distributions of primary particle sizes. Here, the focus is set to the influence of periphery parameters such as the initial flame temperature or the laser profile on 3D particle sizing jointly for the first time.

This work thus builds a bridge from the initial stages of soot formation by the detection of precursor molecules to the determination of soot particle sizes as an important quantity to follow the evolution process.

Kurzdarstellung

Bis heute ist der Prozess der Rußentstehung bei der Verbrennung von Kohlenwasserstoffen nicht vollständig verstanden. Dies ist im Wesentlichen auf das Zusammenspiel umfangreicher Reaktionskinetik, komplexer physikalischer Prozesse wie Wärme- und Massentransfer oder Agglomeration sowie eines erforderlichen Beobachtungsmaßstabs im Nanometer- bis hin zum atomaren Bereich zurückzuführen. Lasermesstechniken ermöglichen in vielen Fällen eine hohe zeitliche und räumliche Auflösung und sind daher ideal, um Einblicke in verschiedene Stadien des Rußentstehungsprozesses zu gewinnen.

In dieser Arbeit wird die Weiterentwicklung von zwei *in situ* Messtechniken beschrieben. Zum einen wird die Breitband-Absorptionsspektroskopie eingesetzt, um die frühen Stadien der Rußbildung zu untersuchen. Dabei werden polyzyklische aromatische Kohlenwasserstoffe als Vorläufermoleküle betrachtet, die für die Keimbildung und das Wachstum von festen Rußpartikeln verantwortlich sind. Ihr Absorptionsverhalten im ultravioletten Wellenlängenbereich erlaubt es, gemessene Spektren möglichen Speziesverteilungen zuzuordnen. Letzteres erfordert die Zusammenstellung einer Datenbank mit Absorptionsspektren der Einzel-Spezies sowie ein vereinfachtes energetisches Modell zur Berücksichtigung der hohen Flammentemperatur. Die Technik wird außerdem eingesetzt, um Veränderungen der optischen Eigenschaften zu beobachten, welche mit der Alterung der Rußpartikel zusammenhängen. Eine Veränderung der atomaren Anordnung der Rußpartikel, ähnlich der Graphitisierung, führt zu einer Verringerung der optischen Bandlücke, die auf der Grundlage von Breitbandabsorptionsmessungen ermittelt wird. Zusätzlich wird die Art des optisch-elektronischen Übergangs aus den Messungen abgeleitet, welche für vollentwickelte Rußpartikel auf einen indirekt erlaubten Übergang hinweisen.

Zudem kann mit Hilfe der zeitaufgelösten laserinduzierten Inkandeszenz die Größe der Rußprimärpartikel bestimmt werden. Eine Herausforderung besteht darin, dass diese Primärpartikel fraktale Aggregate bilden und daher die Wärmeleitung der Partikel im Zentrum durch die sie umgebenden Partikel reduziert wird. Mithilfe der Bayesschen Statistik wird untersucht, wie viel Wissen über die Morphologie dieser Aggregate erforderlich ist, um die Größenverteilung der Primärpartikel zuverlässig zu bestimmen. Die laserinduzierte Inkandeszenz wird zudem mit einem tomographischen Ansatz kombiniert, um 3D-Primärpartikelgrößen zu erhalten. Dabei liegt erstmals der Schwerpunkt auf der Bestimmung und dem Einfluss von lokalen

Umgebungsparametern wie der anfänglichen Flammentemperatur oder dem Laserprofil.
Diese Arbeit schlägt somit eine Brücke von den Anfangsstadien der Rußbildung durch den Nachweis von Vorläufermolekülen hin zur Bestimmung der Rußpartikelgröße als wichtige Größe zur Verfolgung des Entwicklungsprozesses.

Table of Contents

0 Symbols and Abbreviations

Latin symbols

Symbol	Unit	Description
A	-	Absorbance
a	m	Interlayer spacing
a_{xy}	-	Hydrocarbon specific constant
c	$m \cdot s^{-1}$	Speed of light
C_{abs}	m^2	Absorption cross section
C_{det}	-	Detection constant
C_{OV}	-	Overlap coefficient
c_{s}	$J \cdot kg^{-1} \cdot K^{-1}$	Specific heat
d_{a}	m	Aerodynamic diameter
D_{f}	-	Fractal dimension
d_{m}	m	Mobility diameter
d_{p}	m	Primary particle diameter
e	C	Elementary charge
$E(\widetilde{m})$	-	Absorption function
E_{γ}	eV	Energy of a photon
E_{g}	eV	Optical band gap
f_V	ppm	Soot volume fraction
h	J·s	Planck's constant
H	$J \cdot m^{-2}$	Laser fluence
I	$W \cdot m^{-2}$	Intensity after passing absorbing media
I_0	$W \cdot m^{-2}$	Initial intensity
$I_{\mathrm{b},\lambda}$	$W \cdot m^{-2} \cdot m^{-1}$	Spectral blackbody intensity
k_{B}	$J \cdot K^{-1}$	Boltzmann constant
k_{f}	-	Fractal prefactor
L	m	Absorption path length
L_{a}	m	Conjugation length
m	kg	Mass
m/z	$kg \cdot C^{-1}$	Mass-to-charge ratio
$\widetilde{m}$	-	Complex refractive index
n_i	m^{-3}	Number density

N_p	-	Number of primary particles
p	Pa	Pressure
q	$\mathrm{m^{-1}}$	Scattering wave vector
R_g	m	Radius of gyration
$R_\mathrm{g,eff}$	m	Effective radius of gyration
S_LII	$\mathrm{W{\cdot}m^{-2}{\cdot}m^{-1}}$	LII signal
S_abs	$\mathrm{m^{-2}{\cdot}Pa^{-1}}$	Absorption line strength
T_g	K	Gas temperature
T_p	K	Particle temperature
X_i	-	Mole fraction

Greek symbols

Symbol	Unit	Description
α	$\mathrm{m^{-1}}$	Absorption coefficient
α_T	-	Accommodation coefficient
β	-	Scaling constant
ε_λ	-	Wavelength dependent emissivity
λ	m	Wavelength
λ_AFR	-	Air-fuel ratio
ϕ	-	Equivalence ratio
φ_V	m	Line shape function
ρ	$\mathrm{kg{\cdot}m^{-3}}$	Density
σ_ext	$\mathrm{m^{-1}}$	Extinction coefficient
θ	°	Scattering angle
$\tilde{\nu}$	$\mathrm{m^{-1}}$	Wavenumber
ξ	-	Dispersion exponent

Abbreviations

AFM	Atomic force microscopy
ART	Algebraic reconstruction technique
BSU	Basic structural unit
CAHM	Carbon addition hydrogen migration
CARS	Coherent anti-Stokes Raman scattering
CHRCR	Clustering of hydrocarbons by radical-chain reactions

CPC	Condensation particle counter
CW	Continuous-wave
DCM	Dichloromethane
DIB	Diffuse interstellar absorption band
DMA	Differential mobility analyzer
EI	Electron-impact
ELPI	Electric low pressure impactor
ELS	Elastic light scattering
FSN	Filter smoke number
FWHM	Full width at half maximum
GC	Gas chromatography
HAB	Height above burner
HACA	Hydrogen abstraction C_2H_2 addition
HIM	Helium-ion microscopy
HITEMP	High-temperature spectroscopic absorption parameters
HITRAN	High-resolution transmission molecular absorption database
HOMO	Highest occupied molecular orbital
HRTEM	High resolution transmission electron microscopy
IC	Internal conversion
ICE	Internal combustion engine
IR	Infrared
ISC	Intersystem crossing
LDLS	Laser driven light source
LE	Laser extinction
LIBS	Laser-induced breakdown spectroscopy
LIF	Laser-induced fluorescence
LII	Laser-induced incandescence
LOS	Line-of-sight
LUMO	Lowest unoccupied molecular orbital
MAC	Mass absorption cross-section
MALS	Multi-angle light scattering
MART	Multiplicative algebraic reconstruction technique
MB	Molecular beam
MBMS	Molecular beam mass spectrometry
MD	Molecular dynamics

MIR	Mid-infrared
MPI	Multiphoton ionization
MS	Mass spectrometry
Nd:YAG	Neodymium-doped yttrium aluminum garnet
NIR	Near-infrared
NMR	Nuclear magnetic resonance
NO_x	Nitrogen oxides
OME	Polyoxymethylene dimethyl ether
OPO	Optical parametrical oscillator
PAHs	Polycyclic aromatic hydrocarbons (singular: PAH)
PMT	Photomultiplier tube
QCL	Quantum cascade laser
QoI	Quantities of interest
REMPI	Resonance-enhanced multiphoton ionization
SAXS	Small-angle X-ray scattering
SCLAS	Supercontinuum laser absorption spectroscopy
SEM	Scanning electron microscopy
SMPS	Scanning mobility particle sizer
SPI	Single-photon ionization
SSA	Soot self-absorption
STM	Scanning tunnelling microscopy
TDLAS	Tuneable diode laser absorption spectroscopy
TEM	Transmission electron microscopy
TEOM	Tapered element oscillating microbalance
TiRe	Time-resolved
TOF-MS	Time-of-flight mass spectrometer
TRFA	Time-resolved fluorescence anisotropy
UV	Ultraviolet
Vis	Visible
VUV	Vacuum ultraviolet
WALS	Wide-angle light scattering
WAXS	Wide-angle X-ray scattering
XAS	X-ray absorption
XPS	X-ray photoelectron spectroscopy
XRS	X-ray Raman spectroscopy

1 Introduction

The combustion of hydrocarbons has played an outstanding role in energy conversion for centuries and will be involved in the global energy sector for decades to come [1]. The conversion from chemical energy to heat and further conversion to motive power or electricity benefits from the high energy density of the fuels and the ease of their handling and logistics, e.g., availability and storage. The main areas relying on combustion technologies include power generation, transportation and various industrial sectors. Especially industries that depend on temperatures between 900 °C to 1600 °C are based on combustion processes capable of providing such high temperatures. In Germany, the largest sectors are the iron/steel, cement/lime and glass/ceramics industries [2]. At the same time, hydrocarbon combustion is always accompanied by carbon dioxide (CO_2) emissions, which is a major contributor to global warming. The emission reduction of this gas is undoubtedly one of the major challenges for mankind in the near future [3]. With the combustion of fossil fuels, CO_2 is reemitted to the atmosphere, which was chemically bonded and stored for thousands of years. This ultimately leads to a continuous increase in the global CO_2 net balance. Besides CO_2, the emission of other combustion species must also be considered. The operation conditions substantially affect the resulting combustion products and pollutants. Especially the ratio of fuel to oxidizer allows for the differentiation between a “fuel-rich” or “lean” combustion. With a shift to carbon-free fuels such as hydrogen (H_2) or ammonia (NH_3), the formation of nitrogen oxides (NO_x) is relevant, mainly due to high combustion temperatures [4]. For fuel-rich combustion of hydrocarbons the surplus carbon atoms (C) that cannot oxidize to CO_2 due to the lack of oxygen form solid carbonaceous particles known as soot.

The process of soot formation – as the main topic of this thesis – can be simplified as the transition from gaseous fuel radicals, over polycyclic aromatic hydrocarbons (PAHs) as intermediate molecules to carbonaceous solid soot nanoparticles and aggregates [5-7]. As will be shown, this transformation includes several stages. A detailed understanding is required to technically control the soot evolution in many different applications. Here, one main aspect is the reduction of soot (and soot precursor) emission as harmful pollutants. Its impact on the environment can take several forms, e.g., the reduction of albedo effects on the polar caps, its role as condensation nuclei during cloud formation, or an influence on radiation balance as a broadband absorber in the atmosphere [8-10]. Further, soot directly influences human health as a nanoparticle aerosol penetrating deeply into the respiratory system, causing

lung diseases such as cancer or chronic obstructive pulmonary disease [11], as well as cardiovascular diseases [12]. Here, besides the size and morphology [13, 14], it is particularly the reactivity of soot particles linked to their chemical structure that is assumed to be responsible for mutagenic damage [15]. Similar carcinogenic properties are known for PAHs [16, 17], which lead to increased attention on emission of, e.g., benzo[a]pyrene in the European Union over the last decade [18]. The World Health Organization assumes that 7 million death cases worldwide are related to air pollution every year [19]. At the same time, the reduction of soot and PAH emission bears the potential of rapid counteraction against these adverse health and environmental effects as the lifetime of these particles in the atmosphere is limited to a few days [9]. This was confirmed during the first weeks of the global COVID-19 pandemic in 2020, when due to decreased worldwide transport and economic activities, air pollution was noticeably reduced [20, 21].

Besides industrial processes, power generation or natural sources such as wild fires [9], a large contributor to soot emissions is the propulsion sector, e.g., by aircraft, light-duty vehicles or freight transportation [22]. This is especially true for heavy transport technologies such as shipping or truck traffic, as no sophisticated electrical technologies are available, mainly due to the low gravimetric and volumetric energy density of commonly used accumulator materials such as lithium-ion (Li-ion) batteries [23-25]. Therefore, most drive units of freight vehicles are based on the use of Diesel or heavy fuels as the cheaper fraction of the refinery procedure of crude oil [26]. The burning of these high carbon content fuels with high boiling points results in enhanced soot formation and its release into the atmosphere with the exhaust gas. To avoid these emissions, particulate filters are typically installed downstream of the internal combustion engines (ICE). To guarantee that the separated soot particles are completely oxidized to CO_2 and clogging of the particulate filter is avoided, a sufficiently high oxidation rate must be ensured even at lower temperatures present in the exhaust line [27, 28]. Here it was found that the nanostructure of the soot particles again strongly influences their oxidation behaviour [29]. A second possibility for emission reduction is the use of chemical additives that directly influence individual steps of the soot evolution process. For example, the addition of gases like hydrogen, CO_2 or water [30], as well as liquid additives such as polyoxymethylene dimethyl ether (more familiar as “OME”) to the fuel blend can directly reduce soot concentrations [31, 32]. Further, the addition of certain salts such as potassium chloride or alkali salts to the flame can impact soot and PAHs formation mechanisms [33, 34]. To assess the modes of action of these additives detailed knowledge about soot formation and oxidation mechanisms is

required [35]. A third option to minimize soot emissions is to provide defined operation conditions under which no enhanced soot formation occurs. Increasing the combustion temperature, for example, can drastically reduce soot concentrations. Yet, the correlation of temperature with other combustion species such as NO_x often leads to a conflicting trade-off between the resulting pollutants [36]. In reality, legal regulations are required to reduce emissions. To give an example, standards such as "Euro 6" for the automotive sector have been very limited to non-existent for ocean shipping. Within the last years, increased decarbonisation efforts have evolved in this sector and tighter regulations can be expected for the foreseeable future [37]. To this date, the emission of soot particles into the atmosphere remains a problem on a global scale.

At the same time, certain forms of soot are an industrially manufactured raw product called "carbon blacks" [38] with a large production volume, which is assumed to increase to a total capacity of 15 million tons a year by 2025 [39]. They are widely used as filler material to rubber and elastomer materials, specifically in the tyre industry. Here, the carbon black aggregates strongly influence physical parameters such as the abrasion resistance, elasticity or the reinforcement of the final product [40]. A second purpose of carbon blacks is their use as a black pigment [41]. Here, excellent insolubility in different media as well as strong thermal and colour stability can be named as some main advantages in comparison to competing black pigments based on iron oxide or other inorganic spinel materials [42]. In addition, carbon blacks are promising candidates in the design of energy conversion and storage technologies [43], e.g., improved Li-ion batteries, fuel cells or supercapacitors [44-46] and can further play a key role in the recycling economy of products such as tyres [47]. Again, the physical properties of the carbon blacks are a crucial parameter for their intended purpose [48]. The major share of carbon blacks' production goes back to the oil furnace black process. Here a fine mist of crude oil (or feedstock) is atomized into a natural gas combustor providing high temperatures of approx. 1650 °C. The oil droplets vaporize and form carbon black aggregates that are rapidly cooled or quenched from the further reaction by water spray insertion downstream of the reactor [38, 49]. This allows for specific control and design of a variety of different carbon black materials.

So far, the discussion about soot formation has been mainly related to combustion processes. Yet, the formation process is not strictly limited to combustion at all. Very similar processes that include the transition from aromatic hydrocarbons to solid carbon particles take place in a variety of different phenomena and applications. For example, the interstellar medium and especially the interstellar dust contains multiple forms of carbon, ranging from ionized C atoms over PAHs, carbon clusters and fullerenes to

carbonaceous solids [50-52]. It is assumed that PAHs could be responsible for a characteristic ultraviolet (UV) absorption band at 217.5 nm, as well as diffuse interstellar absorption bands (DIBs) from UV to near infrared (NIR) in galactic extinction observations [50, 53]. Also in our solar system, Saturn's largest moon Titan has an aerosol "rain" in its atmosphere similar to soot, which likely forms from PAHs [54]. Another technical challenge are solidified carbon depositions in components such as fuel injectors or combustion chamber valves mainly resulting from petrogenic PAHs that are initially contained in the fuel blend [55, 56]. These processes are strongly dependent on the fuel composition as well as pressure and temperature, and again a detailed understanding of the various soot formation routes is required for an improved design of these technical devices.
In almost all of the previously mentioned applications and effects, the physical and chemical properties of soot particles dictate their use and behaviour and therefore techniques to characterize quantities related to these properties are required. These include size and shape related, compositional or optical parameters of soot and are described in more detail in section 2.2.1. The challenges of determining these quantities include the nanometric to atomic size range, rapid conversions in milli- to microsecond timescales and harsh flame environments at elevated temperatures or pressures coupled to turbulent flow fields. These facts complicate the development of appropriate – and in the best case non-disturbing – diagnostics and therefore it remains an active research field to ultimately improve understanding of the soot formation process.

The aim of this work is the development and advancement of optical diagnostics to track and investigate the soot evolution process including (mainly) formation and (in parts) subsequent oxidation. The thesis is structured as follows: State of the Art, Aim of the Thesis, Overview of the Publications and their Interrelationships and finally Conclusions and Prospect. The publications themselves, which form the core of the thesis are reproduced thereafter. Specifically, UV-Vis absorption spectroscopy is used to identify PAH molecules as soot precursors [M1] and is used to investigate the type of optical band gap transition related to soot maturity [M2]. In addition, the laser-induced incandescence (LII) technique, which allows for determination of soot particle sizes and concentrations, is extended to the third dimension [M4] and critically assessed by means of statistical methods regarding the resulting quantities and influencing parameters [M3].

2 State of the Art

This section provides a brief overview of the current state of the art linked to the characterization of the soot evolution process. It is thus divided into two parts: first, the theoretical background and knowledge about the process itself are given. Second, the metrology and measurement techniques that allow us to gain a deeper understanding about the process by providing certain quantities of interest (QoI) are introduced. Obviously, both aspects are closely linked and the separation into two sections is mainly for reasons of structure and readability.

2.1 Fuel-Rich Hydrocarbon Combustion

While in the introduction several fields were mentioned where the transition of gaseous hydrocarbons to solid nanoparticles occurs, the upcoming sections focus on the soot evolution process during fuel-rich combustion. The thermodynamic definition of combustion involves the transition of chemically bonded energy of fuels to heat by an exothermal reaction with an oxidizer. By now, this complex process is not fully understood, and an advancement in this field requires the interplay between diagnostics and comprehensive models.

2.1.1 Kinetics and Modelling of Combustion Processes

The stoichiometric or lean combustion of hydrocarbons with air as the oxidizer medium can be described in terms of a global reaction equation with its general formulation given by

$$\begin{aligned} &\mathrm{C}_x\mathrm{H}_y + \lambda_{\mathrm{AFR}} \cdot a_{xy}\,(\mathrm{O}_2 + 3.76 \cdot \mathrm{N}_2) \\ &\rightarrow x \cdot \mathrm{CO}_2 + \frac{y}{2} \cdot \mathrm{H}_2\mathrm{O} + (\lambda_{\mathrm{AFR}} - 1) \cdot a_{xy} \cdot \mathrm{O}_2 + 3.76 \cdot \lambda_{\mathrm{AFR}} \cdot a_{xy} \cdot \mathrm{N}_2\,. \end{aligned} \tag{1}$$

Here, a_{xy} depends on the used hydrocarbon fuel and can be substituted by a_{xy}=x+y/4 and λ_{AFR} stands for the air-fuel ratio with values of 1 for stoichiometric, >1 for lean and <1 for fuel-rich conditions. It is directly related to the equivalence ratio $\phi = 1/\lambda_{\mathrm{AFR}}$ as the more commonly used quantity for sooting flames [57]. This global equation can be divided into multiple elemental reactions that form intermediate species that in turn might serve as source material for further reactions. In the case of fuel-rich combustion, the mass balance leads to an excess of carbon atoms that remain in form of, e.g., soot on the product side. The entire cascade of elemental reactions is hardly understood and consists of thousands of equations and possible reaction paths with hundreds of

participating species. Over the last decades, several groups have defined kinetic models that allow for the simulation of combustion processes (some including the formation of soot) based on listing most of the elemental reactions, thermodynamics and transport properties. One main effort of kinetic modelling lies in the reduction of mechanisms to the most dominant ones to reduce computational expense and complexity.

For a first assessment of such kinetic models, the high-temperature soot mechanism for ethene/ethylene (C_2H_4), combustion from the "CRECK modelling group" [58, 59] was adopted to an adiabatic one-dimensional freely-propagating premixed flat flame reactor provided and preset by the open source tool "Cantera" [60]. The equivalence ratio was set to 2.1, which corresponds to a slightly sooting flame. The profiles of some combustion species and intermediates as well as the adiabatic temperature are depicted in Figure 2.1.

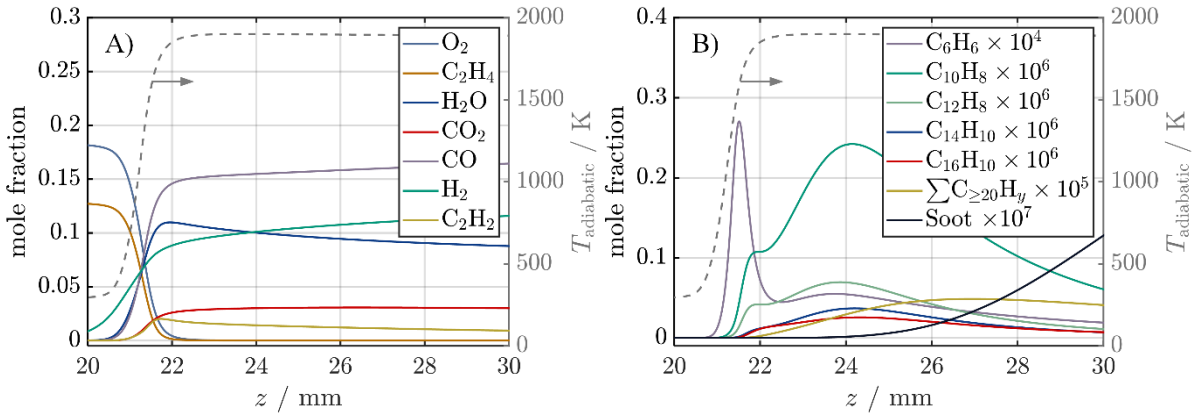

Figure 2.1: Mole fraction profiles of several combustion species and temperature in an adiabatic flame reactor (Cantera) for a one-dimensional ethylene/air flame at an equivalence ratio of ϕ=2.1 using the high-temperature soot mechanism from the CRECK modelling group. The average flame speed was 1.4 m·s^{-1}.

For reasons of readability and presentation, the calculated profiles are divided into two diagrams with the main combustion species and products depicted in the left plot A, while some major aromatic species and soot are exemplarily shown on the right side B. The absolute value of the abscissa is arbitrary as the zero point was randomly chosen. The location of the flame front can best be identified by the steep temperature rise from 293 K to ~1900 K depicted as dashed grey lines in both diagrams. As can be seen in the left plot, the reactants oxygen (O_2) and ethylene (C_2H_4) (see Equation (1)) are rapidly consumed while at the same time combustion products such as water (H_2O) and carbon dioxide (CO_2) are formed. Additionally, species such as carbon monoxide (CO) or hydrogen (H_2) are present due to the high-temperature environment and a comparably large share of acetylene (C_2H_2) exists, which will later be identified as a decisive species responsible for aromatic growth. While the species shown in the left plot A are covered

by most of the standard reaction mechanisms (e.g. “GRI-30” [61] with 53 species and 325 reactions) the profiles in the right diagram B require the formation mechanisms of PAHs [62] and soot [58, 59] (the latter with 452 species and 24041 reactions). Some exemplary aromatic species are displayed, including benzene (C_6H_6) as the smallest, up to $C_{16}H_{10}$ (pyrene and fluoranthene) and a summarized group of larger PAHs with more than 19 C atoms. Considering the species-specific scaling in the legend, it becomes obvious that generally smaller aromatics are present in larger amounts. At the same time, the peak positions of larger species are shifted to increased z values, which corresponds to longer residence times in the flame environment and consequently a progressed formation schedule. The formation of soot particles and aggregates starts relatively late with an exponential-like increase between 24 mm and 30 mm, already indicating that PAHs might serve as precursor molecules.
For the understanding and design of combustion devices, these models are already valuable tools and might become even more useful with further development. Yet, to validate these models, measurement techniques are required that provide species selective information. Further, the simulations of more complex scenarios (beyond a one-dimensional flame) become excessively more complex [63] and certain boundary- and input parameters such as temperature maps must be defined prior to the simulations.

2.1.2 Flame Types and their Impact on Soot Formation

To allow for a comparison between model predictions and experimental data, standard type flames are required [64]. Therefore, multiple burner designs with standard configuration settings have evolved within the last decades and have been intensively studied and characterized by various research groups and different measurement techniques. In principle, a classification can be made into premixed flames, where fuel and oxidizer are mixed prior to ignition, and non-premixed flames, where both components are added separately and diffusion processes become dominant [65]. There are also mixed forms commonly named partially premixed flames, for which some share of the oxidizer is added to the fuel before ignition. In addition, combustion is always linked to fluid dynamics and therefore a division between laminar and turbulent flames is drawn. The chaotic randomness and transient nature of turbulence complicates investigations and typically requires a high temporal resolution in the millisecond range or below [66]. While many technical flames in, e.g., aircraft gas turbines or rotary kilns are of a non-premixed and turbulent nature, the focus of this work lies on two types of laminar flames, as their steady and reproducible behaviour is ideal for the development

of optical metrology. In addition, they provide an ideal test bed for comparison against simulation results leading to an increased process understanding.

First, to reduce the degrees of freedom a one-dimensional reactor serves as an ideal system as the soot formation process is simply a function of residence time, or – as related to the flow velocity and direction – a function of the height above the burner (HAB) outlet. Its technical realization corresponds to a laminar premixed flat flame usually stabilized by a stagnation plate and shielded from the surrounding air by an inert gas, e.g., a nitrogen (N_2) shroud [67, 68]. The adjustment of the fuel and oxidizer flows allows for a straightforward setting and variation of the equivalence ratio. Figure 2.2 A and B show two C_2H_4/air flat flames at $\phi = 1.3$ on top and $\phi = 2.1$ below. Although both flames are run under fuel-rich conditions ($\phi > 1$) the yellowish flame luminosity deriving from the radiation of soot particles can only be observed for the $\phi = 2.1$ flame. This can be traced back to the existence of a soot threshold, describing the transition point when the first solid soot particles are formed. It is strongly dependent on the fuel used, as well as on temperature and pressure [69]. As a rule of thumb, the higher the C share (compared to H) of the C_xH_y fuel the lower the equivalence ratio of the soot threshold. As an example, the soot formation threshold of a methane (CH_4) flame is at larger ϕ values compared to a C_2H_2 flame. Yet, as highlighted by Michelsen et al. [70] the definition of the soot formation threshold varies throughout the literature and is sometimes defined by the detection of first LII signals or by the onset of light absorption in the visible (Vis).

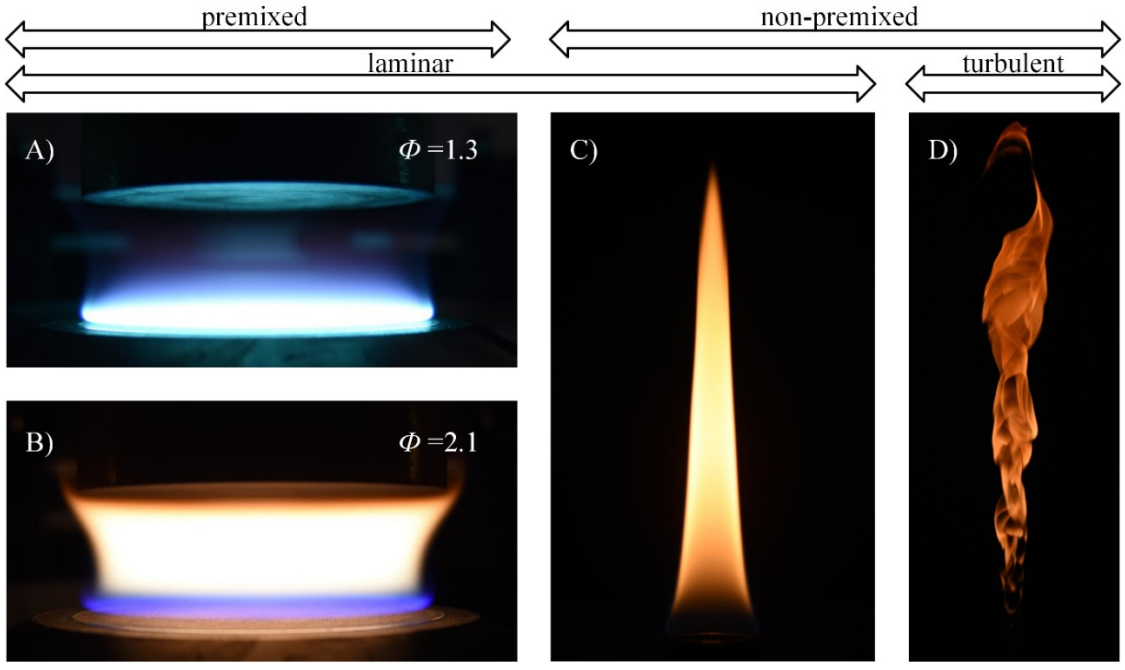

Figure 2.2: Overview of different types of laboratory flames ranging from premixed flat flames (A & B), over a laminar non-premixed flame (C) to a partially turbulent flame (D).

A further observation from the premixed flame photographs is the blue chemiluminescence signal right after the burner outlet. These photon emissions arise from chemical reactions of certain species and can mainly be attributed to CH and C_2 radicals [71, 72], the latter of which are also called “Swan” bands [73, 74]. To achieve a deeper understanding of this aspect, Figure 2.3 shows the spectrally resolved emission signals of both premixed flames meaning that the emission intensity is plotted against the wavelength λ. Here, three spectrometers covering different spectral ranges are combined and a wavelength dependent intensity calibration was performed in a wavelength range from 350 nm to 1000 nm. Therefore, the absolute intensities must be treated with caution as the different instrument responses are not corrected over the entire spectral range and especially the decrease of intensities at λ>1000 nm does not present a physical behaviour. Yet, the CH and C_2 emissions can clearly be observed as peaks in the visible wavelength range between 400 nm to 750 nm for the flame at $\phi = 1.3$. There are further chemiluminescence peaks located in the UV (λ<400 nm), e.g., from the hydroxyl radical (OH) at ~306 nm and ~290 nm. In addition, emission bands of water can be observed in the NIR region >900 nm. For the flame at $\phi = 2.1$ a broadband emission signal with an exponential-like increase for λ>400 nm results from the incandescence signal of the soot particles at flame temperatures of approximately 1750 K. Here, the optical properties of soot cause the deviation from an ideal black body, as will be discussed in more detail in an upcoming section. The high-frequency oscillations superimposing the infrared (IR) signals are not related to the emission but very likely derive from etalon effects in an optical component [75].

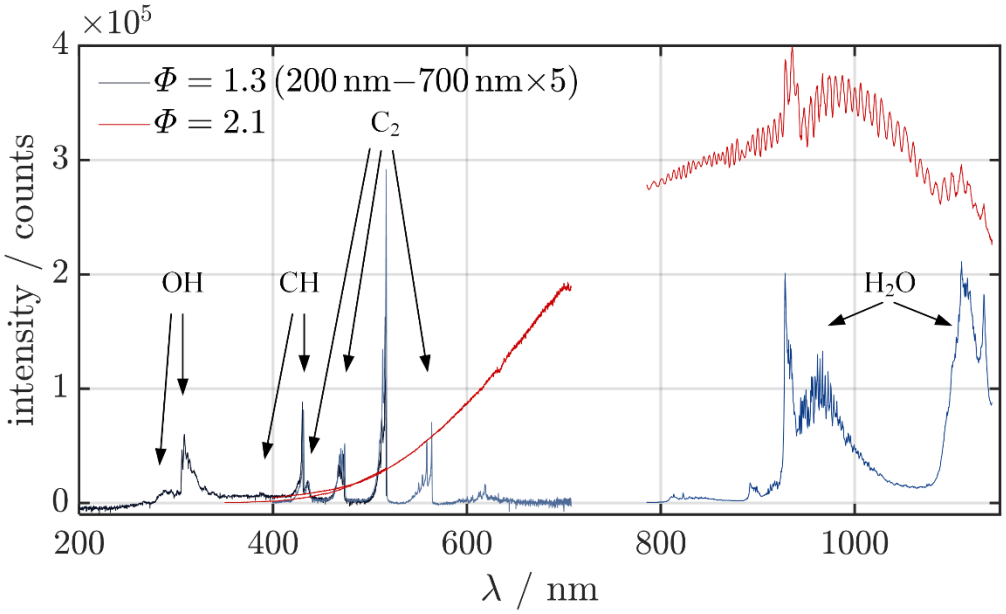

Figure 2.3: Spectral features of both fuel-rich premixed flames are shown in Figure 2.2 (A & B). The blue lines refer to the flame at $\phi = 1.3$, while red lines indicate a $\phi = 2.1$.

A second type of flame investigated in this work is a non-premixed laminar coflow ethylene/air flame depicted in Figure 2.2 C. In contrast to a premixed flame, the oxidizer and fuel are first spatially separated forming a defined reaction front named flame front. On both sides of the flame front, the gas composition and stoichiometry differ, leading to the growth of larger aromatics as the decomposition products on the fuel side favour certain PAH and soot formation pathways. Besides the coflow design, the fuel and oxidizer streams can also be directed from opposite sides leading to counterflow flames [76, 77]. Overall, the non-premixed type flame is closer to most applications and is commonly used as a standard type flame for investigating the soot evolution process regarding measurements and models [78-81]. An example of a partially turbulent diffusion flame is depicted in Figure 2.2 D and can serve as a next logical step of a laboratory burner concept towards more technical and applicative flames [82]. For a detailed description of the burner designs and configurations, the reader is referred to the respective manuscript [M1-M4] and the references therein.
Besides the utilized fuel and flame types, the formation of soot is further dependent on surrounding conditions such as pressure and temperature [69, 83]. It has been shown that soot forms preferably in a range from 1500 K to 1900 K and the formation rate increases under elevated pressure, which is particularly relevant as many applications such as internal combustion engines run at these conditions [84]. As a consequence, specialized high-pressure burners have been developed for closer investigations [85-88]. In contrast, low-pressure burners are widely used to spatially stretch the main reaction region and facilitate investigations of individual regimes of the soot evolution process [89, 90]. Yet, it must be kept in mind that with changed surrounding conditions different pathways of the soot formation process may become relevant. To give an extreme example, it was found that under detonation experiments soot particles with diamond-like structures are formed due to extreme temperature and pressure conditions [91].

2.1.3 The Soot Evolution Process

The previous section highlighted that the evolution of soot is dependent on various parameters such as utilized fuel, pressure, temperature or stoichiometry, which is often linked to the flow conditions. Yet, in any case it ultimately includes a transition from hydrocarbon fuels to solid carbonaceous soot particles. The different forms of hydrocarbons or amorphous carbons are depicted in the ternary diagram of Figure 2.4 with the corners pure hydrogen, sp^2 hybridized graphite and the sp^3 hybridization of the diamond structure of carbon. With the simplification of neglecting the oxygen share, a

common soot evolution route (e.g., for atmospheric combustion of gaseous hydrocarbons such as C_2H_4) is schematically depicted by the red arrow (adopted from Ref. [92]). It reveals that besides the deposition from fuel molecules to solid particles a change in the internal atomic structure of soot particles occurs, which is often referred to as the maturing of soot. This goes hand in hand with a morphological transition from gaseous precursor molecules, to first spherical nanoparticles and finally fractal-like aggregate structures composed of multiple primary particles.

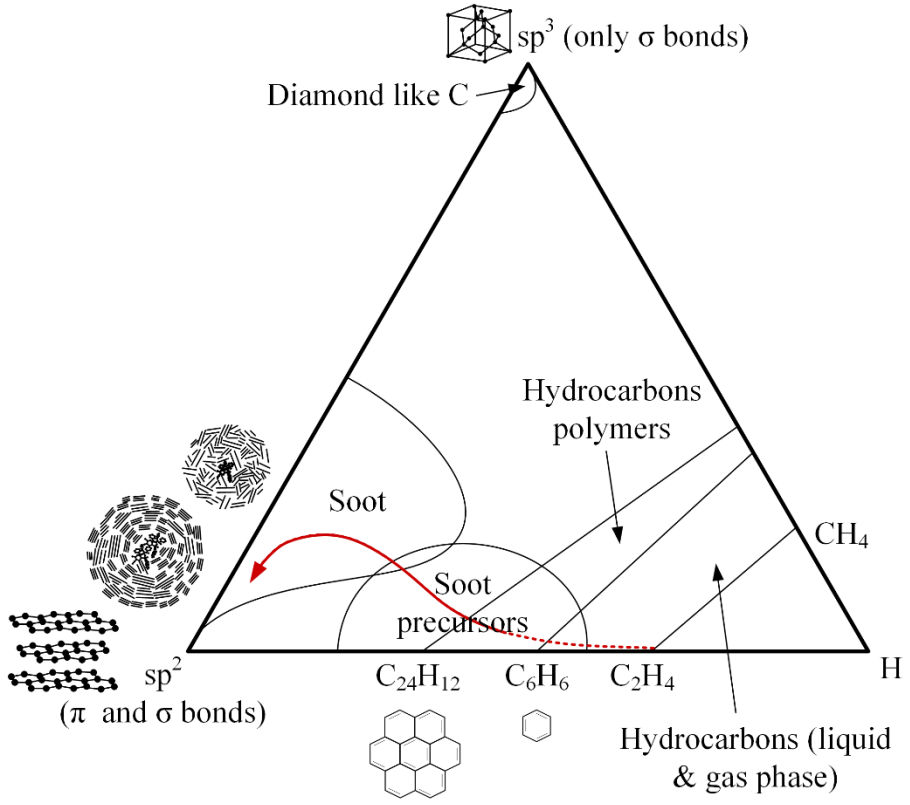

Figure 2.4: Ternary diagram of amorphous carbon taken from [92] with the corners H (lower right), sp²-carbon (lower left) and sp³-carbon (top). Different forms of hydrocarbons are located at different regions, and the red arrow indicates a common route of soot formation.

The entire process can be divided into several transition regimes, which are often described as the *gas-phase and PAH chemistry*-, the *particle inception*-, the *surface growth and coalescence*-, the *particle graphitization, agglomeration and aggregation*- and finally the *particle oxidation*-regions. In reality, there is always overlap and no sharp separation between the individual stages exists, and as a result, this work refrains from a structuring classification into these regions. However, to provide a lucid overview Figure 2.5 shows a simplified description of the proceeding soot formation process and the participating species and will help to follow the discussion in this section.

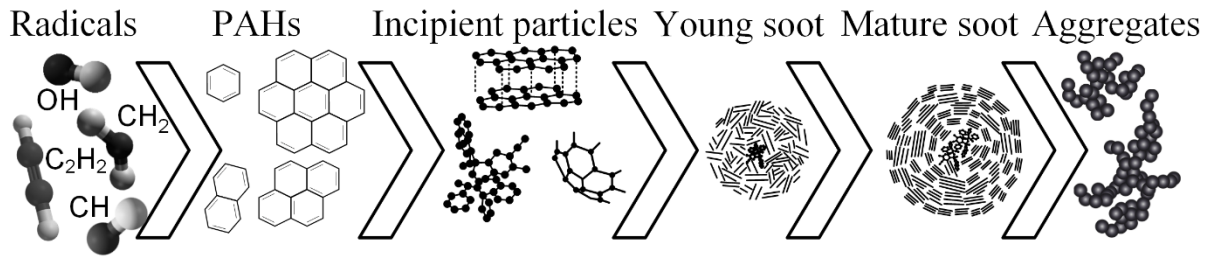

Figure 2.5: Schematic illustration of the different species and formation steps during the soot formation process.

As the naming of the participating species showed a large variation especially regarding the different research fields (e.g., atmospheric research, pyrolysis research, combustion research) one essential requirement is the use of precise and uniform terminology that was recently clarified by Michelsen et al. [70] and builds the basis for this work.

The first step of the soot evolution process is the decomposition of the hydrocarbon fuel by small radicals such as CH, OH, O, H or CH_2 [64, 93]. The subsequent formation of the first aromatic benzene (C_6H_6) ring is strongly dependent on the utilized fuel as well as the temperature-dependent rate coefficients as shown by Kohse-Höinghaus et al. [94]. Yet, four important reactions could be identified with the recombination of two propargyl radicals (C_3H_3) as one possible option [95]. Besides, the reaction of C_4H_5 with acetylene (C_2H_2) results in the formation of benzene + H. As a third option, the reaction of C_4H_3 [96] with acetylene (C_2H_2) leads to a phenyl ring (C_6H_5), which can hydrogenate to C_6H_6 under the presence of H_2 and H. A fourth reaction includes cyclopentadienyl (C_5H_6) and a methyl radical (CH_3) to form benzene + 2H. The formation of the first benzene ring is considered the rate-defining process step in the soot formation process followed by its growth to multiple ring PAHs [64].

The two-ring PAH naphthalene ($C_{10}H_8$) can be formed by the self-reaction of cyclopentadienyl (C_5H_6). However, it is widely accepted that the main reaction pathway for planar growth to PAHs is the “hydrogen abstraction C_2H_2 addition” (HACA) mechanism first described by Frenklach [97]. It is based on the activation of a benzene ring by the abstraction of a hydrogen atom and the addition of a C_2H_2 molecule. By repeating this mechanism a second ring forms. This pathway is schematically depicted in Figure 2.6.

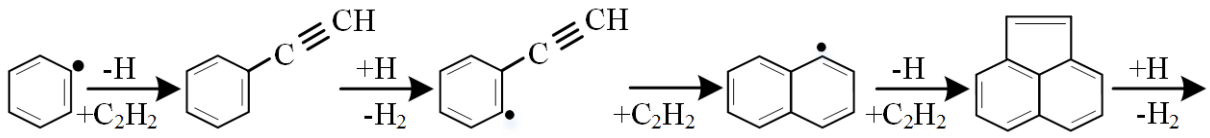

Figure 2.6: Hydrogen abstraction C_2H_2 addition (HACA) mechanism responsible for the growth of aromatic rings derived from [69]. The aryl radical (incorporating a free carbon atom) is depicted with a black dot.

Recalling the mole fraction profiles of Figure 2.1, C_2H_2 as well as H_2 are present in adequate amounts during the entire formation region. The ring arrangement of PAHs with more than two rings can obviously take different forms and a distinction is made between cata-condensed (where just two rings share a single carbon atom resulting in more linear arrangements) and peri-condensed (also three rings have the same carbon atom in common leading to more circular structures) PAHs. Their formation is closely linked to their stability, which mainly depends on temperature. On the one hand, temperature drives the kinetic mechanisms but at the same time causes fragmentation of the molecules [98]. It was found that at high temperatures in flames stable peri-condensed PAHs such as pyrene or coronene are more likely to be present [5, 98, 99]. In addition to PAHs, aliphatic species are known to exist in sooting flames [100] and aliphatic branches at six-membered benzenoid rings were identified by atomic force microscopy [101]. This suggests that besides the sole growth through the HACA mechanism other reaction routes occur, and resonance stabilized free-radical species were identified as major contributors through clustering of hydrocarbons by radical-chain reaction (CHRCR) mechanisms [98, 102].

The next step of the soot evolution process is the particle inception or gas-to-solid phase deposition. It is the least understood step of soot evolution and can be grouped into chemical and physical mechanisms [98, 103]. There are also mixed forms of both phenomena and overall three major routes were identified. The CHRCR mechanism as a first chemical pathway is responsible for the growth of initiator radicals, which in combination with hydrocarbons form disordered three-dimensional covalently bonded incipient particles [102]. The shift from planar 2D to 3D objects can result from chemical crosslinking between PAH monomers and a rotation between both of the monomer fragments [104]. A second physical pathway is the formation of dimers and trimers through the stacking of planar PAHs by Van der Waals forces. Here, a remaining inconsistency was the finding that only Van der Waals forces between PAHs as large as or larger than circumcoronene ($C_{54}H_{18}$) are thermodynamically stable at flame temperatures, contradicting the observation that mainly moderately sized PAHs such as pyrene and coronene exist in sufficient amounts to explain soot inception [105]. Yet,

recent studies experimentally confirmed the existence of dimers of moderately sized PAHs stabilized through covalent bonds [106, 107]. A third chemical route is given by a fullerene-like growth through the curving of planar PAHs, but this process was found to be too slow to explain the soot inception in flames [98]. Yet, the formation of curved PAHs through the addition of a pentagonal ring in the 6-membered ring lattice is still considered as a relevant process [108], especially regarding curvature in the basic structural unit (BSU) of soot particles as observed by high resolution transmission electron microscopy (HRTEM) [109]. Further, pentagonal rings can be responsible for the crosslinking between peri-condensed PAHs [110] as well as dimer stabilisation and therefore support the formation of disordered incipient particles.

After the formation of these 1 nm-6 nm sized incipient particles they grow further through coalescence (describing the complete merging of two particles similar to droplets) as well as surface growth [111]. The surface growth of the particles follows very similar processes as discussed during the planar PAHs growth section. Besides HACA and CHRCR the carbon addition and hydrogen migration (CAHM) was identified as a possible candidate at lower flame temperatures of ~1500 K [112]. Yet, during the discussion session at the 37th International Symposium on Combustion in 2018 in Dublin (Ireland), Frenklach generalized the definition of HACA to “hydrogen activation carbon addition” as a more universal description as the aryl radical sites might also serve as bonding partners to other aliphatic or aromatic species. Therefore, HACA covers a larger range of possible reactions and remains the driving mechanism during particle inception and surface growth [113, 114]. The particle growth process leads to the formation of spherical primary particles of ~10 nm-50 nm in diameter and is accompanied by a maturing process in form of a fine structural change. First, the particles are highly amorphous with a large H/C ratio and a high sp^3-share and are typically referred to as young soot particles. Over time, the structure of these particles partially matures and transforms into so-called turbostratic graphite forming onion-like graphitic layers at the surface of the particle (growing towards the core). This process is mainly temperature-driven and accompanied by carbonization and an H/C-ratio decrease.

Simultaneously, the spherical primary particles collide with each other and first form loosely bond agglomerates mainly by Van der Waals and electrostatic forces [115]. This process is followed by the formation of tightly bonded aggregates mainly due to ongoing surface growth [116]. This finally leads to the formation of random, dendritic fractal-like aggregates comprised of primary particles that often follow a log-normal size distribution [117]. The sizes of the aggregates formed are also polydispersely

distributed and can be approximated by a log-normal distribution as well. More details are provided in manuscript [M3] and the references therein.
Oxidation as the last step of the soot evolution process describes the reaction of the soot particle surface with oxygen or oxygen-containing gases to CO and CO_2. It leads to a decrease in the particle size and can further result in the breakup or fragmentation of soot aggregates. Stanmore et al. discerned between oxidation at temperatures >800 °C occurring in flames and oxidation at lower temperatures mainly relevant in the exhaust gases [118]. For the former, especially the existence of the hydroxyl radical with increased reactivity in comparison to molecular oxygen dominates the process and with the addition of gases such as CO_2 or H_2O the OH-balance can directly be influenced [30]. Oxidation at lower temperatures is extensively studied to assess the possibilities of emission reduction [27, 119]. Yet, for the present work the oxidation processes occurring in flame environments are more relevant [120] and in the case of a non-premixed flame is located towards the tip of the flame [121].

2.2 Measurement Techniques to Characterise the Soot Evolution Process

Large parts of the knowledge about the individual steps of the soot evolution process derive from the development and utilization of various measurement techniques which are capable of providing certain quantities for its characterization. For a comprehensive understanding, the combination of multiple measurement techniques is required, as each technique is typically only applicable to a certain stage of the process and is also limited in terms of its achievable spatial and temporal resolution [64, 79, 92, 93, 122, 123]. In this section, first, an overview of some of the most important quantities related to the soot evolution process is given, followed by listing some of the most commonly used diagnostics. The latter is divided into sampling-based *ex situ* techniques and *in situ* capable approaches, which in many cases are optical techniques allowing for non-disturbing investigations. An additional reasonable classification could be drawn between diagnostics for gas phase molecule detection and techniques to quantify the properties of solid soot particles and aggregates. However, in the present work, it is explicitly mentioned for each measurement technique which quantities can be resolved.

2.2.1 Quantities to Describe the Soot Evolution Process

Prior to the discussion about the various diagnostics for investigating the soot evolution process, several of the most important quantities are introduced. Obviously, one main interest lies in the assignment of the type and amount of species present in the

measurement volume. Therefore, the mole fraction X_i or the number density n_i of species i mainly in the form of precursor molecules or the soot particles are of paramount interest. The latter is often described by the soot volume fraction $f_V = n_{\mathrm{Soot}} \cdot \pi \cdot d_{\mathrm{p}}^3 / 6$, which can be expressed as the product of the number concentration n_{Soot} and each particle's volume if monodispersly distributed and spherical particles are assumed [124]. As shown in Figure 2.7 several quantities describe size-related or morphological parameters and can therefore be obtained from imaging techniques such as microscopy. These include the primary particle diameter d_{p} typically ranging from 10 nm-50 nm for soot. The radius of gyration R_{g} is the radius from the aggregate's centre of mass that results in the same moment of inertia as the actual mass distribution of the aggregate and is therefore a measure for its effective size. Obviously, it strongly depends on the morphology of the aggregate, which is defined by the fractal dimension D_{f}. As can be taken from the inset of Figure 2.7 A, the dimensionality D_{f} of the aggregate structures varies somewhere between 1 as a linear neckless-like shape and 3 as a clustered raspberry-like structure. For soot, typical values lie within a range of 1.5 to 2.0.

There are further aggregate-related size descriptors such as the mobility diameter d_{m} [125], which is an equivalent diameter for a balance between drag- and electric forces of charged particles in an electric field. It is measured by techniques described in detail in section 2.2.2.3. Empirical relationships between d_{m} and quantities as d_{p} or R_{g} allow to retrieve the actual size parameters [126, 127]. As the aggregate is comprised of multiple primary particles, the number of primary particles per aggregate N_{p} is relevant and can be described by the fractal relationship [128] with

$$N_{\mathrm{p}} = k_{\mathrm{f}} \cdot \left(\frac{2\, R_{\mathrm{g}}}{d_{\mathrm{p}}} \right)^{D_{\mathrm{f}}} . \qquad (2)$$

Here, k_{f} is the fractal prefactor with values ranging from <1 up to ~4 for soot [115, 129]. Figure 2.7 reveals that in reality the primary particles are not in perfect point contact but overlap to a certain degree, which can be described by the overlap coefficient $C_{\mathrm{OV}} = (d_{\mathrm{p}} - d_{ij})/d_{\mathrm{p}}$ with typical values between 0-33 % [128-130]. This mainly derives from ongoing surface growth after agglomeration as described in section 2.1.3. Further important measures are related to the fine structure of soot, which can be seen as lamella-like structures in the HRTEM image of Figure 2.7 B, taken from [119]. For example, the largest length in a PAH monomer (schematic illustration in the inset) is termed the conjugation length L_{a} and typically takes values of ~1 nm for soot BSUs.

The separation between the monomer layers is given by the interlayer spacing a, which is 0.335 nm for graphite and decreases from values >0.5 nm for young soot down to ~0.35 nm for mature soot [109].

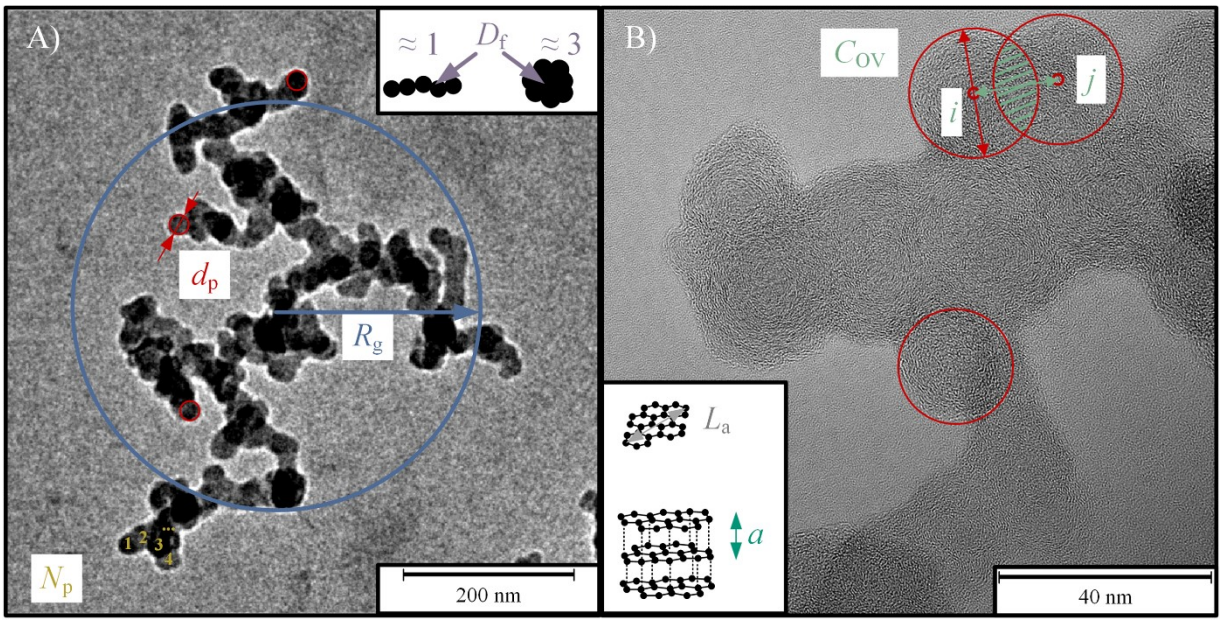

Figure 2.7: Schematic depiction of certain quantities related to the soot formation process. A: Transmission electron microscopy (TEM) image of a dendritic soot aggregate sampled from a premixed C_2H_2/air flame with an equivalence ratio of ϕ=2.7 at HAB=17 mm. B: A HRTEM image of iso-octane soot taken from [119].

Beyond these concentration- and size-related descriptors, further properties related to the fine structure of soot are known to change throughout the soot evolution process. These include the density of soot ρ, the amount of sp^2/sp^3 hybridization, the defect density, the C/H ratio or the reactivity. Excellent overviews are provided by various references [92, 93, 131] and summarize the evolution of these quantities throughout the soot formation process. In many cases, these quantities are highly correlated, such as the density ρ and the specific heat c_s and additionally often show strong temperature dependencies [132]. This complicates evaluation routines of optical diagnostics that often rely on precise knowledge of these parameters. Obviously, also the optical characteristics of the targeted materials are of great importance. The most important ones are the absorption function $E(\tilde{m})$ with the complex refractive index $\tilde{m}$, the absorption coefficient α, the dispersion exponent ξ or the optical band gap E_g, which will be explained in more detail in upcoming sections. Additionally, the entire soot formation process is strongly dependent on the flame temperature T_g, which makes its determination an important aspect from which to draw reasonable conclusions. Various optical thermometry techniques were developed, including pyrometry, laser-induced

fluorescence, two-line atomic fluorescence, coherent anti-Stokes Raman- or absorption spectroscopy, which are briefly described in the respective upcoming sections.
This list of quantities is not complete and for certain diagnostics, certain parameters become relevant, e.g., the mass-to-charge *m/z* ratio for mass spectrometry or the thermal accommodation coefficient α_T for LII.

2.2.2 Sampling Based *ex situ* Techniques

Sampling based measurement techniques are often considered the "gold standard" to determine various QoI, as the measurement location is taken out of harsh flame environments and the devices can specifically be designed to acquire high quality data regarding sensitivity or resolution. Yet, they mainly suffer from disturbing the underlying process by the sampling device as well as a possible transformation of the probe materials throughout the sampling line, e.g., by ongoing chemical reactions. In this section, the main focus lies on imaging microscopy, mass spectrometry, separation-based techniques and Raman spectroscopy, as these techniques are widely used for soot studies. Other *ex situ* techniques such as nuclear magnetic resonance (NMR), are capable of providing insight into the molecular structure of PAHs and soot but are not discussed in more detail in this work [133, 134].

2.2.2.1 Imaging Microscopy

With regard to the previous sections, it is quite understandable that imaging techniques are desirable as multiple quantities can directly be extracted from the images. Microscopy approaches with resolutions of few nanometres and even down to the atomic level are therefore widely applied at different stages of the soot evolution process [92]. In any case, a sampling of the probes from the process is demanded as direct measurements, e.g., inside the flame, are not feasible. Typically for extraction of soot particles from a flame thermophoretic sampling is used. Here, a grid or a disc is rapidly inserted into the flame with a dwell time of tens to hundreds of milliseconds during which the soot particles are deposited on the substrate [135].
For decades, transmission electron microscopy (TEM) has been used to analyse the size d_p and morphology ($R_\mathrm{g}, D_\mathrm{f}$) of soot particles and aggregates, including their size distribution parameters as well as the overlap coefficient C_OV [136]. It is based on the transmission of an electron beam through a thin probe (<100 nm) and the (electron-) wave-particle interaction. The very short wavelengths of the electron beam compared to visible light improves the achievable resolution according to the Abbe limit. The microscope consists of an electron emission source (~200 keV), a collimating

(electromagnetic) lens, the probe, a focusing lens and a detector. An exemplary TEM image of a soot aggregate taken from a premixed flame is shown in Figure 2.7 A. In combination with soot the technique is limited to particles with a diameter larger than ~10 nm as for smaller particles the low contrast between probe and substrate (usually carbon) reaches the noise level. An increased electron beam intensity cannot solve this problem as it leads to significant changes or damage of the particles [137].

A microscopy technique that allows to image smaller incipient soot particles is atomic force microscopy (AFM) [138, 139]. Here, the surface of a probe is scanned typically with a one-atomic tip on a cantilever. The movements of the tip caused by, e.g., surface roughness or the deposited particle on the substrate are optically measured by the reflection of a laser beam. By scanning the entire probe with precise piezoelectric positioners, a topographic measurement of the probe is achieved. In most cases the tip is operated in tapping mode, meaning that it oscillates at a high frequency to avoid probe or tip damage and further increase the quality of the measurement [140]. More recently, AFM was used to image PAHs from flames, revealing features such as aliphatic branches or chains as well as five-membered rings for the first time [101, 141].

The detection of PAHs and PAH-clusters or stacks is also possible using scanning tunnelling microscopy (STM) [142, 143]. Here, a voltage is applied to a metallic tip, which is placed close to the sample surface. A scan of the sample leads to positions where electrons are emitted from the sample's atoms due to the quantum tunnelling effect resulting in an electric current, which is measured and used to create an image. Additionally, electronic properties can be inferred from the measurements such as the band gap [144].

The use of helium-ion microscopy (HIM) as a sensitivity and contrast enhanced version of scanning electron microscopy (SEM) enables a simultaneous detection from small 4 nm-8 nm sized incipient particles up to soot aggregates [137, 145, 146]. In contrast to TEM, the principle of SEM is based on focusing an electron beam on the sample and the detection of the secondary electrons emitted from the sample surface. For HIM the electron source is replaced by an ion source with enhanced brightness and an increased amount of secondary electrons for each incoming ion. In addition, the backscattering of ions can be used for imaging, resulting in a better sub-nanometre resolution.

HRTEM allows to resolve the internal fine structure of soot particles by focusing the electron beam on the sample and detecting the constructive and destructive interference of transmitted and diffracted electrons to generate a phase-contrast image [109]. An example image (taken from [119]) is depicted in Figure 2.7 B. This enables the investigation of the maturity stage of the soot particles as turbostratic arrangements of

matured and partially matured soot is clearly different from the amorphous character of young soot [147]. In addition, quantities such as the stacking order, the conjugation length L_a, the interlayer spacing a or the fringe tortuosity can be extracted [27]. The latter describes the deviation from linear fringes and might be closely related to the existence of curved PAHs in the BSUs. One drawback of HRTEM is the possibility of damaging the probe or changing its structure through annealing as typically higher electron beam energies are required compared to TEM [148].
An excellent overview of the different microscopy techniques together with values for their achievable resolutions and exemplary images is given by Baldelli et al. [92].

2.2.2.2 Mass Spectrometry for PAH Detection

While microscopy-based techniques allow for the investigation of single particles or molecules individually, they do not directly provide information about the concentration or distribution of certain species or at least require elaborate frequentist repetitions to receive statistical meaningful results. Especially for the variety of different PAH classes present during the soot formation process quantitative and selective measurements are challenging. Over the years, mass spectrometry (MS) based approaches have developed into powerful tools to characterize the type and amount of molecular species such as PAHs. In principle, these techniques are based on sampling from the process, a classification step based on, e.g., ionization and a detection device. For each step various designs exist. Starting with the sampling method one common option is sampling by molecular beam (MB) formation [149]. Here, a small (100 µm-500 µm) quartz nozzle is placed inside the flame and in a two-staged low-pressure expansion the flame gases are extracted, stopped from the further reaction by quenching and finally form a collisionless free-molecular flow. One advantage over continuous regime microprobe extraction is the ability to investigate reactive species such as radicals [122]. The use of gas chromatography (GC) allows to directly detect lighter aromatics (up to benzene) [150] but requires additional extraction of heavier aromatics in a solvent such as dichloromethane (DCM) [151].
The ionization of the molecules can either be achieved by electron-impact (EI) or photoionization. The latter can be subdivided into single-photon (SPI) and multiphoton ionization (MPI). While EI is commonly used for flame diagnostics, fragmentation of the molecules is more likely compared to photoionization and overall lower selectivity and sensitivity are given [122]. As the energies required for PAH ionization lie typically somewhere around 6 eV-9 eV, SPI requires vacuum-ultraviolet light (VUV) and therefore either a VUV laser (e.g., ninth harmonic Nd:YAG laser at 118 nm) or

synchrotron radiation [152]. The latter benefits from a high brilliance and easy tuneability and therefore a targeted choice of photon energies, yet the availability of such devices is limited. Resonance-enhanced multiphoton ionization (REMPI) requires the simultaneous absorption of two or more photons with energies below the ionization threshold to ionize the targeted molecule [153]. As the energy gaps are specific for different molecules this technique has a high selectivity, especially by coupling it with a wavelength-tuneable dye laser. In addition, fragmentation becomes negligible due to the low photon energies [64]. Yet, for targeted and quantitative results knowledge about the ionization cross sections of the individual species is required [154].
For detection of the ions typically a time-of-flight mass spectrometer (TOF-MS) is used. It relies on the dependency of the kinetic energy of the ions from their mass-to-charge (*m/z*) ratio. This leads to a higher velocity of low mass ions and an earlier detection compared to heavier species. A second option is a quadrupole mass spectrometer, which consists of four rods with an oscillating voltage surrounding the sample flow and solely ions of a certain *m/z* ratio pass through the electric field and reach the detector.
In contrast to MBMS a GC consists of a long flow-through column in which the sample is injected, and due to adsorption and desorption processes different species have different travelling times to the detector. Instead of a mass spectrometer also flame ionization or thermal conductivity detectors can be coupled to the GC [155].
MBMS and GC-MS provide species selective measurements of hydrocarbons, which are essential for the understanding of soot formation and the validation of combustion models. Yet, besides the drawbacks of probe disturbance inherent to every *ex situ* technique, the major disadvantage is that species with the same molecular weight such as isomers can hardly be discerned. Some fragmentation-based approaches exist but are associated with additional effort. Further, measurements in presence of soot are challenging mainly due to the clogging of the sampling device impeding investigations on most technical flames [64, 156].

2.2.2.3 Soot Classification by Separation-Based Techniques

In contrast to PAHs and molecular species, the measurement of soot concentrations, masses and size distributions is often realized by separation-based techniques. Especially in large emitting devices such as Diesel engines gravimetric filtration-based techniques remain the industrial standard (e.g., ISO 8178-1:2020) based on measurements of the filter's weight increase due to particle deposition [157]. The filter loading can also be monitored by changed oscillation frequencies using a tapered element oscillating microbalance (TEOM) [158] or optically by tracking its blackening

to retrieve the filter smoke number (FSN) [159] (e.g. ISO 10054:1998). In the context of this work, comparative sizing techniques are of special interest.

For the investigation of soot size distributions a scanning mobility particle sizer (SMPS) can be used [160]. It consists of a differential mobility analyser (DMA) for classification coupled with a condensation particle counter (CPC) for quantification. First, the polydispersly distributed soot particles must be extracted from the flame. In many cases the burner stabilized stagnation method is used where the sampling orifice is embedded in the stagnation plate of a premixed burner with variable HAB positions [127, 161]. After sampling a particle neutralizer in form of a Kr-85 or X-ray source is used to ensure a defined charge distribution of the particles. The following DMA classifies the particles of the aerosol by size. Here, the charged particles are accelerated perpendicularly to the aerosol stream direction in an electric field, which is created between a high voltage centre rod and a concentrically surrounding grounded tube. Dependent on the drag forces and thus different electrical mobility, differently sized particles have characteristic travelling traces through the device. A slit at the end of the DMA tube selects a certain particle size in dependence of the applied voltage. The monodisperse aerosol is then guided through a (typically) butanol saturated environment in the CPC where condensation around each particle occurs and droplets are formed. The increased size of the droplets enables optical counting through the scattering of laser light. A voltage scan in the DMA allows the size distribution of the steady aerosol stream to be determined. The detection of small incipient soot particles (<5 nm) requires specialized SMPS devices, which for example have an additional activation stage through diethylene glycol in the CPC to allow for the counting of these small particles [162]. Yet, it is important to keep in mind that the determined size is the mobility diameter d_{m}, which is not directly comparable to the actual particle diameter d_{p} determined by microscopy or optical techniques but rather relates to the aggregate size [145]. Further, precise control of the dilution ratio is required for reliable size distributions [161]. Various studies of size distributions revealed a bimodal shape with one peak <10 nm and one at ~20 nm related to the different species during the soot formation process [163]. In addition to SMPS, particle size distributions can also be determined by the use of an electric low-pressure impactor (ELPI) [164, 165]. Here, electrically charged particles in a gas stream are deposited on several cascade impactor stages and the current/charge is measured if a particle hits an impactor plate. The inferred quantity in this case is an aerodynamic diameter d_{a}, which for fractals is stronger related to the primary particle size compared to the mobility diameter. The combination of d_{a} and d_{m}

measurements additionally yield information on fractal-like dimensions and effective densities of soot [166].

2.2.2.4 Raman Spectroscopy

Raman spectroscopy is widely used to study carbonaceous materials ranging from graphene [167] over soot [168] to its precursor molecules [169, 170]. It is based on inelastic light scattering between a photon and the scatterer (e.g., a gas-phase molecule or a solid), which is described in more detail in the upcoming section 2.2.3. In contrast to elastic scattering (often called Rayleigh scattering), Raman scattering involves a transition of rotational or vibrational energy states of the scatterer and therefore leads to either a red- (Stokes) or blue-shifted (anti-Stokes) scattering signal as a characteristic spectral fingerprint. This fingerprint is comprised of characteristic peaks located at certain Raman-shifts expressed in the unit cm^{-1} and calculated by $\tilde{\nu}_{\mathrm{Laser}} - \tilde{\nu}_{\mathrm{scatter}}$. Yet, the occurrence of these processes is extremely rare, leading to the inherent problem of weak Raman- compared to strong backgrounds signals.

While in recent years some online approaches have been developed [170, 171], the vast number of Raman spectroscopy studies related to the soot evolution process are based on *ex situ* approaches [92]. Therefore, a sampling procedure is demanded, which can either consist of thermophoretic sampling similar to TEM probes [172, 173] or in many cases is based on extraction from the flame using a vacuum pump and deposition on quartz fibre filters [174, 175]. The sampling substrates require low Raman and fluorescence background signal.

Raman signals are used to investigate the structural properties of soot particles linked to their maturity. The spectra of soot (see manuscript [M2] Fig. 7) exhibit two characteristic peaks referred to as D (~1325 cm^{-1}) and G (~1600 cm^{-1}) band (first order) and a second-order 2D peak between 2300 cm^{-1} and 3300 cm^{-1}. The width of the 2D peak yields information about the stacking order of the BSUs [175]. From the intensity ratio of the D to G peak the conjugation length L_a can be obtained, based on a relationship described by Ferrari and Robertson [176]. Further, from the decomposition of the measured first-order spectrum the individual peaks refer to certain properties such as the defect density. A remaining inconsistency is the number of peaks fitted to the measured spectra as addressed by Herdmann et al. [177] and was found to vary between two to six peak models for soot [178] but can involve up to eight peaks for char [179]. The photoluminescence background can be used as an indicator of organic carbon content (with fluorescing properties) to total sp^2 carbon content by dividing the slope of the photoluminescence background by the G peak intensity [180, 181]. Therefore, the

slope of the photoluminescence background decreases with increasing soot maturity. In many cases, Raman measurements are applied to investigate soot oxidation as the graphitization can directly be followed [27].
Additional focus should be put on the dependency of the polarization of the excitation laser and the Raman signal, which should be sensitive to the structural order of the material [182]. A recent work by Kim et al. [183] used a polarization-based background suppression method pointing towards *in situ* capable approaches for simultaneous determination of multiple gas phase molecules in a sooting flame.
Besides the investigation of soot particles by spontaneous Raman scattering, coherent anti-Stokes Raman scattering (CARS) spectroscopy must be mentioned as a powerful nonlinear *in situ* thermometry technique. It is based on the interaction of three laser pulses and a targeted molecule to generate a fourth frequency, which contains the temperature information in the form of the population distribution of the molecule's energetic levels. Various forms of CARS have been developed over the years [184, 185], with the typical advantages of comparably strong signals, high accuracy and precision (in the order of ~2% of the measured values) and a high spatial resolution.

2.2.3 *In situ* Techniques Related to the Soot Evolution Process

As previously mentioned, a major disadvantage of any sampling-based method is the interference or even disturbance of the underlying process [64]. In the case of sooting flames this may take the form of sampling bias towards certain particles, the ongoing reaction of less stable species along the sampling path, local temperature drops causing changed kinetics or sheer changes linked to the flow fields and fluid dynamics. Therefore, *in situ* techniques are extremely valuable tools as their almost non-intrusive nature can be used to gain information from the actual processes taking place [93, 122]. Yet, some forms of *in situ* diagnostics using strong laser pulses may influence the soot particles through effects such as annealing, sublimation or precursor restructuring [186-188].
In this section, an overview of several *in situ* techniques is provided. While some X-ray or neutron-based techniques are discussed, the vast number of *in situ* diagnostics are optical techniques [189]. Besides the self-occurring emission of light from molecules or particles through chemiluminescence or thermal radiation (e.g., Figure 2.3), the use of light excitation at specific wavelengths (typically provided by lasers) builds the basis for most optical diagnostics. The interaction between light and matter can take several forms and is summarized in simplified form in Figure 2.8.

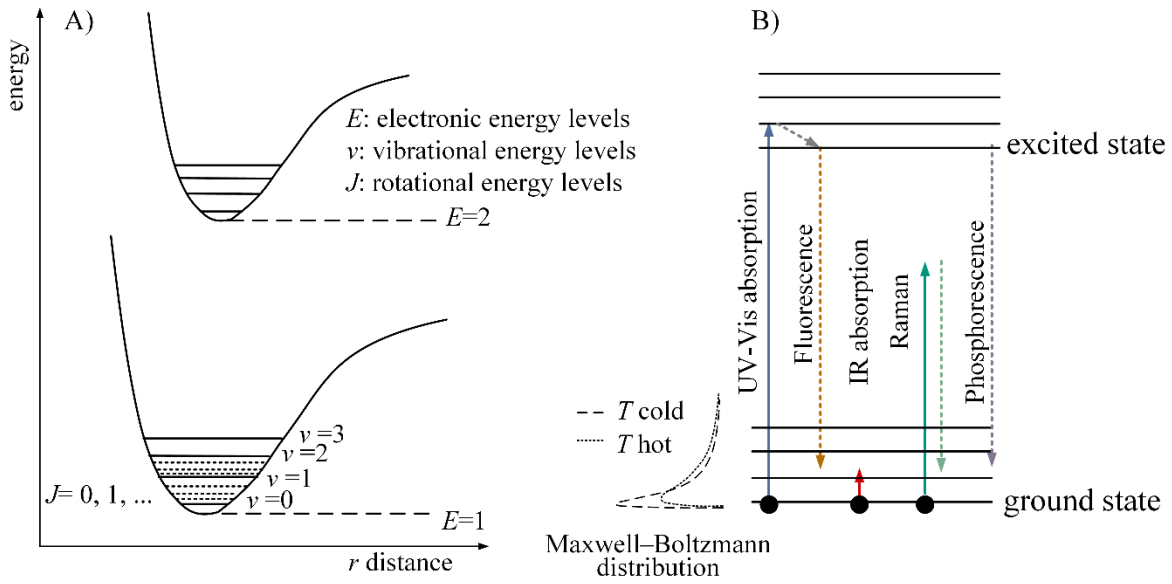

Figure 2.8: A: Simplified energetic levels for an exemplary molecule or particle. B: Possible phenomena occurring by the interaction of the molecule/particle with photons.

Applying sufficiently strong laser pulses or light intensities can result in the formation of a plasma with characteristic line emissions for each species as well as a broadband Bremsstrahlung background. This laser-induced breakdown spectroscopy (LIBS) can be used for species assignment [190] or can also be performed in a phase-selective manner to follow the transition from gas-phase to solid particles, especially for metal oxide nanoparticles in flame synthesis [191, 192]. For light intensities below the breakdown threshold, one possibility is that incoming photons scatter elastically on the particle or molecule leading to a change of the photons' directions while maintaining the wavelength. The angular dependent characteristic scattering pattern yields information on quantities related to the size and morphology. A second possibility involves a change in wavelength between incoming and emitted photons, so that one can experimentally distinguish between excitation and emission signals. For an exemplary and hypothetical molecule as depicted in Figure 2.8 different energetic levels exist, ranging from rotational, over vibrational to electronic levels. An incoming photon of a certain wavelength can interact with the molecule in the form of an absorption event leading to an electron being lifted from the ground state to an excited state as well as an increase in the internal energy and therefore heating of particles. Dependent on the energy of the photon (given in the unit eV), which is directly related to its wavelength via $E_\gamma = \frac{c \cdot h}{\lambda \cdot e}$ this excitation can occur between vibrational levels (infrared photons) or electronic levels (typically UV-Vis photons). Here, $h = 6.626 \cdot 10^{-34}$ J·s is Planck's constant, $c = 299792458$ m·s^{-1} the speed of light in vacuum and $e = 1.602 \cdot 10^{-19}$ C

the elementary charge. In the case of (mainly UV-Vis) absorption the relaxation of the excited electronic state can lead to the emission of a photon; a process named fluorescence. As discussed earlier, the energetic difference of a photon after an inelastic scattering event can be called Raman-shift and derives from , e.g., phonon or molecular rotational and or vibrational excitation (2.2.2.4). Further processes such as phosphorescence, where the lifetime in the excited state is remarkably longer compared to fluorescence, are not discussed in this work as they are not directly related to soot. However, laser-induced phosphorescence can be used for thermometry in seeded aerosol flows or directly on solids such as combustion chamber walls or pistons [193-195]. In addition to optical diagnostics, in recent years some photoacoustic *in situ* techniques were developed that allow to measure, e.g., soot volume fractions [188, 196, 197].

2.2.3.1 X-Ray or Neutron-Based Techniques

A brief overview about various X-ray or neutron-based techniques used to investigate the soot formation process is provided in this section. It should be mentioned that the different techniques are hardly comparable to each other as they resolve different quantities related to the formation of soot. Yet, they all have in common that they are either based on X-rays and therefore electromagnetic radiation with wavelengths far below the optical techniques or neutron radiation.

Small-angle X-ray scattering (SAXS) is a common technique to determine the average aggregate morphology as well as the particle size distribution of soot in flames [198, 199]. It is based on the elastic scattering of X-rays at the electrons of the material. Dependent on the particle shape and size a characteristic scattering pattern is observable. In case of *in situ* soot measurements, usually size distributions and random orientations of the particles and aggregates are given, leading to a superposition of several scattering patterns and therefore a radial symmetric distribution of the scattering intensities. After a rotational averaging of the images the resulting one-dimensional scattering intensity can be plotted versus the scattering vector. The experimental setup consists of a collimated and monochromatic X-ray beam that is shone through the flame on a detector. A beamstop of the initial beam size blocks the transmitted section of the incident beam and defines the smallest angles resolvable together with the distance between flame and detector. In most cases, this distance is adjustable, which is used to resolve different size ranges of the particles [200]. The scattered X-rays hit a 2D detector and show the amplitude of the Fourier transform. As mentioned before, the one-dimensional scattering curve can be extracted from those images and a regression

between this measured curve and a modelled one allows to infer the underlying particle size distributions. One drawback of the technique lies in the dependency on typically large-scale synchrotron devices. Further, SAXS is limited to particles smaller ~150 nm and requires consideration of background scattering of gas molecules [201]. Yet, SAXS is a valuable tool to determine soot size distributions and can be combined with other techniques for a comprehensive analysis [120].

The combination of SAXS and wide-angle X-ray scattering (WAXS) additionally yields information about the internal atomic structure of soot particles, e.g., clustering, stacking or the level of graphitization [202]. Moreover, *in situ* WAXS measurements can be used to indirectly infer the species composition (e.g. H_2O, CO_2, CO, C_2H_2, C_2H_4) and temperature by the comparison of experimental and modelled scattering curves [203]. Experimentally, the required larger scattering angles (resulting in higher resolution) in comparison to SAXS can be achieved by simply placing the detector closer to the sample.

X-ray absorption (XAS) based on the interaction of monochromatic X-rays and core electron excitation can be used to investigate the aliphatic and aromatic content of soot as well as surface functional groups [204]. It should be mentioned that the vast number of XAS experiments are performed on sampled probes, yet, there are some *in situ* [205] (under specific low pressure conditions) or online in-flight approaches [206]. Additionally, X-ray photoelectron spectroscopy (XPS) is a prominent technique to determine quantities as surface hybridization (sp^2 / sp^3), defect ratios [121] or the work function [206] and therefore allows insight to the maturity level of soot particles. Again the technique is almost solely used in an *ex situ* manner and listed here to facilitate the reader's further research [92]. X-ray Raman spectroscopy (XRS) can complement XAS approaches by providing information about disorder and carbonization [207].

An additional *in situ* technique is based on the scattering of a neutron beam and benefits from reduced background influence and the capability of measuring in denser environments compared to X-ray scattering [208]. Yet, the basic principle and the determined quantities are similar to SAXS approaches.

2.2.3.2 Laser-Induced Fluorescence

As schematically depicted in Figure 2.8 B, laser-induced fluorescence (LIF) is based on absorption of a laser pulse for excitation (typically at UV wavelengths) and detection of the spectrally shifted fluorescence emission occurring during relaxation. The wavelength shift of the emission signal is mainly caused by vibrational relaxations in the exited state leading to decreased energy differences and therefore a red- or Stokes

shifted photon. In case of higher occupied ground state levels (e.g., through elevated temperatures of the molecules) the emission signal can also result in a blue shift as the electron falls back to a lower energy level compared to its initial state. This process is referred to as anti-Stokes fluorescence. Further, non-radiative energy conversion processes of the excited state through intersystem crossing (ISC), internal conversion (IC) or quenching through collision with molecules such as oxygen are known to occur and make it difficult to obtain absolute quantitative results based on the fluorescence efficiency.

LIF is widely used to resolve combustion species and intermediates such as PAHs, formaldehyde (CH_2O), C_2 [209], OH or NO [210]. It can either be used for pointwise and spectrally resolved measurements [211] or as a 2D [212], 3D [213] or even highly temporally resolved 4D [214] technique to obtain species maps and concentration fields [215]. Some forms of LIF (e.g., NO-LIF or atomic-LIF [216, 217]) can be used for thermometry as the temperature is directly related to the population distribution of the energetic states for the targeted species. Typically, the use of two excitation wavelengths is required to cancel out effects such as self-absorption and varying concentrations in the measurement volume by using the ratio of both signals. While the determination of OH fields is particularly relevant for the oxidation processes in flames, this section focuses on the use of LIF for PAH detection as it directly relates to the formation of soot particles.

As shown by Bejaoui et al. [218] by using a wavelength tuneable optical parametrical oscillator (OPO) laser in a methane premixed flame, PAHs in flames can fluoresce up to an excitation wavelength of 680 nm, a fact that becomes relevant for other emission-based techniques such as LII. The resulting fluorescence spectra reveal a rather broad characteristic resulting first from the coexistence of multiple PAH species at the measurement location and second from the broadening of the spectra at elevated flame temperatures through increased occupation of higher energetic levels. Quantitative evaluations of certain species therefore requires a decomposition of the sum signal [219, 220]. To overcome the drawback of the temperature broadening, jet-cooled LIF was developed, where the species are extracted from the flame and cooled down rapidly leading to LIF spectra with specific spectral characteristics facilitating assignments to certain PAH classes [156]. However, this approach is just capable online but not *in situ*. The fact that the absorption and fluorescence spectrum of larger PAHs is shifted to longer wavelengths can be used to qualitatively follow PAHs growth by utilizing two spectral detection windows [221]. In many cases PAH-LIF is also combined with LII as an imaging technique (using a laser light sheet) relating the formation of the solid

particles from the precursor molecules [222-224]. In 1997 Vander Wal and coworkers reported the existence of a transition zone (called “dark zone”) between the PAH fluorescence and the soot incandescence regions and attributed these to the presence of soot precursor particles [225]. To investigate this region, a technique based on the fluorescence lifetime, which is typically in the order of several tens of nanoseconds, was developed. Precisely, the use of a short laser pulse (femto- or picosecond) and the detection of the LIF signal decay at both polarization directions can be used to follow the Brownian motion of the soot precursors. The latter is related to their average size as the anisotropy of the polarization takes longer for larger species [226]. These approaches named time-resolved fluorescence anisotropy (TRFA), however, require cost intensive experimental set-up and therefore somehow have vanished over the last few years.

2.2.3.3 Elastic Light Scattering

Based on similar principles as SAXS, elastic light scattering (ELS) can be used to determine the size and morphology of aggregates or particle ensembles such as soot [227]. Light of a specific wavelength scatters at the aggregates resulting in a characteristic scattering pattern with an angle-specific intensity distribution. The scattering pattern over scattering angle θ depends on the aggregate size R_g, the utilized laser light wavelength λ and its polarization. For a detailed description the reader is referred to the work of Sorensen [227] where the structure factor of the scattering wave vector $q = \frac{4 \cdot \pi}{\lambda} \sin\left(\frac{\theta}{2}\right)$ is described as

$$S(q) = e^{-\frac{(q\,R_\mathrm{g})^2}{D_\mathrm{f}}}\ {}_1F_1\left(\frac{3 - D_\mathrm{f}}{2}, \frac{3}{2}, \frac{(q\,R_\mathrm{g})^2}{D_\mathrm{f}}\right). \tag{3}$$

Here, ${}_1F_1$ is the hypergeometric function. Exemplary scattering patterns in one plane are depicted in the polar plot of Figure 2.9 A (intensities in log-scale) calculated for three different aggregates with a fractal dimension of D_f=1.78 and a size of R_g=100 nm, 300 nm and 500 nm, respectively. The upper half of the polar plot shows the ⊥-polarized scattering intensity, the lower half the ∥-polarization with incoming laser light (532 nm) from the left side. For discrete detection angles the scattering pattern can be converted to a scattering curve plotting the scattering intensity versus q. Different regimes allow to infer different quantities and are schematically shown in Figure 2.9 C. It should be mentioned that the signals depend on the scattering at the aggregate

structure as given in Equation (3) as well as from scattering at the primary particles as Rayleigh scatterers. The latter have a $\cos^2\theta$ dependency if the incident light is polarized parallel to the scattering plane (denoted by ∥). The information about R_g is contained in the Guinier regime, while D_f derives from the Power-law region.

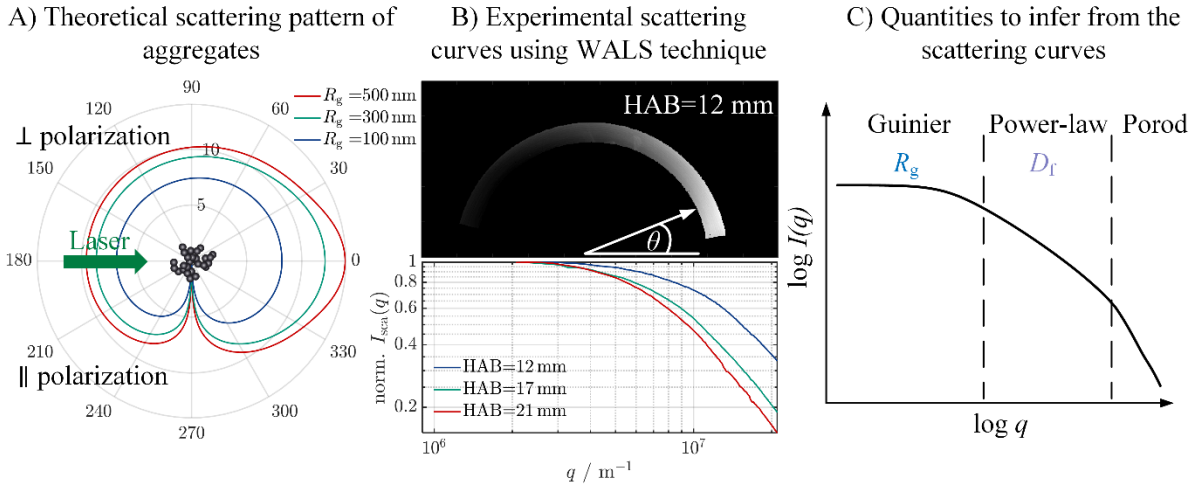

Figure 2.9: A: Calculated scattering patterns in logarithmic scale for three differently sized aggregates (R_g=100 nm, 300 nm, 500 nm) with a D_f=1.78 and a laser wavelength of 532 nm following Sorensen [227]. B: Experimental scattering data taken in a premixed C_2H_2/air flame with an equivalence ratio ϕ=2.7 (see Figure 2.7) at different HABs using WALS apparatus described in detail in [228] and converted to scattering curves. C: Different regimes of the scattering curves and related quantities.

Experimentally, ELS can either be applied as a pointwise or a 2D measurement [229, 230]. For pointwise measurements the use of an ellipsoidal-shaped mirror segment facilitates to capture a wide angular range (10°-170°) with a high-angular resolution and therefore is referred to as wide-angle light scattering (WALS) [231]. Here, the measurement volume in one focal point of the ellipsoid is spatially filtered by an aperture in the second focal point and imaged on a camera [232]. Figure 2.9 B shows one mirror-half illuminated by the scattered light of soot aggregates in a C_2H_2/air premixed flame at ϕ=2.7 and 12 mm HAB. Below, the intensity is converted to the scattering plot with two additional HAB positions. Due to an ensemble of aggregates in the imaged scattering volume the radius of gyration has an effective character and is typically biased towards larger aggregates dominating the scattering signal. This fact requires a deconvolution of the signal to obtain the aggregates' size distribution parameters (assuming log-normal distribution) as shown by Huber et al. [231]. Further, the interpretation of scattering signals suffers from the changed sizes of the observed measurement volumes with varying angle of detection and can, e.g., be solved by appropriate calibration with isotropic scatterers [233] or by planar light sheet utilization [234]. A comparison between WALS measurements (shown in Table 4.1 of Section 4.3)

and TEM data of Figure 2.7 at HAB 17 mm with resulting R_g=207 nm reveal a discrepancy. This highlights that a comparison of *in situ* and *ex situ* data is not straightforward. A possible explanation could be the preferable deposition of larger aggregates at the TEM grid during the sampling or image analysis procedure [235].
For 2D measurements multiple cameras at fixed angular positions [230] or a rotation of the 2D detector around the measurement volume is required [236]. The former benefits from the capability of simultaneous acquisition at the expense of numerous experimental devices. These approaches are termed multi-angle light scattering (MALS). The definition of the scattering vector also makes it possible to fix the angle of detection θ and instead use broadband light and therefore a variation of λ as shown by references [237-239]. An inherent limitation of ELS approaches is the occurrence of multiple scattering in optically thick measurement environments. It means that the scattered light in the measurement volume is scattered again on its way to the detector. Here, the polarization ratio (∥ to ⊥) yields information on the relative amount of multiple scattering as the latter leads to an increasing anisotropy [227].
For a comprehensive picture of soot aggregates, the combination of ELS and a primary particle sizing techniques such as LII or TEM is desirable in context of Equation (2) [240, 241]. At the same time particle sizing with LII benefits from knowledge about the aggregate morphology from ELS measurements as laid out in detail in manuscript [M3].

2.2.3.4 Absorption Spectroscopy

For decades absorption spectroscopy has been a powerful diagnostic tool to investigate reactive flows such as combustion processes regarding various QoI [242, 243]. The technique is based on the attenuation of light, which can be described by Beer-Lambert's law relating the absorbance

$$A(\lambda) = -\ln\left(\frac{I(\lambda)}{I_0(\lambda)}\right) = \int_0^L \alpha(\lambda, x)\,\mathrm{d}x \qquad (4)$$

with the incident $I_0(\lambda)$ and transmitted $I(\lambda)$ light intensities, based on the assumption that Rayleigh scattering of small particles or molecules can be neglected (i.e. that the extinction coefficient σ_{ext} equals the absorption coefficient α) [M2]. In the case of homogenously distributed species along the measurement path, the absorbance can simply be expressed as the product of absorption path length L and the absorption coefficient $\alpha(\lambda)$. As illustrated in Figure 2.8 B it can generally be discerned between

IR and UV-Vis absorption spectroscopy dependent on the energy or wavelength of the photons resulting in the excitation of different energetic transitions.
On the one hand, combustion gases and molecules such as H_2O, CO_2 or CH_4 exhibit characteristic absorption bands in the NIR and the mid infrared (MIR) wavelength region related to their vibrational and rotational transitions. Here, the absorbance can also be expressed by

$$A(\lambda) = \int_0^L \alpha(\lambda, x)\,\mathrm{d}x = p \int_0^L X_i(x) \cdot S_{\mathrm{abs}}\big(T(x)\big) \cdot \varphi_v\,\mathrm{d}x, \tag{5}$$

where p is pressure, X_i the absorbing gas mole fraction, S_{abs} the temperature dependent line strength and φ_v the line shape function. The latter is typically described by a Voigt profile as the convolution of a Gaussian and a Lorentzian line shape. Equation (5) in combination with absorption line databases can be used to model the absorption spectra of these gases for various conditions (e.g., Figure 2.10) and a comparison with measurements enables to determine QoI such as temperature [244], species concentration or even pressure [245]. To resolve the absorption peaks it is required to measure a certain wavelength range. This is either realized by scanning in time domain using tuneable diode laser absorption spectroscopy (TDLAS) [246] or broadband supercontinuum laser absorption spectroscopy (SCLAS) [245]. The latter typically benefits from covering a broader spectral range allowing for high-speed multiparameter and multispecies determination. Yet, the expense of these broadband light sources in combination with IR detection equipment such as line cameras or very fast oscilloscopes makes TDLAS set-ups attractive for a broader span of applications. An inherent disadvantage of absorption spectroscopy is its line-of-sight (LOS) nature and a loss of spatial information along the measurement path. This problem is typically overcome by combining the technique with tomographic reconstruction [247]. Here, the detection of multiple paths builds the basis to computationally reconstruct the underlying species maps, which is an ill-posed problem and often requires advanced statistical methods such as Bayesian approaches (see also manuscript [M3]) and regularization [248]. Besides the ability of using IR absorption spectroscopy to characterize combustion products as well as the key parameter temperature, the technique is especially interesting with respect to the soot formation process and the detection of C_2H_2 as the intermediate precursor molecule responsible for PAH and surface growth through the HACA mechanism. As described in the previous sections, a detailed understanding of the interplay of all the species is required to ultimately

improve the understanding about soot formation. This makes IR absorption spectroscopy a valuable tool to set a comprehensive framework.

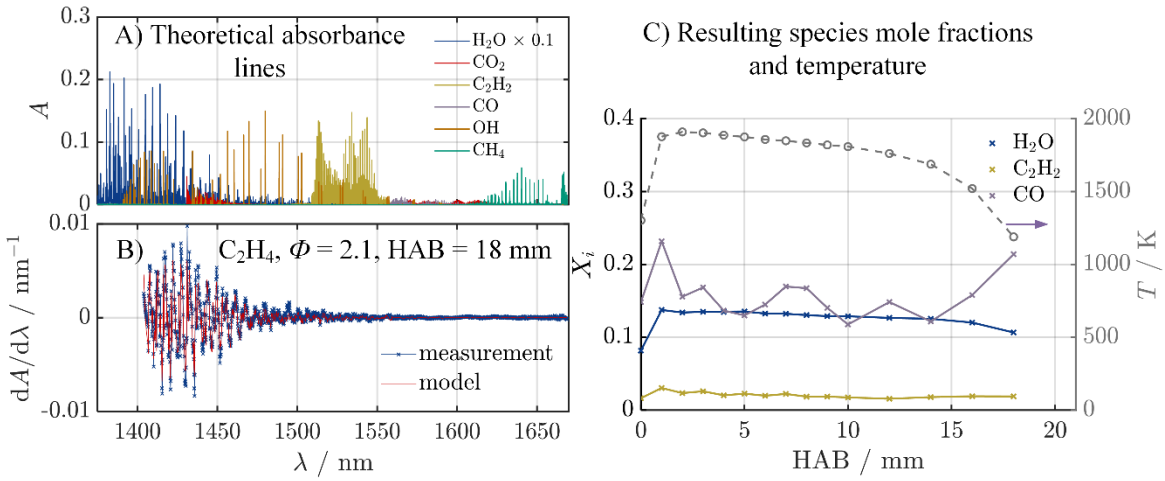

Figure 2.10: A: Theoretical absorbance lines of various combustion gas species in a wavelength range from 1375 nm to 1670 nm. B: Broadband measurement in a C_2H_4/air flame at ϕ=2.1 and HAB=18 mm together with the model fit. C: Resulting species mole fractions and temperature over HAB.

Figure 2.10 A shows the absorbance lines of six combustion-related molecules in a wavelength range from 1375 nm to 1670 nm taken either from the database HITRAN [249] (C_2H_2) or HITEMP [250]. The diagram below shows the derivative over wavelength of the broadband absorbance spectrum taken in a ϕ=2.1 premixed C_2H_4/air flame at a HAB of 18 mm together with the model fit. A detailed description of the evaluation routine and the measurement set-up can be found in reference [245] showing the multi-pass Herriott-cell, which was aligned to achieve 17 passes through the flame in one horizontal plane. The derivative is used to reduce broadband baseline signals mainly resulting from fluctuations of the light source intensity, however, at the expense of measurement noise amplification. From the regression of measurement and model the underlying species distributions of H_2O, C_2H_2, CO and the temperature shown in Figure 2.10 C can be inferred, providing an excellent experimental *in situ* tool to validate simulation results as displayed in Figure 2.1. It should be kept in mind that the idealized simulation settings of an adiabatic flame reactor can hardly be compared to the measurements in a premixed flame, e.g., the stabilization plate mounted at 21 mm HAB will influence temperature and species profiles. However, the temperature and species profiles are quite well-pictured regarding the absolute values [251]. Other species such as CO_2 or OH can hardly be extracted from the measurements. This can be explained by the spectral resolution of the spectrometer in combination with the narrow line width of these species at atmospheric pressure. In addition, the spectral overlap of

these species with strong H_2O absorption bands in the regarded wavelength range further complicates their determination. In recent years, IR absorption spectroscopy has developed more towards longer wavelengths in the MIR, especially with the availability of suitable quantum cascade lasers (QCLs) [252]. Here, stronger absorption bands of more species such as, e.g., aromatics, are accessible and spectral separation between the species facilitates the evaluation [253].

On the other hand, PAHs show absorption in the UV-Vis region [254, 255] and soot particles absorb over a broad spectral range from UV to IR [256, 257]. The wavelength dependence of the latter relates with maturity mainly linked to the fine structural composition of the particles and in general shows a decreasing trend of the absorption coefficient towards longer wavelengths. UV-Vis absorption measurements can therefore be used to infer several QoI of PAHs and soot related to the soot formation process. In this work, *in situ* UV-Vis absorption spectroscopy measurements built the basis to estimate PAH distributions in premixed flames [M1] and retrieve the optical band gap E_g of soot in a non-premixed coflow flame [M2]. Details are provided in the respective manuscripts. Yet, the technique is also widely used to infer further parameters such as $E(\tilde{m}, \lambda)$ [28], the dispersion exponent ξ [258] or f_V as will be discussed in this section.

Extinction or laser extinction (LE) measurements (often in the visible wavelength range) are widely used to determine the soot volume fraction in flames. The simplest form is based on Equation (4) at one specific wavelength. From the path averaged absorption coefficient and with the Rayleigh assumption that the size of the particles is small compared to the laser wavelength, f_V can be obtained following

$$f_V = \frac{\alpha \cdot \lambda}{6 \cdot \pi \cdot E(\tilde{m})}. \tag{6}$$

For reliable results several factors should be considered. First, knowledge about the optical properties in form of $E(\tilde{m}) = -\Im\left(\frac{\tilde{m}^2-1}{\tilde{m}^2+2}\right)$ are required, where $\Im$ is the imaginary part. Second, in case of non-homogenous distributions along the LOS path, an inversion procedure is demanded to obtain the local absorption coefficients. For radial symmetric objects such as many flames this can take the form of an inverse Abel transform [259]. Further, the extinction signal is the sum of scattering and absorption and the latter can derive from soot particles or soot precursor structures such as PAHs [260]. In many cases the contribution of scattering to the overall attenuation is assumed to be small and therefore negligible [261, 262]. For a closer look at the influence of scattering on the

absorption signal the reader is referred to manuscript [M2]. The influence of PAH absorption can be avoided by utilizing longer wavelengths in the visible or a shift towards the IR wavelength range. Figure 2.11 shows broadband extinction measurements from 700 nm-1000 nm (solely attributed to soot) in a standard non-premixed coflow flame at HAB=42 mm. The signals $I(\lambda)$ and $I_0(\lambda)$ are background corrected and with the absorption path length L (extracted from flame photographs), α can be calculated based on Equation (4). Using the wavelength dependent $E(\tilde{m},\lambda)$ values reported by Yon et al. [263], Equation (6) can be used to infer f_V as displayed in the right diagram, revealing an almost constant value of ~4 ppm over all wavelengths.

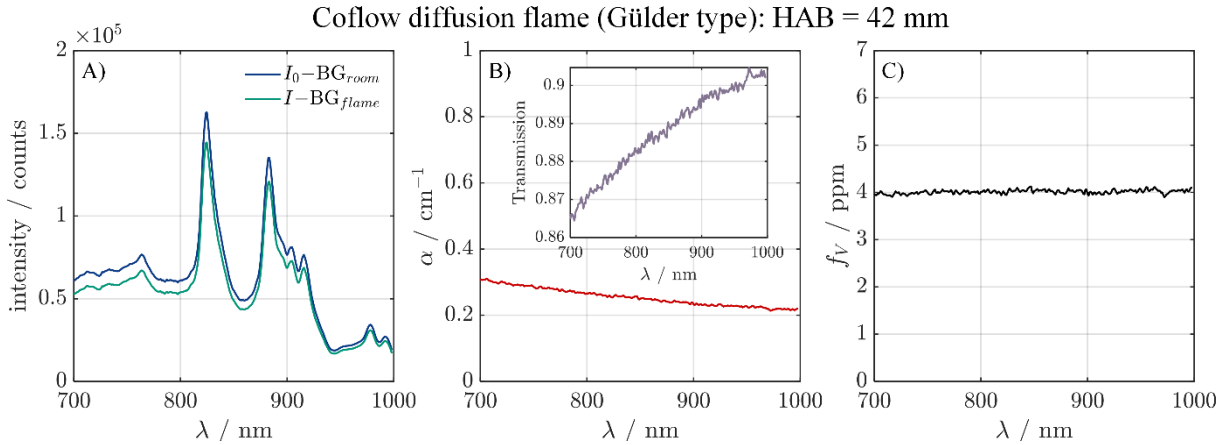

Figure 2.11: A: Background corrected intensities. B: Resulting transmission and absorption coefficient α using absorption length L evaluated from flame images. C: Resulting soot volume fraction using $E(\tilde{m},\lambda)$ from Yon et al. [263]. Data taken in a non-premixed coflow ethylene/air flame at HAB=42 mm.

With the use of LE at multiple wavelengths further information about the optical properties of soot can be obtained [258]. Equation (6) is based on the common assumption of an $\alpha \propto \lambda^{-1}$ proportionality, which is valid for mature soot particles. However, for young soot $\alpha \propto \lambda^{-\xi}$ relationships lead to ξ values larger than 1.0 [262, 264, 265]. This parameter, named dispersion- or Ångström exponent, therefore accounts for the wavelength dependency of the absorption coefficient and also emissivity assuming the validity of Kirchhoff's law in thermodynamic equilibrium. An evaluation of the absorption coefficient displayed Figure 2.11 leads to ξ=1.02 and therefore a value close to mature soot. In case of a known f_V from, e.g., complementary measurement techniques as SMPS, Equation (6) can also be used to infer wavelength dependent $E(\tilde{m},\lambda)$ from broadband absorption measurement [263, 266]. The link between the dispersion exponent and the wavelength dependency of the absorption function is given by [28]

$$E(\widetilde{m},\lambda) = \lambda^{1-\xi} \cdot \frac{\beta}{[6 \cdot \pi \cdot f_V]}, \quad (7)$$

where β is a scaling constant. The LE measurements can also be applied in a 2D manner using volumetric illumination of the flame [264, 267]. In some cases, and especially in atmospheric research, the mass absorption cross-section (MAC) as a specific quantity with the unit $m^2 \cdot g^{-1}$ is utilized as the absorption coefficient divided by the partial density of the absorbing mass [8, 268, 269]. The latter is defined as the product of volume fraction f_V and the solid density ρ. Several recent studies reported a mass and thus size dependency of the absorption cross-section, concluding various reasons such as internal scattering or quantum confinement effects [270-273]. The results by Corbin et al., however, indicate that it might mainly be linked to the size dependent degree of graphitization of the soot particles [268].

In the UV wavelength range of the electromagnetic spectrum, PAHs show absorption bands based on their π-π* transitions [274]. Larger PAHs show broadened absorption towards the visible as the energetic separation between highest occupied molecular orbital (HOMO) and lowest unoccupied molecular orbital (LUMO) decreases. This in principle can be used to discern between different size classes by the evaluation of wavelength scanning or broadband UV-Vis spectra. Similar to IR approaches, a comparison of the measured absorption spectra to the sum of those of individual species provides insight to their distribution in the measurement volume [275]. However, an assignment to specific PAHs is complicated by the fact that the absorption peaks broaden at flame temperature and the availability of spectroscopic data is limited. A more detailed description can be found in manuscript [M1]. Similar approaches in the UV wavelength range are used for *in situ* measurements of potassium in flames and might further be applicable for NO determination [276].

2.2.3.5 Pyrometry and Laser-Induced Incandescence

Prior to the discussion about signals from thermal radiation after laser heating, the natural incandescence of soot particles at flame temperatures already provides insight to several QoI such as temperature or volume fraction [277]. As the intensity of the thermal radiation signal is a function of temperature and the wavelength position of the emission maximum, its detection at two or multiple wavelengths can be used to resolve temperature fields by ratio pyrometry [82, 278]. Here, one must account for the optical properties of soot and its deviation from an ideal black body. This is often expressed by the emissivity ε_λ, which can be phrased by the Rayleigh approximation

$\varepsilon_\lambda = 4 \cdot \pi \cdot d_\mathrm{p} \cdot E(\widetilde{m})/\lambda$ if $d_\mathrm{p} \ll \lambda$. However, using the emissivity is not a preferred formulation as it defines the efficiency of a surface emitting radiation. In case of soot nanoparticles the particle wave interaction occurs volumetrically and therefore the absorption cross section $C_\mathrm{abs} = \pi^2 \cdot d_\mathrm{p}^3 \cdot E(\widetilde{m})/\lambda$ should be used [279-281]. The resulting wavelength dependent incandescence signal of a single soot particle at temperature T captured by a detector can therefore be expressed by

$$S_{\mathrm{LII},\lambda}(T) = C_\mathrm{det} \cdot C_\mathrm{abs} \cdot I_{\mathrm{b},\lambda}(T) = C_\mathrm{det} \cdot C_\mathrm{abs} \cdot \frac{2\pi hc^2}{\lambda^5 \cdot \left[\exp\left(\frac{hc}{\lambda k_\mathrm{B} T}\right) - 1\right]}, \tag{8}$$

where $I_{\mathrm{b},\lambda}(T)$ is Planck's function for a blackbody, k_B is Boltzmann's constant and C_det a constant accounting for detection efficiency. For temperature determination typically the ratio of two signals following Equation (8) integrated over two different wavelength intervals is used. Due to this ratio it is irrelevant if the emissivity or the absorption cross section is used to account for the optical properties of soot particles. In both cases everything but $E(\widetilde{m})/\lambda$ cancels out from the respective definition. The detection device must be calibrated regarding its wavelength dependent response, which is typically realized by placing a reference light source of known spectral irradiance in the measurement volume [282]. The principle of two colour pyrometry together with an exemplary measurement in a premixed C_2H_4/air flame at ϕ=2.1 is depicted in Figure 2.12. On the left side, a comparison between the emissive power of a black body (solid lines) and soot particles (dashed lines) for four different temperatures is displayed. With the detection of flame images at two spectral bands (here centre wavelengths at 561 nm and 700 nm with filter transmission curves shown in subplot C), temperature values can be obtained by comparing the calibrated intensity ratio of each pixel to the calculated ratio shown in Figure 2.12 B. As can be seen in Figure 2.12 D, a decrease of the temperature with increasing HAB can be observed similar to the temperature profile of Figure 2.10. However, the technique is limited to regions where soot particles exist and shows some dependency according to the choice of spectral detection, which leads to higher uncertainties compared to other thermometry approaches. Yet, pyrometry measurements can be used to determine the flame temperature assuming thermal equilibrium between gas and soot particles.

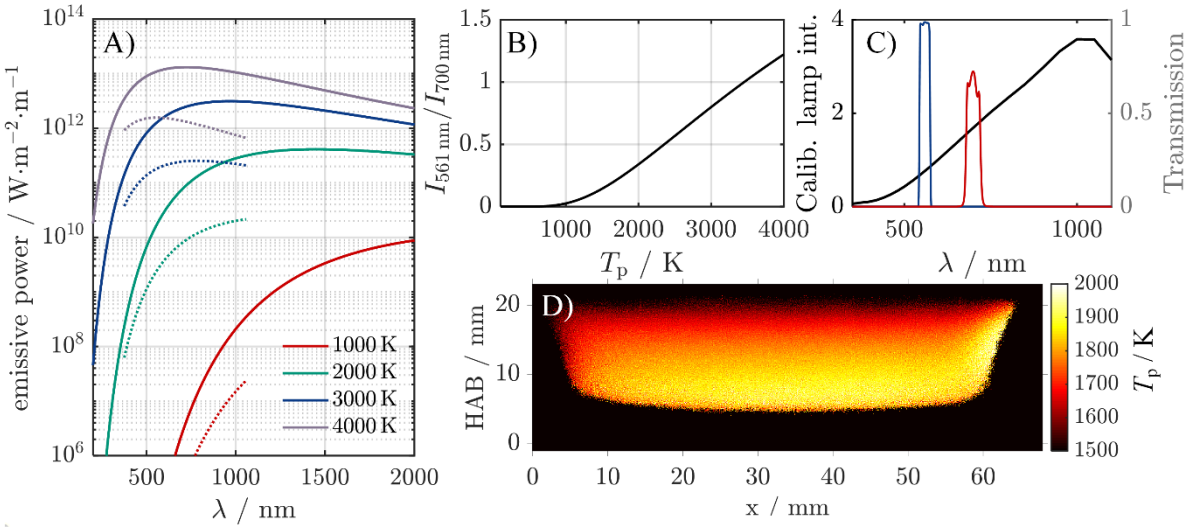

Figure 2.12: A: Emissive power over wavelength for a blackbody (solid) and for a soot particle using ε_λ for 20 nm and an $E(\widetilde{m},\lambda)$ from Yon et al. [263] (dashed) for four temperatures. B: Intensity ratio of two signals following Equation (8) for 561 nm to 700 nm bandpass filters (depicted in C) as a function of temperature. C: Calibration source intensity over wavelength and transmission curves of the bandpass filters. D: Resulting temperatures in a premixed C_2H_4/air flame at ϕ=2.1.

Laser-induced incandescence is based on heating an ensemble of particles in an aerosol by a short laser pulse and detection of the subsequent incandescence signal, while particles equilibrate to the initial gas temperature [283]. It is widely used for various nanoparticle materials such as metals, metal oxides, semiconductors or even few-layer graphene flakes [281, 284-288]. However, a large number of LII experiments and diagnostic development is related to soot due to its suitable absorption and emission characteristics close to a black body and the advantage that soot does not melt but directly sublimates at elevated temperatures. From the laser-induced incandescence signal multiple QoI can be inferred, including the soot volume fraction f_V, the primary particle size d_p and the particle temperature T_p thus making LII a valuable *in situ* tool to investigate the soot evolution process.

Starting with the laser pulse: Commonly nanosecond pulse lasers, e.g., Nd:YAG at 1064 nm or frequency doubled 532 nm are used, with the former being preferred to avoid interference of PAH fluorescence [289]. The temporal pulse shape of these lasers is typically Gaussian-like with a full width at half maximum (FWHM) between 5 ns-10 ns. There are some picosecond- [290, 291] and multiple continuous-wave (CW) laser approaches [292], however, this work focuses on the use of nanosecond pulses. The laser pulse is partially absorbed by the soot particles leading to their heating and an increased thermal radiation or incandescence signal, which is captured by a detection device. For detection either photomultiplier tubes (PMT) with high temporal sampling

rates or cameras (typically short gated and intensified) can be utilized. Here, it can be discerned again between spectrally filtered detection by using bandpass filters or spectrally resolved measurements using, e.g., spectrographs [293]. Considering the spatial expansion of the laser pulse (defining the measurement volume) different dimensionalities of the measurements can be achieved, ranging from pointwise- (0D) [294], to imaging- (2D) [295] or even volumetric (3D) approaches [296]. As highlighted in the previous sections, the turbulent nature of most applicative flames requires to either "freeze" the process with single shots or using high temporal repetition rates utilizing burst-mode lasers [297]. This led to the development of various high-speed (HS) imaging approaches [298, 299]. Their combination with 3D tomography reconstruction is typically referred to as 4D measurements [300]. These types of measurements so far were mainly performed for the determination of soot volume fraction fields. In case of 3D primary particle sizing approaches an average constant flame temperature for the entire flame was considered [301]. Reliable 3D/4D determination of temperatures and particle sizes is still pending.

To illustrate how the QoI can be inferred from the incandescence signal some exemplary measurements are discussed in this section, starting with the determination of f_V. Figure 2.13 shows multiple time-resolved (TiRe) LII measurements in a premixed C_2H_2/air flame using a 532 nm excitation laser and a PMT equipped with a bandpass filter (centre wavelength 650 nm, FWHM 40 nm) for detection.

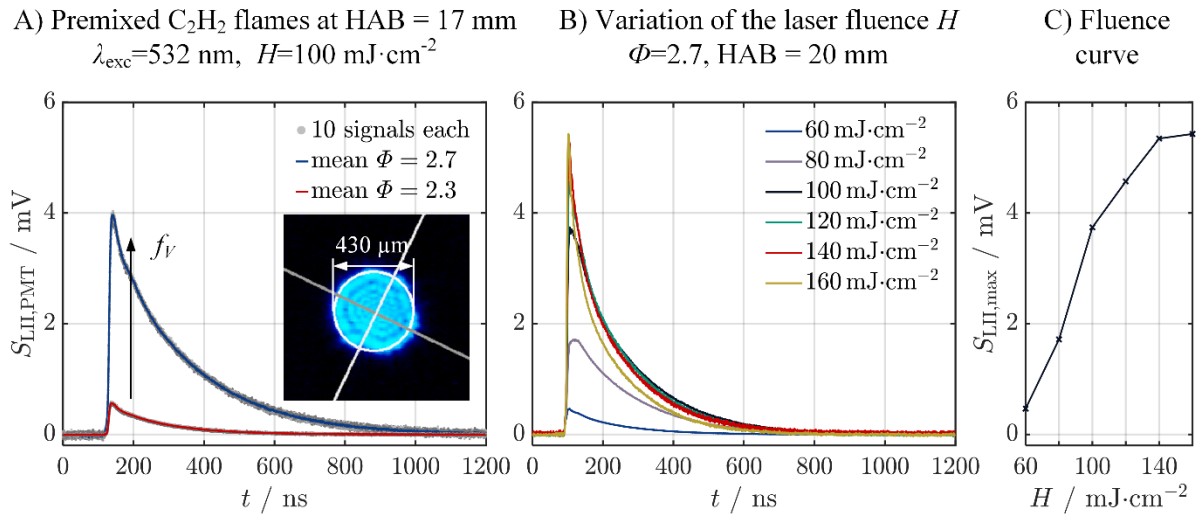

Figure 2.13: A: TiRe-LII signals taken in premixed C_2H_2/air flames with ϕ=2.3 and ϕ=2.7 at HAB=17 mm using 532 nm excitation at a fluence of H=100 mJ·cm^{-2}. Inset shows the laser profile. B: Variation of the laser fluence for the flame at ϕ=2.7 and HAB=20 mm. C: Resulting fluence curve by evaluation of the peak intensities of centre plot B.

Diagram A shows LII signals for two equivalence ratios of 2.3 and 2.7 at a HAB of 17 mm and a constant laser fluence of H=100 mJ·cm^{-2}. The inset shows the underlying

beam profile recorded with a beam profile camera. An increase of the signal intensity with increasing ϕ and therefore presumably higher soot concentrations can be observed [240, 258]. This quasi-proportional relationship is used to infer f_V from the prompt LII signal peak intensity. To guarantee homogenous particle heating in the measurement volume and reduced effects of inhomogeneous spatial laser profiles, f_V-experiments are typically performed at a sufficiently high laser fluence, leading to particle heating close to sublimation temperature of ~4000 K. Figure 2.13 B shows LII signals for a flame at ϕ=2.7 and a fluence variation from 60 - 160 mJ·cm^{-2}. As can be seen, the peak intensities converge towards a maximum value and plotting the maximum intensities over H leads to a typical fluence curve depicted on the right side of Figure 2.13. Therefore, LII can be classified into high fluence and low fluence regime measurements with a limit at ~100 mJ·cm^{-2} at 532 nm excitation (double for 1064 nm) [302, 303]. For quantitative f_V values a calibration procedure is required, commonly utilized by an extinction measurement at one specific point in the flame such as those described in section 2.2.3.4. For extended measurement volumes (e.g., 2D or 3D approaches), the location of the calibration measurement in the flame is important as variations in, e.g., the optical properties are otherwise not pictured. Other calibration procedures have been developed based on absolute incandescence intensities requiring measurements at two or multiple wavelengths [304, 305] similar to the description at the beginning of this section.

To resolve the primary particle size d_p from TiRe-LII data the temporal decay of the signal is analyzed. Due to the size specific surface-to-volume ratio of isolated spherical particles, smaller ones cool faster compared to larger particles. Here, for a quantitative evaluation the decay rates must be related to particle sizes, which can in principle derive from other sizing techniques such as TEM. Yet, as this would be extremely time-consuming and expensive and must be repeated for any change of the measurement conditions, the use of a regression between measured and modelled LII signals evolved as a standard for d_p determination. In this context, obviously a suitable heat and mass transfer model accounting for all heat transfer mechanisms is demanded, which was extensively developed over the last decades [280, 306]. Figure 2.14 shows a schematic illustration of some of the most important mechanisms together with modelled particle temperatures T_p and resulting normalized LII signals for four primary particle sizes. A detailed description of the utilized model with its mathematical formulations are given in manuscripts [M3] and [M4], while a brief overview about the basic principles is provided here.

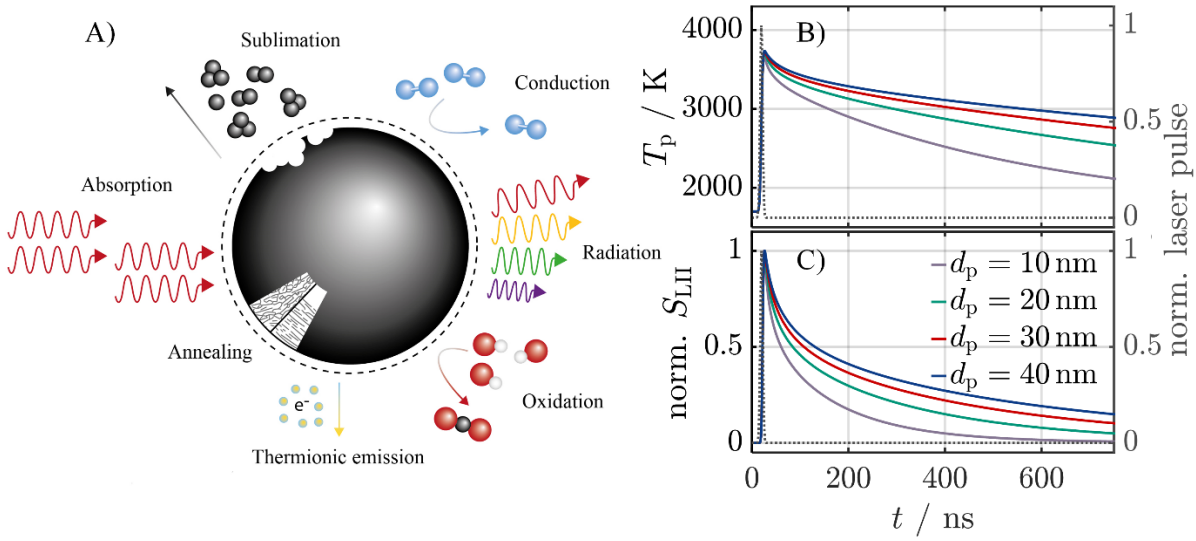

Figure 2.14: A: Schematic illustration of heat transfer mechanisms to model particle temperatures. B: Modelled particle temperature curves. C: Resulting normalized TiRe-LII signals for four exemplary particle sizes and measurement conditions summarized in Table 2.1.

First, the absorption of the laser pulse (grey dashed line in the diagrams B and C) leads to an increase of the internal energy and therefore heating of the particles. As the small particles absorb the laser volumetrically, they all reach approximately the same peak temperatures. After the laser pulse the particle temperature starts to decrease, which in the first nanoseconds might be dominated by sublimation (dependent on the utilized laser fluence) and is then overtaken mainly by heat conduction. Dependent on the primary particle sizes the temperature decay shows different slopes. The detected LII signal follows the cooling and is displayed in Figure 2.14 C. The modelled LII signals are calculated by solving the energy and mass balance equations based on input parameters summarized in Table 2.1.

Table 2.1: Input parameters to model T_p and S_{LII} of Figure 2.14.

Parameter	Value	Remark
Laser wavelength λ_{exc}	532 nm	Nd:YAG (frequency doubled)
Laser width (FWHM)	6 ns	-
Laser fluence H	80 mJ·cm^{-2}	-
Initial gas temperature T_g	1750 K	Mean value of a premixed flame
Density ρ	1860 kg·m^{-3}	[307]
Absorption function $E(\tilde{m})$	0.3	Average value in the visible [303]
Thermal accommodation coefficient α_T	0.2	Reduced value to account for shielding [308]
Specific heat c_s	2.3 J·g^{-1}·K^{-1}	T-dependent [309], value at 4000 K

Vapour pressure p_V	$1.89 \cdot 10^5$ Pa	T-dependent [310], value at 4000 K
Heat of vaporization Δh_V	$8.16 \cdot 10^5$ J·mol^{-1}	T-dependent [310], value at 4000 K
Mean molecular weight of vapour M_V	0.0397 kg·mol^{-1}	T-dependent [310], value at 4000 K
Heat-transfer mechanisms		$\dot{Q}_\mathrm{abs}$, $\dot{Q}_\mathrm{subl}$, $\dot{Q}_\mathrm{cond}$

The schematic illustration in Figure 2.14 A reveals that besides the heat transfer mechanisms reported in Table 2.1, additional ones such as radiation, oxidation, thermionic emissions or annealing occur [311, 312]. However, these terms typically have a small share in the energy and mass balance and are therefore often neglected. This is further justified by an increasing model complexity possibly leading to higher uncertainties of the inferred particle sizes as the knowledge on certain parameters relevant to model these mechanisms is vague. To give an example, the models for thermionic emissions – the release of electrons from the hot soot particle – are often based on a work function value of graphite leading to an overestimation of the effect [313]. Similar limitations hold for the formulation of sublimation models [314], which for example in most cases neglect effects such as recondensation [315]. That is why particle sizing with TiRe-LII is preferably applied at low fluence levels where sublimation becomes negligible. A major challenge is the fine structural change of soot particles with maturity and its impact on particle heating and sublimation [316], especially as there is a strong correlation between particle growth and particle maturity. The absorption and emission characteristics of the soot particles strongly depend on their optical properties and can be addressed in the value of $E(\widetilde{m}, \lambda)$, which shows a large variation reported in literature [302, 303, 317]. Recently, multiple studies are dedicated to the question of $E(\widetilde{m}, \lambda)$ changes and dependencies, including a size dependency [273] or effects as internal multiple scattering in soot aggregates leading to the introduction of a light absorption enhancement factor [318]. Besides the techniques discussed in section 2.2.3.4, LII provides an additional possibility to infer $E(\widetilde{m}, \lambda)$ [319], e.g., by being applied in a dual-pulse manner [266]. Further, the reduction of possible heat transfer mechanisms by, e.g., utilizing LII measurements at low fluence (no sublimation) in the vacuum (no heat conduction) facilitates to determine this quantity following [320]

$$E(\widetilde{m}) \approx \frac{h^4 \cdot c^3}{1194 \cdot \pi^2 \cdot k_\mathrm{B}^5} \cdot \frac{\rho(T) \cdot c_\mathrm{s}(T)}{T^5} \frac{\mathrm{d}T}{\mathrm{d}t}. \tag{9}$$

This is of particular interest with respect to recent findings related to specific heat and density [132], which possibly allows for a re-evaluation of these measurements. Another parameter that shows a wide range in reported values is the thermal accommodation coefficient α_T. It is a relative quantity describing the efficiency of a particle and gas molecule collision resulting in a value of 1.0 for complete energy transfer and a value of zero for no energy transfer [321]. Here, an important aspect derives from the fact that the LII signal does not result from isolated spherical particles but from aggregates composed of polydispersly distributed primary particles. Typically, a physical value of about 0.37 is considered for soot primary particles [308, 322], while the dendritic structure of aggregates reduces the collision efficiency and therefore can be considered by a reduced α_T value. Here, the reader is additionally referred to manuscript [M3] highlighting the role of aggregate morphology to particle sizing by TiRe-LII. A remaining question is how reliable primary particle size distributions can be inferred from LII signals if no further knowledge about the aggregate structure is given. The main challenge to determine the correct value of α_T results from the fact that it is hard to measure for soot and in many cases derives from molecular dynamics (MD) simulations [323]. The latter is complicated as there are multiple forms of structural arrangement for different soot maturities and therefore the value for α_T is considered to change throughout the soot evolution process.

The discussion about the “correct” choice of heat and mass transfer models as well as utilized values of uncertain parameters leads to the question of the limitations of the technique. Regarding the lower limit, Desgroux and coworkers reported f_V values of 0.12 ppt in nucleation flames [89] and particle sizes of ~3 nm for incipient soot [145]. However, this was possible under very controlled conditions. The simultaneous presence of larger soot aggregates as existent in many applications such as large scale furnaces [324] shifts these limits. In such environments often the assumption of an optically thin medium is violated and therefore effects such as soot self-absorption (SSA) become increasingly important [277, 325, 326].

3 Aim of the Thesis

The previous sections highlighted the complexity and challenges related to the soot evolution process. While many aspects are already investigated, especially the early phases of the process require an improved understanding. Same holds for the complete characterisation of soot particles during their growth and oxidation in flames. Major parts of the current knowledge derive from appropriate diagnostics. However, as the process is not entirely understood additional effort in the development of these techniques is demanded. While *ex situ* approaches mainly suffer from disturbance of the underlying process, optical *in situ* diagnostics in many cases offer fast and spatially resolved results of targeted QoI necessary to follow and picture the evolution process. In this work the main focus lies on the use of broadband absorption spectroscopy and laser-induced incandescence. In detail, the manuscripts forming the main body of this thesis are dedicated to several research questions related to soot formation, which can be summarized in shortened form as:

- Is it possible to identify PAHs as soot precursors in flames based on their absorption characteristics in the UV-Vis wavelength range?

The measurement concept developed can also be used for later process phases. Here, also the spectral absorption of soot particles changes throughout the soot evolution process leading to the following question:

- Is a direct or indirect transition assumption the better descriptor for the optical band gap of soot particles, which is a quantity related to soot maturity?

The strong correlation between soot maturity in form of the structural arrangement of the particles and their growth process requires a technique capable of providing reliable size measurements. Here a pending question remained:

- Is it possible to infer not only an effective, average particle size but particle size distribution parameters from TiRe-LII signals, and what knowledge is required about the degree of aggregation and other model parameters?

With fundamental findings on the capabilities of the technique, a follow up question remains in using TiRe-LII for extended measurement volumes:

- Can particle sizing through TiRe-LII be used as a volumetric technique providing 3D information and what is the impact of parameters such as the initial flame temperature and the utilized laser fluence?

Only new developments as presented in the next section of this thesis allow for major steps in answering these questions. Beyond these specific research questions, this work is additionally dedicated to provide an overview about current state of the art.

4 Main Approaches and Selected Results

This chapter gives an overview of the four publications in peer-reviewed journals that form the core of the thesis. It describes the main concepts of the experimental approaches, which are detailed in the respective manuscripts. In particular, it is also to provide common routes in the experimental, which bridge from one manuscript to another. A detailed presentation and discussion of the manifold results is also given in the respective manuscripts, a repetition does not seem appropriate here. So in this chapter only the respective major findings are summarized. In the case of [M4] supporting results are presented in brief that complement the investigations presented there. Instead of a chronological order of the publication dates, the reader is advised to comply to the upcoming sequence as it follows the soot evolution process.

4.1 UV-Vis Absorption Spectroscopy for PAH and Soot Characterisation

To perform UV-Vis absorption spectroscopy measurements in flames a broadband light source is required. In this work a laser driven light source (LDLS) was used, which is based on the emission of a plasma powered by a 974 nm CW laser. In comparison to other UV-Vis light sources such as deuterium lamps the LDLS benefits from a ~100 times high spectral radiance as well as a broad spectral range from 190 nm to 2100 nm. The experimental setup used for the flame measurements is depicted in Figure 4.1.

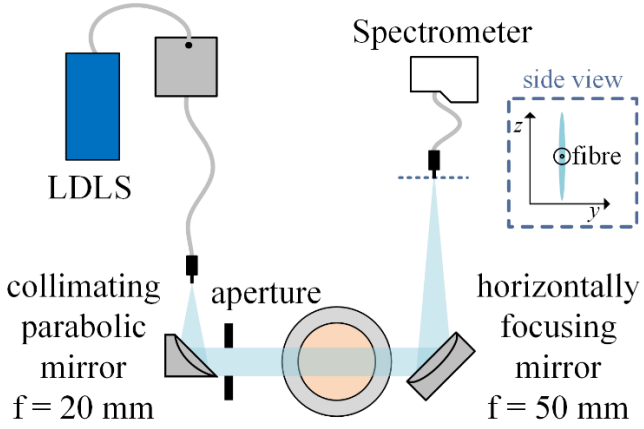

Figure 4.1: Experimental setup as utilized in [M1] for UV-Vis absorption spectroscopy measurements in flames. The light of a LDLS is collimated by an off-axis parabolic mirror, shone through the flame and focused into a detection fibre coupled to a spectrometer (resolving a wavelength range from 200 nm to 540 nm). The signal is spatially filtered by the fibre and results from one horizontal plane at a defined HAB position.

The output fibre of the LDLS is 230 µm in diameter with a numerical aperture of 0.22. For collimation of the broadband light an off-axis parabolic UV-enhanced aluminium

mirror with a focal length of 20 mm was utilized. The flame under investigation is run with a premixed C_2H_4/air gas mixture at varying equivalence ratios. For each measurement position I_0 and I were acquired and the respective background signal was subtracted from the measurements. The absorption coefficient was then obtained following Equation (4). The measured UV-Vis spectra were reconstructed in a next step based on a database of the individual absorbing species. Here, the individual spectra were first convoluted by a simplified energetic model to account for the high temperature flame conditions. After reconstruction of the measured spectra the resulting species distributions for two HAB positions and five equivalence ratios are shown in the bar charts of Figure 4.2 taken from [M1].

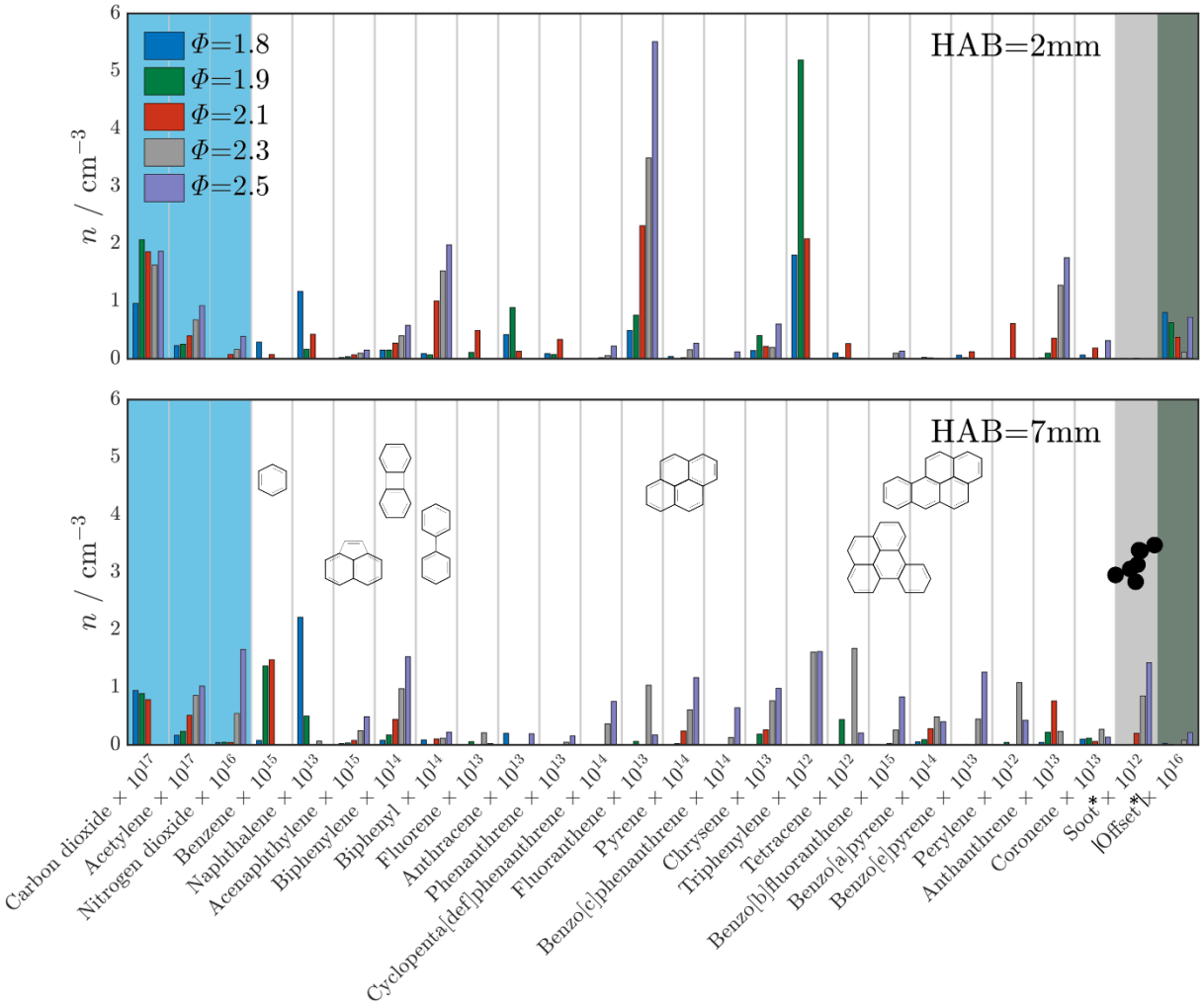

Figure 4.2: Resulting species distributions for two HAB positions and five equivalence ratios taken from [M1]. The species size increases from left to right.

The diagrams reveal that the number density of many PAHs increase with increasing ϕ and especially larger PAHs and soot particles exist at the 7 mm HAB position. A case study of two soot absorption spectra in the database revealed little impact to the inferred PAH distribution, making the approach in principle attractive to other flame

investigations. Overall, the approach sheds light on the early stages of soot formation and investigates the role of PAHs as soot precursor molecules.

4.2 Absorption Spectroscopy to Investigate the Optical Band Gap of Soot

Following the soot formation process, after the PAH zone especially the particle inception and growth regions are of paramount interest. At these stages the first solid incipient particles, which are highly amorphous transform with increasing maturity to more graphitic-like particles. This fine structural change manifests in form of a decreasing value of the optical band gap, which is therefore an important parameter to quantify the level of soot maturity. Its determination is possible by using the so-called Tauc method applied to absorption spectra. The method is based on the extrapolation of a linear function to the converted absorption data. The value of E_g can then be taken from the intersection point of the linear fit and the abscissa. To acquire the absorption spectra, basically the same experimental setup as shown in Figure 4.1 was used. The premixed burner was replaced by a standard non-premixed flame similar to the one shown in Figure 2.2 C and the spectrometer for detection was replaced by one that covers a broader spectral range up to 1000 nm. One debated aspect lies in the transition type of soot. Prior to the evaluation with the Tauc method the transition type value must be defined and takes a value of 2 for an indirect allowed and 0.5 for a direct allowed transition. This is illustrated in Figure 4.3, which shows the comparison of the resulting band gaps for the different transition type assumptions for the same absorption measurements at HAB=40 mm.

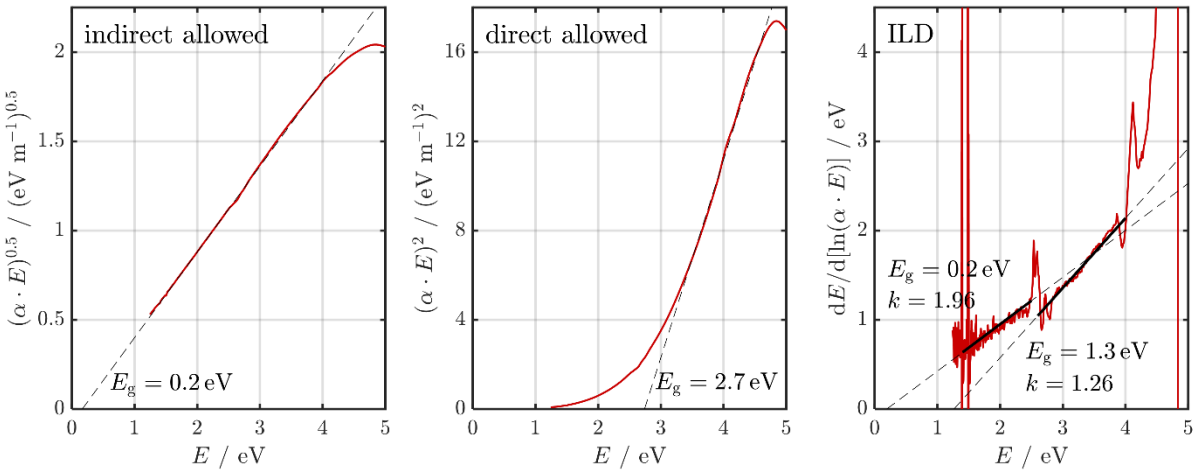

Figure 4.3: Tauc plots for the indirect and direct allowed transition and the inverse logarithmic derivative (ILD) method used in [M2]. The underlying absorption data are the same for each plot taken at HAB=40 mm in a non-premixed C_2H_4 flame.

As can be seen, the resulting band gap values differ if either an indirect or a direct allowed transition is used. This led to the question which assumption is the better choice for soot particles. To that end, an inverse logarithmic derivative method was adopted to simultaneously infer the optical band gap value as well as the transition type exponent. The results revealed that for mature soot an indirect allowed transition exists with a band gap value close to 0.2 eV. However, a second slope can be observed at higher energy ranges indicating towards a changed transition type and resulting in higher band gap values. This can possibly be attributed to the coexistence of multiple species in the measurement volume. To answer this question spatially resolved measurements of the band gaps are required. This can be realized by coupling the technique with tomographic reconstruction.

4.3 Laser-Induced Incandescence to Infer Primary Particle Size Distributions

It is still unclear whether the optical properties of soot are dominated by the degree of maturity or the particle size. This is especially challenging as both parameters are strongly correlated during the growth process. Therefore, besides the characterisation of soot maturity in form of the optical band gap also an *in situ* sizing technique is required for a comprehensive understanding of the process. Here, TiRe-LII is an ideal tool for the determination of the primary particle size. While the technique is long established the reliability of determining the primary particle size distribution parameters (assuming a log-normal distribution) remained unanswered. Manuscript [M3] is dedicated to the question if reliable primary particle size distribution parameters μ_{d_p} and σ_{d_p} can be inferred from a TiRe-LII signal and how much knowledge about the aggregate structure and certain model parameters is required.

A typical TiRe-LII experimental setup is depicted in Figure 4.4 and was used to record LII signals as depicted in Figure 2.13. The intensity of a laser pulse is controlled using the combination of a half-wave plate and a polarizing beam cube. Several optical components shape the laser beam, which is shone through the flame. The resulting incandescence signal is collected by several optics and recorded by a PMT (equipped with filters) and an oscilloscope.

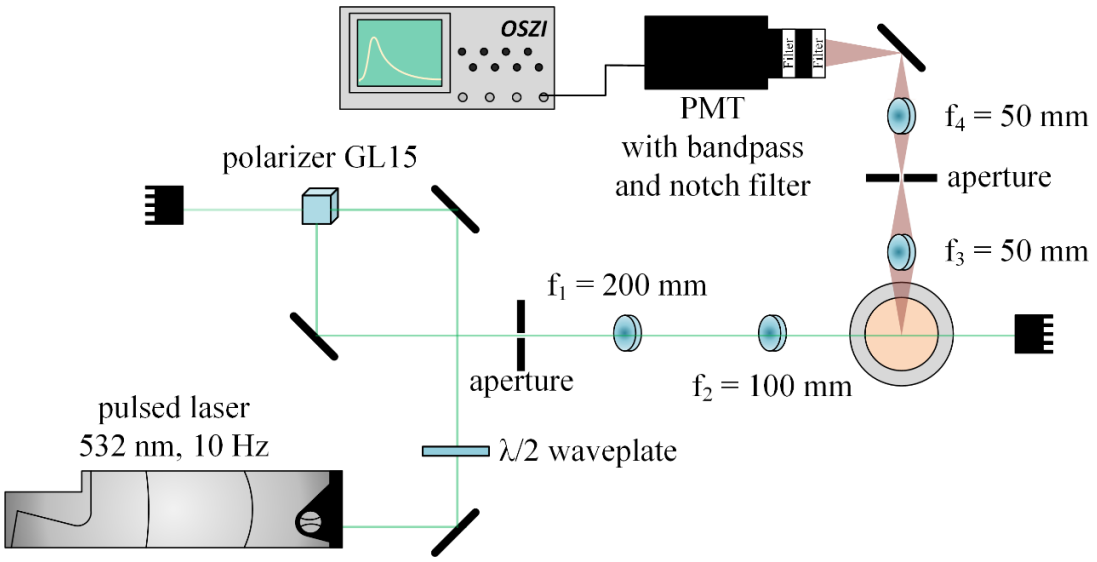

Figure 4.4: Experimental setup to acquire TiRe-LII data for the determination of d_p. The laser pulse intensity is regulated and shaped by several optical components to ultimately heat the soot particles in the premixed flame. The resulting incandescence signal is recorded under 90° with an PMT detection setup monitored by an oscilloscope.

The determination of primary particle sizes using a regression between measurements and the LII model is an ill-posed problem, meaning that multiple sets of parameters explain the measured signal equally well. One source contributing to the uncertainties in the inferred QoI (μ_{d_p} and σ_{d_p}) is the measurement noise. The acquisition of a sufficient number of signals makes it possible to investigate the noise behaviour as laid out in detail in [M3]. Additionally, uncertainties in model parameters propagate to the uncertainties of the QoI. Here, Bayesian inference is used to incorporate prior knowledge about certain parameters including the size of the aggregates. To investigate the impact of shielding on the determination of the size distribution parameters, knowledge about the aggregate structure is required. To that end WALS can be used to obtain the radius of gyration R_g and the fractal dimension D_f. A regression between the measured scattering curves shown in Figure 2.9 B and modelled ones based on Equation (3) results in aggregate sizes and fractal dimensions as listed in Table 4.1.

Table 4.1: Resulting quantities of ELS measurements at three HAB positions in a C_2H_2/air premixed flame at ϕ=2.7. A prior of D_f=1.78±0.01 was used during Bayesian evaluation similar to the approach described in detail in manuscript [M3].

HAB / mm	$R_{g,eff}$ / nm	D_f
12	95	1.74
17	136	1.66
21	160	1.64

As can be seen, the effective radius of gyration $R_{\mathrm{g,eff}}$ increases at higher HAB positions due to aggregate growth, while the fractal dimension tends to decrease indicating the formation of more linearly-shaped structures. This information about the state of aggregation can now be used as an input parameter in the LII model. Different scenarios reflecting different levels of knowledge were analysed with respect to the resulting uncertainties of μ_{d_p} and σ_{d_p}. These are shown in Figure 4.5 for flame-case conditions.

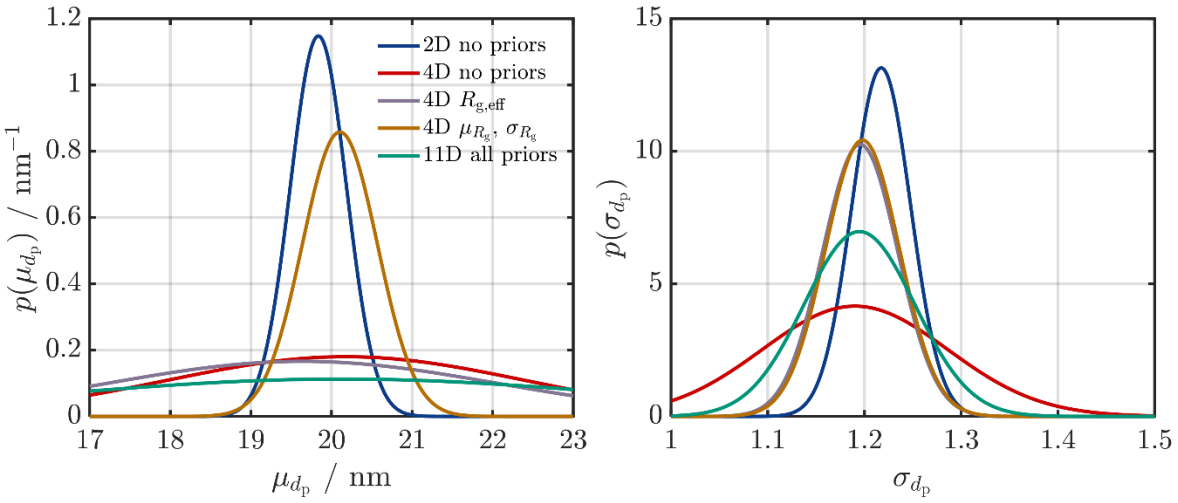

Figure 4.5: Resulting uncertainties of μ_{d_p} and σ_{d_p} for various scenarios under flame conditions taken from [M3].

The best-case scenario is depicted in blue assuming that all parameters other than μ_{d_p} and σ_{d_p} are known. However, for flame measurements this is rarely the case and by adding the aggregate size distribution parameters as unknowns (shown in red) the uncertainties increase. If knowledge about the aggregate size in form of $R_{\mathrm{g,eff}}$ deriving, e.g., from WALS measurements or the aggregate size distribution parameters is present, the uncertainties in μ_{d_p} and σ_{d_p} decrease again (purple and orange lines). A last scenario reveals the impact of multiple uncertain parameters (as also discussed in Section 2.2.3.5) and is depicted in green. These findings allow to evaluate under which conditions reliable estimates about μ_{d_p} and σ_{d_p} can be obtained.

4.4 Volumetric Laser-Induced Incandescence for Particle Sizing

While the reliable determination of size distribution parameters requires knowledge of various parameter, the determination of relative changes in particle size throughout a flame is of great importance. This especially holds for extended measurement volumes,

which in best case are three-dimensional to capture the full picture of soot formation in a flame. Manuscript [M4] is dedicated to the possibility of using TiRe-LII for particle sizing as a volumetric technique. Therefore, it is coupled with tomographic reconstruction based on simultaneous recordings of flame images from various detection angles. While the manuscript [M4] provides a proof-of-concept in a smaller non-standard flame, a remaining question was the validation of the method against planar and pointwise measurements. Therefore, additional measurements were taken in the standard non-premixed coflow ethylene/air diffusion flame depicted in the centre of Figure 2.2 and well characterized by various research groups [303]. In principle the experimental setup follows the description of [M4], while the overall detection angle was slightly increased to ~150° and a higher mean laser fluence of H=183 mJ·cm^{-2} was realized. The schematics are depicted in Figure 4.6 with the beam profile of the laser shown in the inset.

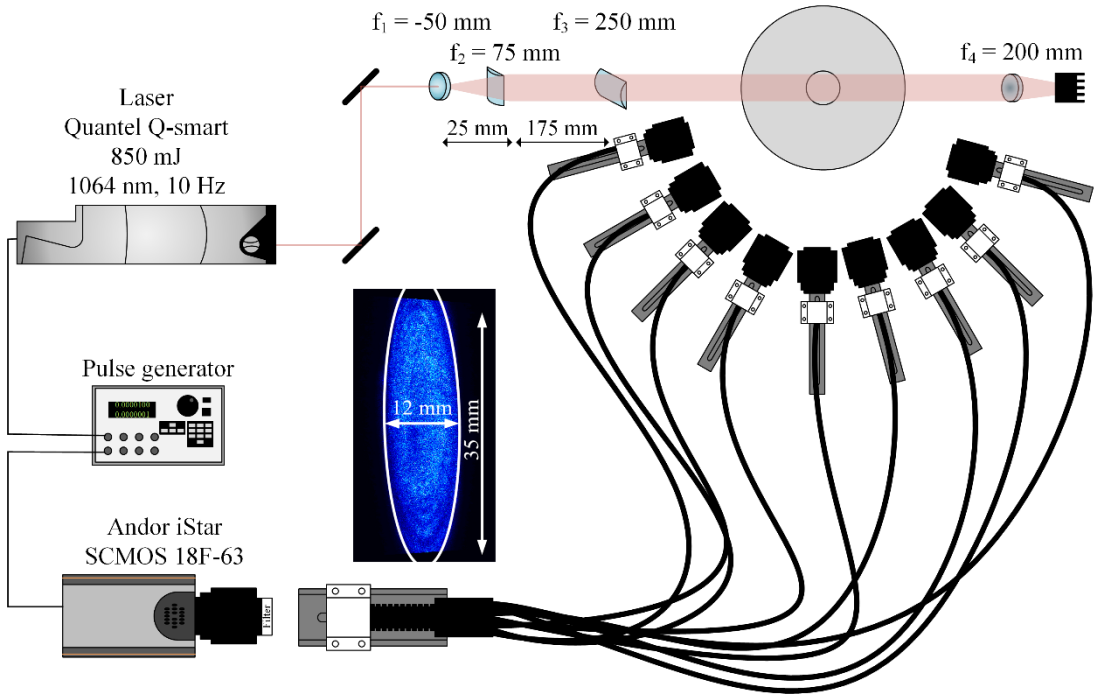

Figure 4.6: Schematic illustration of the optical setup for 3D TiRe-LII.

Regarding data evaluation, instead of the algebraic reconstruction technique (ART) a multiplicative algebraic reconstruction technique (MART) implemented in LaVision's commercial DaVis software together with the therein suggested camera calibration procedure was used. For details on the various forms of reconstruction algorithms the reader is referred to a review paper by Grauer et al. [327]. Figure 4.7 shows a resulting reconstructed LII signal as well as f_V and d_p maps for the centre layer together with radial distributions for four HAB positions. The f_V values derive from the prompt LII

signal and a calibration using the extinction measurements in the same flame displayed in Figure 2.11. The d_p results derive from the regression of sequentially acquired decay curves and the model accounting for various input parameters as described above or in manuscript [M4]; including pyrometry measurements at 425 nm and 750 nm centre wavelength detection.

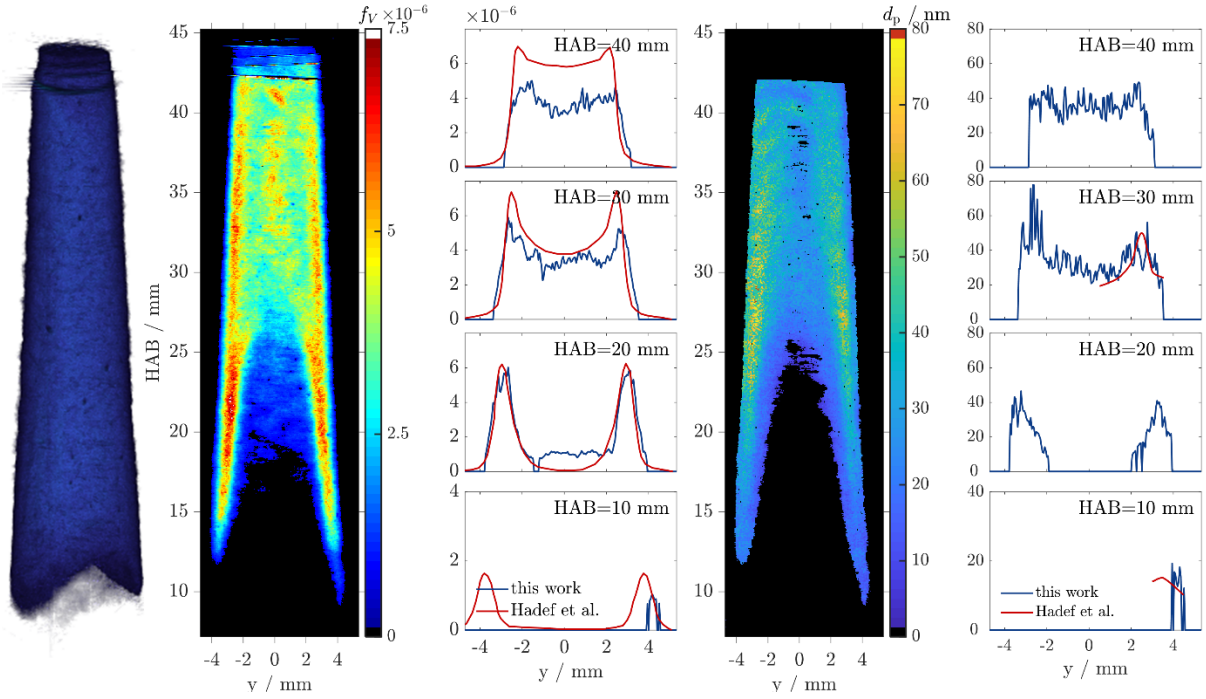

Figure 4.7: From Left to Right: 3D LII signal after tomographic reconstruction of a non-premixed coflow ethylene/air flame. Centre layer of 3D data for f_V values with radial distributions at four HAB positions in comparison with data by Hadef et al. [328]. Analogous for d_p results.

As can be seen, a comparison to the planar data of Hadef et al. [328] for the same flame configuration shows overall good agreement with a slight underestimation for f_V at HAB=40 mm. Obviously, the 3D results are more strongly affected by noise, however, provide a remarkably higher information density regarding the total measurement volume compared to 2D results. A comparison at a well characterized measurement location at HAB=42 mm burner centreline reveals values of f_V=3.5 ppm, d_p=34.5 nm and T_g=1660 K, which are in good agreement with reported values in reference [303]. A qualitative comparison regarding f_V and d_p maps to a slightly different non-premixed ethylene/air flame again reveals overall consistency [329, 330]. Therefore, the technique applied in a volumetric manner is considered to be capable of providing reliable results regarding the various QoI. Further possible improvements may be achieved by investigating the spectral and intensity dependent response of the detection equipment. Intensified cameras are known to exhibit some slight non-linear behaviour along the pixel array, which at this point is considered negligible.

5 Conclusions and Prospect

This thesis explored optical diagnostics to investigate the soot evolution process in hydrocarbon flames and provided an insight to several decisive quantities related to different stages of the process. The focus lied on the *in situ* assignment of combustion species and intermediates such as soot precursors in flames as well as the determination of soot particle sizes related to growth and oxidation reactions. The main section is composed of four publications, which are given in the appendix.

Precisely, several examples were named where the soot formation process plays and will play an important role, and therefore an understanding of its detailed steps is demanded. This was followed by an overview of the current understanding of the soot evolution process and a list of commonly used *ex situ* and *in situ* diagnostics. The limits, advantages and disadvantages of the respective techniques were highlighted and the importance of combining various techniques was underlined. Special attention was paid to two techniques, namely broadband absorption spectroscopy and time-resolved laser-induced incandescence.

The first was used to investigate the absorption characteristics of PAH molecules in the UV-Vis region, as they are considered as the building blocks of soot particles. The assignment to defined PAHs is complicated by the broadening of absorption bands at elevated flame temperature and the various species involved. One aspect was the simultaneous existence of soot particles as strong broadband absorbers for *in situ* measurements. The compilation of a database and a simplified energetic model was used to reconstruct measured absorption spectra and provided indications of certain PAH distributions for the first time. The development of this *in situ* measurement tool therefore allows to investigate the early steps of soot formation. For future improvements, some challenges related to the technique need to be addressed. In most cases the absorption path length strongly impacts the signal quality and a multi pass setup is mostly accompanied by reduced spatial information. Dedicated flames with stretched out formation regions and long absorption path length could facilitate investigations. Additionally, it must be kept in mind that due to temperature broadening the absorption signals show limited spectral features that help to identify certain molecules. Here, a coupling with additional techniques such as LIF can potentially improve the results by increasing the information density through a comparative technique.

Broadband absorption measurements were additionally utilized to shed light on the optical band gap of soot particles in flames. The optical band gap is an important

quantity for the use of carbon blacks in various applications such as solar cells. The semiconducting behaviour of the particles mainly derives from their fine structural arrangement, which changes throughout the formation process from amorphous to graphitic-like. In this case, a method was applied that allowed to retrieve the optical band gap value as well as the type of transition, which can be of a direct or indirect nature. Additional *ex situ* Raman measurements complemented the picture at the respective measurement locations. The results suggest that in most cases an indirect band gap assumption is the better choice for soot particles. However, the transition type presumably shows a dependency on soot maturity. The main drawback derived from the LOS integrated measurements and that the signal results from multiple species along the measurement path. This can be overcome by investigating a flame with stretched formation regions, e.g., using a low-pressure burner. A second option is the combination of the measurements and tomographic approaches to receive a 2D map of soot band gaps in a measurement plane, which is currently in progress.

The determination of soot particle sizes is based on a regression between TiRe-LII measurements and a heat and mass transfer model. This method depends on multiple model parameters as well as measurement noise of the LII signals. Both aspects make this problem ill-posed, meaning that various sets of parameters explain the measured decay rate equally well. To assess influences of the uncertainty of model parameters and measurement noise, a Bayesian method was utilized to investigate the possibility to obtain primary particle size distribution parameters with respect to the dendritic structure of soot aggregates and its influence on heat conduction. The results suggest that a certain degree of knowledge of the aggregate morphology is required to receive reliable estimates, especially for TiRe-LII experiments conducted at ambient conditions. With the help of these findings, assessments can now be made under which measurement conditions reliable primary particle size distributions can be obtained.

Finally, TiRe-LII was applied as a volumetric technique for particle sizing with emphasize on required input parameters such as initial flame temperature and local laser fluence. A comparison to planar and pointwise techniques was provided in present work to verify the approach in a standard flame. As a next step, the technique can be advanced to a high-speed diagnostic. A high repetition rate pulse laser in combination with three high-speed cameras allows for temporally resolved measurements at short time scales. Two of the cameras detect the LII signal decay at two time instances, while the third one is used in combination with one of the others for temperature determination via two colour pyrometry. This approach could be used in turbulent flames to follow and track changes of soot particle sizes. As under these conditions soot formation proceeds in all

spatial dimensions and at short time scales a tomographic high-speed technique is required. Additional focus should be on improvements regarding tomographic reconstruction as well as experimental related aspects. For the latter, e.g., spatially homogenous volumetric illumination can be improved with the use of adaptive optics such as deformable mirrors.

While the above-mentioned research findings are dedicated to detailed sub-questions of the soot evolution process, they contribute to improve its overall understanding. Optical diagnostics as an often cheap and *in situ* capable option resolve these nanoscale processes and are therefore increasingly important in the foreseeable future. Ultimately, this is required to use the unique characteristics of soot nanoparticles in various technical applications and also develop cleaner combustion technologies.

6 References

[1] A. Dreizler, H. Pitsch, V. Scherer, C. Schulz, J. Janicka
The role of combustion science and technology in low and zero impact energy transformation processes
Applications in Energy and Combustion Science **7** (2021), 100040.

[2] H. Pfeifer
Industrial furnaces-status and research challenges
Energy Procedia **120** (2017), 28-40.

[3] S. Solomon, G.-K. Plattner, R. Knutti, P. Friedlingstein
Irreversible climate change due to carbon dioxide emissions
Proceedings of the National Academy of Sciences **106** (2009), 1704-1709.

[4] P. Glarborg, J. A. Miller, B. Ruscic, S. J. Klippenstein
Modeling nitrogen chemistry in combustion
Progress in Energy and Combustion Science **67** (2018), 31-68.

[5] H. Bockhorn
Soot formation in combustion: mechanisms and models
Springer Science & Business Media, Berlin, Heidelberg (2013).

[6] K. H. Homann
Fullerenes and soot formation—new pathways to large particles in flames
Angewandte Chemie International Edition **37** (1998), 2434-2451.

[7] H. Richter, J. B. Howard
Formation of polycyclic aromatic hydrocarbons and their growth to soot—a review of chemical reaction pathways
Progress in Energy and Combustion Science **26** (2000), 565-608.

[8] T. C. Bond, R. W. Bergstrom
Light absorption by carbonaceous particles: An investigative review
Aerosol Science and Technology **40** (2006), 27-67.

[9] T. C. Bond, S. J. Doherty, D. W. Fahey, P. M. Forster, T. Berntsen, B. J. DeAngelo, M. G. Flanner, S. Ghan, B. Kärcher, D. Koch
Bounding the role of black carbon in the climate system: A scientific assessment
Journal of Geophysical Research: Atmospheres **118** (2013), 5380-5552.

[10] L. Poulain, B. Fahlbusch, G. Spindler, K. Müller, D. van Pinxteren, Z. Wu, Y. Iinuma, W. Birmili, A. Wiedensohler, H. Herrmann
Source apportionment and impact of long-range transport on carbonaceous aerosol particles in central Germany during HCCT-2010
Atmospheric Chemistry and Physics **21** (2021), 3667-3684.

[11] G. De Falco, C. Colarusso, M. Terlizzi, A. Popolo, M. Pecoraro, M. Commodo, P. Minutolo, M. Sirignano, A. D'Anna, R. P. Aquino
Chronic obstructive pulmonary disease-derived circulating cells release IL-18 and IL-33 under ultrafine particulate matter exposure in a caspase-1/8-independent manner
Frontiers in Immunology **8** (2017), 1415.

[12] C. Colarusso, G. De Falco, M. Terlizzi, F. Roviezzo, I. Cerqua, M. Sirignano, G. Cirino, R. P. Aquino, A. Pinto, A. D'Anna
The Inhibition of Caspase-1-Does Not Revert Particulate Matter (PM)-Induced Lung Immunesuppression in Mice
Frontiers in Immunology **10** (2019), 1329.

[13] D. M. Broday, R. Rosenzweig
Deposition of fractal-like soot aggregates in the human respiratory tract
Journal of Aerosol Science **42** (2011), 372-386.

[14] P. Pedata, T. Stoeger, R. Zimmermann, A. Peters, G. Oberdörster, A. D'Anna
Are we forgetting the smallest, sub 10 nm combustion generated particles?
Particle and Fibre Toxicology **12** (2015), 1-4.

[15] I. M. Kennedy
The health effects of combustion-generated aerosols
Proceedings of the Combustion Institute **31** (2007), 2757-2770.

[16] H. I. Abdel-Shafy, M. S. Mansour
A review on polycyclic aromatic hydrocarbons: source, environmental impact, effect on human health and remediation
Egyptian Journal of Petroleum **25** (2016), 107-123.

[17] K.-H. Kim, S. A. Jahan, E. Kabir, R. J. Brown
A review of airborne polycyclic aromatic hydrocarbons (PAHs) and their human health effects
Environment International **60** (2013), 71-80.

[18] European Environment Agency
Air quality in Europe: 2020 report
Publications Office of the European Union, Luxembourg (2020).

[19] World Health Organization
WHO global air quality guidelines: particulate matter (PM2. 5 and PM10), ozone, nitrogen dioxide, sulfur dioxide and carbon monoxide
World Health Organization, Geneva (2021).

[20] J. L. Laughner, J. L. Neu, D. Schimel, P. O. Wennberg, K. Barsanti, K. W. Bowman, A. Chatterjee, B. E. Croes, H. L. Fitzmaurice, D. K. Henze
Societal shifts due to COVID-19 reveal large-scale complexities and feedbacks between atmospheric chemistry and climate change
Proceedings of the National Academy of Sciences **118** (2021), e2109481118.

[21] Z. S. Venter, K. Aunan, S. Chowdhury, J. Lelieveld
COVID-19 lockdowns cause global air pollution declines
Proceedings of the National Academy of Sciences **117** (2020), 18984-18990.

[22] S. Nalley, A. LaRose
Annual Energy Outlook 2021
https://www.eia.gov/pressroom/presentations/AEO2021_Release_Presentation.pdf
(2021), accessed 12 August 2021.

[23] G. Kalghatgi
Is it really the end of internal combustion engines and petroleum in transport?
Applied Energy **225** (2018), 965-974.

[24] G. Kalghatgi
Development of fuel/engine systems—the way forward to sustainable transport
Engineering **5** (2019), 510-518.

[25] F. Leach, G. Kalghatgi, R. Stone, P. Miles
The scope for improving the efficiency and environmental impact of internal combustion engines
Transportation Engineering **1** (2020), 100005.

[26] J. C. Corbin, H. Czech, D. Massabò, F. B. de Mongeot, G. Jakobi, F. Liu, P. Lobo, C. Mennucci, A. A. Mensah, J. Orasche
Infrared-absorbing carbonaceous tar can dominate light absorption by marine-engine exhaust
NPJ Climate and Atmospheric Science **2** (2019), 1-10.

[27] F. Hagen, F. Hardock, S. Koch, N. Sebbar, H. Bockhorn, A. Loukou, H. Kubach, R. Suntz, D. Trimis, T. Koch
Why Soot is not Alike Soot: A Molecular/Nanostructural Approach to Low Temperature Soot Oxidation
Flow, Turbulence and Combustion **106** (2021), 295-329.

[28] F. P. Hagen, D. Kretzler, T. Häber, H. Bockhorn, R. Suntz, D. Trimis
Carbon nanostructure and reactivity of soot particles from non-intrusive methods based on UV-VIS spectroscopy and time-resolved laser-induced incandescence
Carbon **182** (2021), 634-654.

[29] R. L. Vander Wal, A. J. Tomasek
Soot oxidation: dependence upon initial nanostructure
Combustion and Flame **134** (2003), 1-9.

[30] Y. Wang, M. Gu, Y. Zhu, L. Cao, B. Zhu, J. Wu, Y. Lin, X. Huang
A review of the effects of hydrogen, carbon dioxide, and water vapor addition on soot formation in hydrocarbon flames
International Journal of Hydrogen Energy **46** (2021).

[31] O. I. Awad, X. Ma, M. Kamil, O. M. Ali, Y. Ma, S. Shuai
Overview of polyoxymethylene dimethyl ether additive as an eco-friendly fuel for an internal combustion engine: Current application and environmental impacts
Science of the Total Environment **715** (2020), 136849.

[32] N. Palazzo, L. Zigan, F. J. T. Huber, S. Will
Impact of Oxygenated Additives on Soot Properties during Diesel Combustion
Energies **14** (2021), 147.

[33] M. Mannazhi, S. Bergqvist, P.-E. Bengtsson
Influence of potassium chloride on PAH concentration during soot formation studied using laser-induced fluorescence
Combustion and Flame **235** (2022), 111709.

[34] M. Mannazhi, S. Bergqvist, P.-E. Bengtsson
Laser-induced fluorescence for studying the influence of potassium and sodium salts on PAH formation in sooting premixed flames
Applied Physics B **128** (2022), 1-8.

[35] S. Eckart, L. Cai, C. Fritsche, F. vom Lehn, H. Pitsch, H. Krause
Laminar burning velocities, CO, and NOx emissions of premixed polyoxymethylene dimethyl ether flames
Fuel **293** (2021), 120321.

[36] R. Banerjee, S. Roy, P. K. Bose
Hydrogen-EGR synergy as a promising pathway to meet the PM–NOx–BSFC trade-off contingencies of the diesel engine: a comprehensive review
International Journal of Hydrogen Energy **40** (2015), 12824-12847.

[37] A. S. Alamoush, A. I. Ölçer, F. Ballini
Ports' role in shipping decarbonisation: A common port incentive scheme for shipping greenhouse gas emissions reduction
Cleaner Logistics and Supply Chain **3** (2021), 100021.

[38] J.-B. Donnet
Carbon black: science and technology
CRC Press, New York (1993).

[39] O. Kutsch
Ceresana Brochure - Market Study: Carbon Black (3rd ed.)
https://www.ceresana.com/upload/Marktstudien/brochueren/Ceresana_Brochure_Market-Study_Carbon-Black_3.pdf (2018), accessed 30 August 2021.

[40] J. Fröhlich, W. Niedermeier, H.-D. Luginsland
The effect of filler–filler and filler–elastomer interaction on rubber reinforcement
Composites Part A: Applied Science and Manufacturing **36** (2005), 449-460.

[41] G. Pfaff
Carbon black pigments
Physical Sciences Reviews **7** (2021), 109-125.

[42] G. Pfaff
5. Black pigments (carbon black)
Inorganic Pigments, (Hrsg.), De Gruyter, (2017),167-189.

[43] S. Khodabakhshi, P. F. Fulvio, E. Andreoli
Carbon black reborn: Structure and chemistry for renewable energy harnessing
Carbon **162** (2020), 604-649.

[44] M. R. Mulay, A. Chauhan, S. Patel, V. Balakrishnan, A. Halder, R. Vaish
Candle soot: Journey from a pollutant to a functional material
Carbon **144** (2019), 684-712.

[45] A. G. Pandolfo, A. F. Hollenkamp
Carbon properties and their role in supercapacitors
Journal of Power Sources **157** (2006), 11-27.

[46] M. E. Spahr, D. Goers, A. Leone, S. Stallone, E. Grivei
Development of carbon conductive additives for advanced lithium ion batteries
Journal of Power Sources **196** (2011), 3404-3413.

[47] R. Kumar, T. Bhuvana, A. Sharma
Tire waste derived turbostratic carbon as an electrode for a vanadium redox flow battery
ACS Sustainable Chemistry & Engineering **6** (2018), 8238-8246.

[48] H. H. Nersisyan, J. H. Lee, J.-R. Ding, K.-S. Kim, K. V. Manukyan, A. S. Mukasyan
Combustion synthesis of zero-, one-, two-and three-dimensional nanostructures: Current trends and future perspectives
Progress in Energy and Combustion Science **63** (2017), 79-118.

[49] F. Lockwood, J. Van Niekerk
Parametric study of a carbon black oil furnace
Combustion and Flame **103** (1995), 76-90.

[50] T. Henning, F. Salama
Carbon in the Universe
Science **282** (1998), 2204-2210.

[51] J. Lee, D. Tikhonov, P. Chopra, S. Maclot, A. Steber, S. Gruet, F. Allum, R. Boll, X. Cheng, S. Düsterer
Time-resolved relaxation and fragmentation of polycyclic aromatic hydrocarbons investigated in the ultrafast XUV-IR regime
Nature Communications **12** (2021), 1-11.

[52] G. Sloan, E. Lagadec, A. Zijlstra, K. Kraemer, A. Weis, M. Matsuura, K. Volk, E. Peeters, W. Duley, J. Cami
Carbon-rich dust past the asymptotic giant branch: aliphatics, aromatics, and fullerenes in the magellanic clouds
The Astrophysical Journal **791** (2014), 28.

[53] M. Steglich, J. Bouwman, F. Huisken, T. Henning
Can neutral and ionized polycyclic aromatic hydrocarbons be carriers of the ultraviolet extinction bump and the diffuse interstellar bands?
The Astrophysical Journal **742** (2011), 2.

[54] P. Lavvas, M. Sander, M. Kraft, H. Imanaka
Surface chemistry and particle shape: processes for the evolution of aerosols in Titan's atmosphere
The Astrophysical Journal **728** (2011), 80.

[55] O. Altin, S. Eser
Carbon deposit formation from thermal stressing of petroleum fuels
Preprints of Papers-American Chemical Society, Division of Fuel Chemistry **49** (2004), 764-766.

[56] F. Pickl, M. Russer, M. Hauenstein, M. Wensing
Modelling and understanding deposit formation and reduction in combustion engines–Application to the concrete case of internal GDI injector deposit
Fuel **236** (2019), 284-296.

[57] F. Joos
Technische Verbrennung
Springer, Berlin (2006).

[58] W. Pejpichestakul, E. Ranzi, M. Pelucchi, A. Frassoldati, A. Cuoci, A. Parente, T. Faravelli
Examination of a soot model in premixed laminar flames at fuel-rich conditions
Proceedings of the Combustion Institute **37** (2019), 1013-1021.

[59] C. Saggese, S. Ferrario, J. Camacho, A. Cuoci, A. Frassoldati, E. Ranzi, H. Wang, T. Faravelli
Kinetic modeling of particle size distribution of soot in a premixed burner-stabilized stagnation ethylene flame
Combustion and Flame **162** (2015), 3356-3369.

[60] D. G. Goodwin, H. K. Moffat, R. L. Speth
Cantera: An object-oriented software toolkit for chemical kinetics, thermodynamics, and transport processes
Caltech, Pasadena, CA **124** (2009).

[61] G. P. Smith, D. M. Golden, M. Frenklach, N. W. Moriarty, B. Eiteneer, M. Goldenberg, C. T. Bowman, R. K. Hanson, S. Song, W. C. Gardiner, V. V. Lissianski, Z. Qin
GRI-Mech 3.0
http://www.me.berkeley.edu/gri_mech/ (2021), accessed 13 August 2021.

[62] H. Wang, M. Frenklach
A detailed kinetic modeling study of aromatics formation in laminar premixed acetylene and ethylene flames
Combustion and Flame **110** (1997), 173-221.

[63] S. Rigopoulos
Modelling of soot aerosol dynamics in turbulent flow
Flow, Turbulence and Combustion **103** (2019), 565-604.

[64] C. S. McEnally, L. D. Pfefferle, B. Atakan, K. Kohse-Höinghaus
Studies of aromatic hydrocarbon formation mechanisms in flames: Progress towards closing the fuel gap
Progress in Energy and Combustion Science **32** (2006), 247-294.

[65] J. Warnatz, U. Maas, R. W. Dibble, J. Warnatz
Combustion
Springer, Berlin Heidelberg (2006).

[66] J. B. Michael, P. Venkateswaran, C. R. Shaddix, T. R. Meyer
Effects of repetitive pulsing on multi-kHz planar laser-induced incandescence imaging in laminar and turbulent flames
Applied Optics **54** (2015), 3331-3344.

[67] F. Xu, P. Sunderland, G. Faeth
Soot formation in laminar premixed ethylene/air flames at atmospheric pressure
Combustion and Flame **108** (1997), 471-493.

[68] A. V. Eremin, E. V. Gurentsov, R. N. Kolotushkin, E. Y. Mikheyeva
Dependence of Soot Primary Particle Size on the Height above a Burner in Target Ethylene/air Premixed Flame
Combustion Science and Technology **193** (2021), 1-17.

[69] Z. Mansurov
Soot formation in combustion processes
Combustion, Explosion and Shock Waves **41** (2005), 727-744.

[70] H. A. Michelsen, M. B. Colket, P.-E. Bengtsson, A. D'Anna, P. Desgroux, B. S. Haynes, J. H. Miller, G. J. Nathan, H. Pitsch, H. Wang
A review of terminology used to describe soot formation and evolution under combustion and pyrolytic conditions
ACS Nano **14** (2020), 12470-12490.

[71] R. Obertacke, H. Wintrich, F. Wintrich, A. Leipertz
A new sensor system for industrial combustion monitoring and control using UV emission spectroscopy and tomography
Combustion Science and Technology **121** (1996), 133-151.

[72] V. Smith, J. Robinson
Ultraviolet emission and absorption spectra produced by organic compounds in oxyhydrogen flames 1: Emission spectra
Analytica Chimica Acta **48** (1969), 391-403.

[73] P.-E. Bengtsson, M. Aldén
C2 production and excitation in sooting flames using visible laser radiation: implications for diagnostics in sooting flames
Combustion Science and Technology **77** (1991), 307-318.

[74] J. S. Brooke, P. F. Bernath, T. W. Schmidt, G. B. Bacskay
Line strengths and updated molecular constants for the C2 Swan system
Journal of Quantitative Spectroscopy and Radiative Transfer **124** (2013), 11-20.

[75] B.-L. Hu, J. Zhang, K.-Q. Cao, S.-J. Hao, D.-X. Sun, Y.-N. Liu
Research on the etalon effect in dispersive hyperspectral VNIR imagers using back-illuminated CCDs
IEEE Transactions on Geoscience and Remote Sensing **56** (2018), 5481-5494.

[76] K. Gleason, F. Carbone, A. Gomez
Effect of temperature on soot inception in highly controlled counterflow ethylene diffusion flames
Combustion and Flame **192** (2018), 283-294.

[77] Y. Wang, S. H. Chung
Soot formation in laminar counterflow flames
Progress in Energy and Combustion Science **74** (2019), 152-238.

[78] N. J. Kempema, B. Ma, M. B. Long
Investigation of in-flame soot optical properties in laminar coflow diffusion flames using thermophoretic particle sampling and spectral light extinction
Applied Physics B **122** (2016), 1-13.

[79] M. R. Kholghy, Y. Afarin, A. D. Sediako, J. Barba, M. Lapuerta, C. Chu, J. Weingarten, B. Borshanpour, V. Chernov, M. J. Thomson
Comparison of multiple diagnostic techniques to study soot formation and morphology in a diffusion flame
Combustion and Flame **176** (2017), 567-583.

[80] F. Liu, H. Guo, G. J. Smallwood
Effects of radiation model on the modeling of a laminar coflow methane/air diffusion flame
Combustion and Flame **138** (2004), 136-154.

[81] M. Smooke, R. Hall, M. Colket, J. Fielding, M. Long, C. McEnally, L. Pfefferle
Investigation of the transition from lightly sooting towards heavily sooting co-flow ethylene diffusion flames
Combustion Theory and Modelling **8** (2004), 593.

[82] T. Yu, F. J. Bauer, F. J. T. Huber, S. Will, W. Cai
4D temperature measurements using tomographic two-color pyrometry
Optics Express **29** (2021), 5304-5315.

[83] R. L. Vander Wal, A. J. Tomasek
Soot nanostructure: dependence upon synthesis conditions
Combustion and Flame **136** (2004), 129-140.

[84] D. R. Tree, K. I. Svensson
Soot processes in compression ignition engines
Progress in Energy and Combustion Science **33** (2007), 272-309.

[85] F. Altendorfner, F. Beyrau, A. Leipertz, T. Hammer, D. Most, G. Lins, D. W. Branston
Technical feasibility of electric field control for turbulent premixed flames
Chemical Engineering & Technology **33** (2010), 647-653.

[86] A. E. Karataş, Ö. L. Gülder
Soot formation in high pressure laminar diffusion flames
Progress in Energy and Combustion Science **38** (2012), 818-845.

[87] X. Mi, A. Saylam, T. Endres, C. Schulz, T. Dreier
Near-threshold soot formation in premixed flames at elevated pressure
Carbon **181** (2021), 143-154.

[88] A. Sakhrieh, G. Lins, F. Dinkelacker, T. Hammer, A. Leipertz, D. Branston
The influence of pressure on the control of premixed turbulent flames using an electric field
Combustion and Flame **143** (2005), 313-322.

[89] P. Desgroux, A. Faccinetto, X. Mercier, T. Mouton, D. A. Karkar, A. El Bakali
Comparative study of the soot formation process in a "nucleation" and a "sooting" low pressure premixed methane flame
Combustion and Flame **184** (2017), 153-166.

[90] M. Wartel, J.-F. Pauwels, P. Desgroux, X. Mercier
Quantitative measurement of naphthalene in low-pressure flames by jet-cooled laser-induced fluorescence
Applied Physics B **100** (2010), 933-943.

[91] R. C. Huber, B. S. Ringstrand, D. M. Dattelbaum, R. L. Gustavsen, S. Seifert, M. A. Firestone, D. W. Podlesak
Extreme condition nanocarbon formation under air and argon atmospheres during detonation of composition B-3
Carbon **126** (2018), 289-298.

[92] A. Baldelli, U. Trivanovic, T. A. Sipkens, S. N. Rogak
On determining soot maturity: A review of the role of microscopy-and spectroscopy-based techniques
Chemosphere **252** (2020), 126532.

[93] H. Michelsen
Probing soot formation, chemical and physical evolution, and oxidation: A review of in situ diagnostic techniques and needs
Proceedings of the Combustion Institute **36** (2017), 717-735.

[94] K. Kohse-Höinghaus, B. Atakan, A. Lamprecht, G. G. Alatorre, M. Kamphus, T. Kasper, N.-N. Liu
Contributions to the investigation of reaction pathways in fuel-rich flames
Physical Chemistry Chemical Physics **4** (2002), 2056-2062.

[95] J. A. Miller, S. J. Klippenstein
The recombination of propargyl radicals and other reactions on a C6H6 potential
The Journal of Physical Chemistry A **107** (2003), 7783-7799.

[96] N. Hansen, S. J. Klippenstein, C. A. Taatjes, J. A. Miller, J. Wang, T. A. Cool, B. Yang, R. Yang, L. Wei, C. Huang
Identification and chemistry of C4H3 and C4H5 isomers in fuel-rich flames
The Journal of Physical Chemistry A **110** (2006), 3670-3678.

[97] M. Frenklach
Reaction mechanism of soot formation in flames
Physical Chemistry Chemical Physics **4** (2002), 2028-2037.

[98] H. Wang
Formation of nascent soot and other condensed-phase materials in flames
Proceedings of the Combustion Institute **33** (2011), 41-67.

[99] S. E. Stein, A. Fahr
High-temperature stabilities of hydrocarbons
The Journal of Physical Chemistry **89** (1985), 3714-3725.

[100] B. Öktem, M. P. Tolocka, B. Zhao, H. Wang, M. V. Johnston
Chemical species associated with the early stage of soot growth in a laminar premixed ethylene–oxygen–argon flame
Combustion and Flame **142** (2005), 364-373.

[101] F. Schulz, M. Commodo, K. Kaiser, G. De Falco, P. Minutolo, G. Meyer, D. Andrea, L. Gross
Insights into incipient soot formation by atomic force microscopy
Proceedings of the Combustion Institute **37** (2019), 885-892.

[102] K. Johansson, M. Head-Gordon, P. Schrader, K. Wilson, H. Michelsen
Resonance-stabilized hydrocarbon-radical chain reactions may explain soot inception and growth
Science **361** (2018), 997-1000.

[103] J. Martin
Investigating the role of curvature on the formation and thermal transformations of soot
University of Cambridge (PhD thesis), (2020).

[104] A. Menon, J. A. Dreyer, J. W. Martin, J. Akroyd, J. Robertson, M. Kraft
Optical band gap of cross-linked, curved, and radical polyaromatic hydrocarbons
Physical Chemistry Chemical Physics **21** (2019), 16240-16251.

[105] T. S. Totton, A. J. Misquitta, M. Kraft
A quantitative study of the clustering of polycyclic aromatic hydrocarbons at high temperatures
Physical Chemistry Chemical Physics **14** (2012), 4081-4094.

[106] A. Faccinetto, C. Irimiea, P. Minutolo, M. Commodo, A. D'anna, N. Nuns, Y. Carpentier, C. Pirim, P. Desgroux, C. Focsa
Evidence on the formation of dimers of polycyclic aromatic hydrocarbons in a laminar diffusion flame
Communications Chemistry **3** (2020), 1-8.

[107] M. Sirignano, C. Russo
Pyrene dimerization in controlled temperature environment: An experimental study
Proceedings of the Combustion Institute **38** (2021), 1173-1180.

[108] J. W. Martin, K. Bowal, A. Menon, R. I. Slavchov, J. Akroyd, S. Mosbach, M. Kraft
Polar curved polycyclic aromatic hydrocarbons in soot formation
Proceedings of the Combustion Institute **37** (2019), 1117-1123.

[109] P. Toth
Nanostructure quantification of turbostratic carbon by HRTEM image analysis: state of the art, biases, sensitivity and best practices
Carbon **178** (2021), 688-707.

[110] L. Pascazio, J. W. Martin, A. Menon, D. Hou, X. You, M. Kraft
Aromatic penta-linked hydrocarbons in soot nanoparticle formation
Proceedings of the Combustion Institute **38** (2021), 1525-1532.

[111] M. Frenklach
On surface growth mechanism of soot particles
Symposium International on Combustion **26** (1996), 2285-2293.

[112] H.-B. Zhang, D. Hou, C. K. Law, X. You
Role of carbon-addition and hydrogen-migration reactions in soot surface growth
The Journal of Physical Chemistry A **120** (2016), 683-689.

[113] M. Frenklach, A. M. Mebel
On the mechanism of soot nucleation
Physical Chemistry Chemical Physics **22** (2020), 5314-5331.

[114] M. Frenklach, R. I. Singh, A. M. Mebel
On the low-temperature limit of HACA
Proceedings of the Combustion Institute **37** (2019), 969-976.

[115] J. Yon, J. Morán, F.-X. Ouf, M. Mazur, J. Mitchell
From monomers to agglomerates: A generalized model for characterizing the morphology of fractal-like clusters
Journal of Aerosol Science **151** (2021), 105628.

[116] J. Morán, A. Poux, J. Yon
Impact of the competition between aggregation and surface growth on the morphology of soot particles formed in an ethylene laminar premixed flame
Journal of Aerosol Science **152** (2021), 105690.

[117] J. Morán, A. Fuentes, F. Liu, J. Yon
FracVAL: An improved tunable algorithm of cluster–cluster aggregation for generation of fractal structures formed by polydisperse primary particles
Computer Physics Communications **239** (2019), 225-237.

[118] B. R. Stanmore, J.-F. Brilhac, P. Gilot
The oxidation of soot: a review of experiments, mechanisms and models
Carbon **39** (2001), 2247-2268.

[119] F. P. Hagen, H. Bockhorn, H. Störmer, A. Loukou, R. Suntz, D. Trimis
Nanostructural and morphological characteristics of single soot aggregates during low-temperature oxidation
Proceedings of the Combustion Institute **38** (2021), 1153-1161.

[120] J. Yon, F.-X. Ouf, D. Hébert, J. B. Mitchell, N. Teuscher, J.-L. Le Garrec, A. Bescond, W. Baumann, D. Ourdani, T. Bizien
Investigation of soot oxidation by coupling LII, SAXS and scattering measurements
Combustion and Flame **190** (2018), 441-453.

[121] K. Johansson, F. El Gabaly, P. Schrader, M. Campbell, H. Michelsen
Evolution of maturity levels of the particle surface and bulk during soot growth and oxidation in a flame
Aerosol Science and Technology **51** (2017), 1333-1344.

[122] P. Desgroux, X. Mercier, K. A. Thomson
Study of the formation of soot and its precursors in flames using optical diagnostics
Proceedings of the Combustion Institute **34** (2013), 1713-1738.

[123] H.-Q. Do, L.-S. Tran, L. Gasnot, X. Mercier, A. El Bakali
Experimental study of the influence of hydrogen as a fuel additive on the formation of soot precursors and particles in atmospheric laminar premixed flames of methane
Fuel **287** (2021), 119517.

[124] G. A. Kelesidis, S. E. Pratsinis
Determination of the volume fraction of soot accounting for its composition and morphology
Proceedings of the Combustion Institute **38** (2021), 1189-1196.

[125] P. F. DeCarlo, J. G. Slowik, D. R. Worsnop, P. Davidovits, J. L. Jimenez
Particle morphology and density characterization by combined mobility and aerodynamic diameter measurements. Part 1: Theory
Aerosol Science and Technology **38** (2004), 1185-1205.

[126] G. A. Kelesidis, E. Goudeli, S. E. Pratsinis
Morphology and mobility diameter of carbonaceous aerosols during agglomeration and surface growth
Carbon **121** (2017), 527-535.

[127] A. D. Abid, J. Camacho, D. A. Sheen, H. Wang
Quantitative measurement of soot particle size distribution in premixed flames–the burner-stabilized stagnation flame approach
Combustion and Flame **156** (2009), 1862-1870.

[128] A. M. Brasil, T. L. Farias, M. G. Carvalho
A recipe for image characterization of fractal-like aggregates
Journal of Aerosol Science **30** (1999), 1379-1389.

[129] D. Cortés, J. Morán, F. Liu, F. Escudero, J.-L. Consalvi, A. Fuentes
Effect of fuels and oxygen indices on the morphology of soot generated in laminar coflow diffusion flames
Energy & Fuels **32** (2018), 11802-11813.

[130] C. Oh, C. M. Sorensen
The effect of overlap between monomers on the determination of fractal cluster morphology
Journal of Colloid and Interface Science **193** (1997), 17-25.

[131] J. Yon, J. J. Cruz, F. Escudero, J. Morán, F. Liu, A. Fuentes
Revealing soot maturity based on multi-wavelength absorption/emission measurements in laminar axisymmetric coflow ethylene diffusion flames
Combustion and Flame **227** (2021), 147-161.

[132] H. A. Michelsen
Effects of maturity and temperature on soot density and specific heat
Proceedings of the Combustion Institute **38** (2021), 1197-1205.

[133] M. S. Solum, A. F. Sarofim, R. J. Pugmire, T. H. Fletcher, H. Zhang
13C NMR analysis of soot produced from model compounds and a coal
Energy & Fuels **15** (2001), 961-971.

[134] M. Velásquez, F. Mondragón, A. Santamaría
Chemical characterization of soot precursors and soot particles produced in hexane and diesel surrogates using an inverse diffusion flame burner
Fuel **104** (2013), 681-690.

[135] M. Altenhoff, C. Teige, M. Storch, S. Will
Novel electric thermophoretic sampling device with highly repeatable characteristics
Review of Scientific Instruments **87** (2016), 125108.

[136] M. Altenhoff, S. Aßmann, C. Teige, F. J. T. Huber, S. Will
An optimized evaluation strategy for a comprehensive morphological soot nanoparticle aggregate characterization by electron microscopy
Journal of Aerosol Science **139** (2020), 105470.

[137] M. Schenk, S. Lieb, H. Vieker, A. Beyer, A. Gölzhäuser, H. Wang, K. Kohse-Höinghaus
Imaging nanocarbon materials: soot particles in flames are not structurally homogeneous
ChemPhysChem **14** (2013), 3248-3254.

[138] A. Barone, A. D'Alessio, A. D'Anna
Morphological characterization of the early process of soot formation by atomic force microscopy
Combustion and Flame **132** (2003), 181-187.

[139] L. Sgro, G. Basile, A. Barone, A. D'Anna, P. Minutolo, A. Borghese, A. D'Alessio
Detection of combustion formed nanoparticles
Chemosphere **51** (2003), 1079-1090.

[140] N. Jalili, K. Laxminarayana
A review of atomic force microscopy imaging systems: application to molecular metrology and biological sciences
Mechatronics **14** (2004), 907-945.

[141] M. Commodo, K. Kaiser, G. De Falco, P. Minutolo, F. Schulz, A. D'Anna, L. Gross
On the early stages of soot formation: Molecular structure elucidation by high-resolution atomic force microscopy
Combustion and Flame **205** (2019), 154-164.

[142] C. S. Wang, N. C. Bartelt, R. Ragan, K. Thürmer
Revealing the molecular structure of soot precursors
Carbon **129** (2018), 537-542.

[143] S. Veronesi, M. Commodo, L. Basta, G. De Falco, P. Minutolo, N. Kateris, H. Wang, A. D'Anna, S. Heun
Morphology and electronic properties of incipient soot by scanning tunneling microscopy and spectroscopy
Combustion and Flame **(In Press)** (2022), 111980.

[144] G. De Falco, G. Mattiello, M. Commodo, P. Minutolo, X. Shi, A. D'Anna, H. Wang
Electronic band gap of flame-formed carbon nanoparticles by scanning tunneling spectroscopy
Proceedings of the Combustion Institute **38** (2021), 1805-1812.

[145] C. Betrancourt, F. Liu, P. Desgroux, X. Mercier, A. Faccinetto, M. Salamanca, L. Ruwe, K. Kohse-Höinghaus, D. Emmrich, A. Beyer
Investigation of the size of the incandescent incipient soot particles in premixed sooting and nucleation flames of n-butane using LII, HIM, and 1 nm-SMPS
Aerosol Science and Technology **51** (2017), 916-935.

[146] M. Schenk, S. Lieb, H. Vieker, A. Beyer, A. Gölzhäuser, H. Wang, K. Kohse-Höinghaus
Morphology of nascent soot in ethylene flames
Proceedings of the Combustion Institute **35** (2015), 1879-1886.

[147] J. Davis, E. Molnar, I. Novosselov
Nanostructure transition of young soot aggregates to mature soot aggregates in diluted diffusion flames
Carbon **159** (2020), 255-265.

[148] K. Wan, D. Chen, H. Wang
On imaging nascent soot by transmission electron microscopy
Combustion and Flame **198** (2018), 260-266.

[149] N. Hansen, T. A. Cool, P. R. Westmoreland, K. Kohse-Höinghaus
Recent contributions of flame-sampling molecular-beam mass spectrometry to a fundamental understanding of combustion chemistry
Progress in Energy and Combustion Science **35** (2009), 168-191.

[150] A. Tregrossi, A. Ciajolo, R. Barbella
The combustion of benzene in rich premixed flames at atmospheric pressure
Combustion and Flame **117** (1999), 553-561.

[151] A. Michela, A. Barbara, T. Antonio, C. Anna
Identification of large polycyclic aromatic hydrocarbons in carbon particulates formed in a fuel-rich premixed ethylene flame
Carbon **46** (2008), 2059-2066.

[152] F. Qi
Combustion chemistry probed by synchrotron VUV photoionization mass spectrometry
Proceedings of the Combustion Institute **34** (2013), 33-63.

[153] T. S. Kasper, P. Oßwald, M. Kamphus, K. Kohse-Höinghaus
Ethanol flame structure investigated by molecular beam mass spectrometry
Combustion and Flame **150** (2007), 220-231.

[154] C. Gehm, T. Streibel, J. Passig, R. Zimmermann
Determination of relative ionization cross sections for resonance enhanced multiphoton ionization of polycyclic aromatic hydrocarbons
Applied Sciences **8** (2018), 1617.

[155] L. Dupont, A. El Bakali, J.-F. Pauwels, I. Da Costa, P. Meunier, H. Richter
Investigation of stoichiometric methane/air/benzene (1.5%) and methane/air low pressure flames
Combustion and Flame **135** (2003), 171-183.

[156] X. Mercier, M. Wartel, J.-F. Pauwels, P. Desgroux
Implementation of a new spectroscopic method to quantify aromatic species involved in the formation of soot particles in flames
Applied Physics B **91** (2008), 387-395.

[157] B. Giechaskiel, E. Schiefer, W. Schindler, H. Axmann, C. Dardiotis
Overview of soot emission measurements instrumentation: from smoke and filter mass to particle number
SAE International Journal of Engines **6** (2013), 10-22.

[158] M. N. Ess, M. Berto, A. Keller, M. Gysel-Beer, K. Vasilatou
Coated soot particles with tunable, well-controlled properties generated in the laboratory with a miniCAST BC and a micro smog chamber
Journal of Aerosol Science **157** (2021), 105820.

[159] M. K. Lappi, J. M. Ristimäki
Comparison of filter smoke number and elemental carbon from thermal optical analysis of marine diesel engine exhaust
Proceedings of the Institution of Mechanical Engineers, Part M: Journal of Engineering for the Maritime Environment **233** (2019), 602-609.

[160] V. Krüger, C. Wahl, R. Hadef, K. P. Geigle, W. Stricker, M. Aigner
Comparison of laser-induced incandescence method with scanning mobility particle sizer technique: the influence of probe sampling and laser heating on soot particle size distribution
Measurement Science and Technology **16** (2005), 1477.

[161] J. Camacho, C. Liu, C. Gu, H. Lin, Z. Huang, Q. Tang, X. You, C. Saggese, Y. Li, H. Jung
Mobility size and mass of nascent soot particles in a benchmark premixed ethylene flame
Combustion and Flame **162** (2015), 3810-3822.

[162] J. Tröstl, T. Tritscher, O. F. Bischof, H.-G. Horn, T. Krinke, U. Baltensperger, M. Gysel
Fast and precise measurement in the sub-20 nm size range using a Scanning Mobility Particle Sizer
Journal of Aerosol Science **87** (2015), 75-87.

[163] C. Gu, H. Lin, J. Camacho, B. Lin, C. Shao, R. Li, H. Gu, B. Guan, Z. Huang, H. Wang
Particle size distribution of nascent soot in lightly and heavily sooting premixed ethylene flames
Combustion and Flame **165** (2016), 177-187.

[164] B. Liang, Y. Ge, J. Tan, X. Han, L. Gao, L. Hao, W. Ye, P. Dai
Comparison of PM emissions from a gasoline direct injected (GDI) vehicle and a port fuel injected (PFI) vehicle measured by electrical low pressure impactor (ELPI) with two fuels: Gasoline and M15 methanol gasoline
Journal of Aerosol Science **57** (2013), 22-31.

[165] C. Van Gulijk, J. C. Marijnissen, M. Makkee, J. A. Moulijn
The choice of instrument (ELPI and/or SMPS) for Diesel soot particulate measurements
SAE Technical Paper (2003), 0784.

[166] P. Baltzopoulou, M. Kostoglou, E. Papaioannou, A. G. Konstandopoulos
On the Effective Density and Fractal–Like Dimension of Diesel Soot Aggregates as a Function of Mobility Diameter
Emission Control Science and Technology **4** (2018), 240-246.

[167] J. Ribeiro-Soares, M. Oliveros, C. Garin, M. David, L. Martins, C. Almeida, E. Martins-Ferreira, K. Takai, T. Enoki, R. Magalhães-Paniago
Structural analysis of polycrystalline graphene systems by Raman spectroscopy
Carbon **95** (2015), 646-652.

[168] A. Sadezky, H. Muckenhuber, H. Grothe, R. Niessner, U. Pöschl
Raman microspectroscopy of soot and related carbonaceous materials: Spectral analysis and structural information
Carbon **43** (2005), 1731-1742.

[169] K. Dieter, K. Koschnick, J. Lill, G. Magnotti, A. Weinmann, A. Dreizler, D. Geyer
Development of a Raman spectrometer for the characterization of gaseous hydrocarbons at high temperatures
Journal of Quantitative Spectroscopy and Radiative Transfer **277** (2022), 107978.

[170] K. C. Le, C. Lefumeux, T. Pino
Watching soot inception via online Raman spectroscopy
Combustion and Flame **236** (2022), 111817.

[171] K. C. Le, C. Lefumeux, P.-E. Bengtsson, T. Pino
Direct observation of aliphatic structures in soot particles produced in low-pressure premixed ethylene flames via online Raman spectroscopy
Proceedings of the Combustion Institute **37** (2019), 869-876.

[172] M. Commodo, A. E. Karataş, G. De Falco, P. Minutolo, A. D'Anna, Ö. L. Gülder
On the effect of pressure on soot nanostructure: A Raman spectroscopy investigation
Combustion and Flame **219** (2020), 13-19.

[173] A. Baldelli, S. N. Rogak
Morphology and Raman spectra of aerodynamically classified soot samples
Atmospheric Measurement Techniques **12** (2019), 4339-4346.

[174] M. Ess, D. Ferry, E. Kireeva, R. Niessner, F.-X. Ouf, N. Ivleva
In situ Raman microspectroscopic analysis of soot samples with different organic carbon content: Structural changes during heating
Carbon **105** (2016), 572-585.

[175] G. Vitiello, G. De Falco, F. Picca, M. Commodo, G. D'Errico, P. Minutolo, A. D'Anna
Role of radicals in carbon clustering and soot inception: A combined EPR and Raman spectroscopic study
Combustion and Flame **205** (2019), 286-294.

[176] A. C. Ferrari, J. Robertson
Raman spectroscopy of amorphous, nanostructured, diamond–like carbon, and nanodiamond
Philosophical Transactions of the Royal Society of London. Series A **362** (2004), 2477-2512.

[177] J. D. Herdman, B. C. Connelly, M. D. Smooke, M. B. Long, J. H. Miller
A comparison of Raman signatures and laser-induced incandescence with direct numerical simulation of soot growth in non-premixed ethylene/air flames
Carbon **49** (2011), 5298-5311.

[178] C. Russo, A. Ciajolo
Effect of the flame environment on soot nanostructure inferred by Raman spectroscopy at different excitation wavelengths
Combustion and Flame **162** (2015), 2431-2441.

[179] M. W. Smith, I. Dallmeyer, T. J. Johnson, C. S. Brauer, J.-S. McEwen, J. F. Espinal, M. Garcia-Perez
Structural analysis of char by Raman spectroscopy: Improving band assignments through computational calculations from first principles
Carbon **100** (2016), 678-692.

[180] M. Commodo, G. De Falco, A. Bruno, C. Borriello, P. Minutolo, A. D'Anna
Physicochemical evolution of nascent soot particles in a laminar premixed flame: from nucleation to early growth
Combustion and Flame **162** (2015), 3854-3863.

[181] M. Commodo, P. H. Joo, G. De Falco, P. Minutolo, A. D'Anna, O. m. L. Gülder
Raman spectroscopy of soot sampled in high-pressure diffusion flames
Energy & Fuels **31** (2017), 10158-10164.

[182] K. C. Le, J. Henriksson, P. E. Bengtsson
Polarization effects in Raman spectroscopy of light-absorbing carbon
Journal of Raman Spectroscopy **52** (2021), 1115-1122.

[183] H. Kim, M. Aldén, C. Brackmann
Suppression of unpolarized background interferences for Raman spectroscopy under continuous operation
Optics Express **29** (2021), 1048-1063.

[184] S. Roy, J. R. Gord, A. K. Patnaik
Recent advances in coherent anti-Stokes Raman scattering spectroscopy: Fundamental developments and applications in reacting flows
Progress in Energy and Combustion Science **36** (2010), 280-306.

[185] A. Hosseinnia, M. Ruchkina, P. Ding, J. Bood, P.-E. Bengtsson
Single-shot fs/ns rotational CARS for temporally and spectrally resolved gas-phase diagnostics
Proceedings of the Combustion Institute **38** (2021), 1843-1850.

[186] F. Migliorini, S. De Iuliis, R. Dondè, M. Commodo, P. Minutolo, A. D'Anna
Nanosecond laser irradiation of soot particles: Insights on structure and optical properties
Experimental Thermal and Fluid Science **114** (2020), 110064.

[187] C. Wang, Q. N. Chan, S. Kook, E. R. Hawkes, J. Lee, P. R. Medwell
External irradiation effect on the growth and evolution of in-flame soot species
Carbon **102** (2016), 161-171.

[188] R. Willems, P. Bakker, N. Dam
Laser-induced incandescence versus photo-acoustics: implications for qualitative soot size diagnostics
Applied Physics B **125** (2019), 1-9.

[189] A. C. Eckbreth
Laser diagnostics for combustion temperature and species
CRC press, New York (1996).

[190] A. Portnov, S. Rosenwaks, I. Bar
Emission following laser-induced breakdown spectroscopy of organic compounds in ambient air
Applied Optics **42** (2003), 2835-2842.

[191] Y. Zhang, S. Li, Y. Ren, Q. Yao, C. K. Law
Two-dimensional imaging of gas-to-particle transition in flames by laser-induced nanoplasmas
Applied Physics Letters **104** (2014), 023115.

[192] Y. Zhang, S. Li, Y. Ren, Q. Yao, D. T. Stephen
A new diagnostic for volume fraction measurement of metal-oxide nanoparticles in flames using phase-selective laser-induced breakdown spectroscopy
Proceedings of the Combustion Institute **35** (2015), 3681-3688.

[193] J. M. Herzog, D. Witkowski, D. A. Rothamer
Combustion-relevant aerosol phosphor thermometry imaging using Ce, Pr: LuAG, Ce: GdPO4, and Ce: CSSO
Proceedings of the Combustion Institute **38** (2021), 1617-1625.

[194] S. Someya
Particle-based temperature measurement coupled with velocity measurement
Measurement Science and Technology **32** (2021), 042001.

[195] D. Witkowski, D. A. Rothamer
Precise surface temperature measurements from 400 to 1200 K using the Pr: YAG phosphor
Applied Physics B **127** (2021), 1-10.

[196] C. Haisch, P. Menzenbach, H. Bladt, R. Niessner
A wide spectral range photoacoustic aerosol absorption spectrometer
Analytical Chemistry **84** (2012), 8941-8945.

[197] G. Humphries, J. Dunn, M. Hossain, M. Lengden, I. Burns, J. Black
A simple photoacoustic method for the in situ study of soot distribution in flames
Applied Physics B **119** (2015), 709-715.

[198] S. Di Stasio
Soot with 1013 cm− 3 high concentration and 25 Å radius of gyration as detected by small-angle X-ray scattering in a premixed ethylene-air flame at sooting threshold
Journal of Aerosol Science **110** (2017), 11-24.

[199] F. Zhang, C. Wang, W. Han, Y. Zou, J. Wang, S. Seifert, R. E. Winans
Soot formation and growth with palladium acetylacetonate-toluene injection in ethylene base flames investigated by in situ synchrotron small-angle X-ray scattering
Proceedings of the Combustion Institute **38** (2021), 1859-1866.

[200] J. Mitchell, S. Di Stasio, J.-L. LeGarrec, A. I. Florescu-Mitchell, T. Narayanan, M. Sztucki
Small angle x-ray scattering study of flame soot nanoparticle aggregation and restructuring
Journal of Applied Physics **105** (2009), 124904.

[201] P. Bauer, H. Amenitsch, B. Baumgartner, G. Köberl, C. Rentenberger, P. Winkler
In-situ aerosol nanoparticle characterization by small angle X-ray scattering at ultra-low volume fraction
Nature Communications **10** (2019), 1-7.

[202] F. Ossler, L. Vallenhag, S. E. Canton, J. B. A. Mitchell, J.-L. Le Garrec, M. Sztucki, S. Di Stasio
Dynamics of incipient carbon particle formation in a stabilized ethylene flame by in situ extended-small-angle-and wide-angle X-ray scattering
Carbon **51** (2013), 1-19.

[203] F. Ossler, S. E. Canton, L. R. Wallenberg, A. Engdahl, S. Seifert, J. P. Hessler, R. S. Tranter
Measurements of structures and concentrations of carbon particle species in premixed flames by the use of in-situ wide angle X-ray scattering
Carbon **96** (2016), 782-798.

[204] A. Braun, F. Huggins, N. Shah, Y. Chen, S. Wirick, S. Mun, C. Jacobsen, G. Huffman
Advantages of soft X-ray absorption over TEM-EELS for solid carbon studies—a comparative study on diesel soot with EELS and NEXAFS
Carbon **43** (2005), 117-124.

[205] J. H. Frank, A. Shavorskiy, H. Bluhm, B. Coriton, E. Huang, D. L. Osborn
In situ soft X-ray absorption spectroscopy of flames
Applied Physics B **117** (2014), 493-499.

[206] F.-X. Ouf, P. Parent, C. Laffon, I. Marhaba, D. Ferry, B. Marcillaud, E. Antonsson, S. Benkoula, X.-J. Liu, C. Nicolas
First in-flight synchrotron X-ray absorption and photoemission study of carbon soot nanoparticles
Scientific Reports **6** (2016), 1-12.

[207] L. J. Higgins, C. J. Sahle, M. Balasubramanian, B. Mishra
X-ray Raman scattering for bulk chemical and structural insight into green carbon
Physical Chemistry Chemical Physics **22** (2020), 18435-18446.

[208] J. Mitchell, J.-L. Le Garrec, A. I. Florescu-Mitchell, S. Di Stasio
Small-angle neutron scattering study of soot particles in an ethylene–air diffusion flame
Combustion and Flame **145** (2006), 80-87.

[209] P.-E. Bengtsson, M. Aldén
Soot-visualization strategies using laser techniques
Applied Physics B **60** (1995), 51-59.

[210] W. G. Bessler, C. Schulz
Quantitative multi-line NO-LIF temperature imaging
Applied Physics B **78** (2004), 519-533.

[211] P. Liu, Z. He, G.-L. Hou, B. Guan, H. Lin, Z. Huang
The diagnostics of laser-induced fluorescence (LIF) spectra of PAHs in flame with TD-DFT: special focus on five-membered ring
The Journal of Physical Chemistry A **119** (2015), 13009-13017.

[212] K. Hayashida, K. Amagai, K. Satoh, M. Arai
Experimental analysis of soot formation in sooting diffusion flame by using laser-induced emissions
Journal of Engineering for Gas Turbines and Power **128** (2006), 241-246.

[213] D. Chorey, M. Koegl, P. Boggavarapu, F. J. Bauer, L. Zigan, S. Will, R. Ravikrishna, D. Deshmukh, Y. N. Mishra
3D mapping of polycyclic aromatic hydrocarbons, hydroxyl radicals, and soot volume fraction in sooting flames using FRAME technique
Applied Physics B **127** (2021), 1-13.

[214] B. R. Halls, N. Jiang, T. R. Meyer, S. Roy, M. N. Slipchenko, J. R. Gord
4D spatiotemporal evolution of combustion intermediates in turbulent flames using burst-mode volumetric laser-induced fluorescence
Optics Letters **42** (2017), 2830-2833.

[215] K. P. Geigle, W. O'Loughlin, R. Hadef, W. Meier
Visualization of soot inception in turbulent pressurized flames by simultaneous measurement of laser-induced fluorescence of polycyclic aromatic hydrocarbons and laser-induced incandescence, and correlation to OH distributions
Applied Physics B **119** (2015), 717-730.

[216] I. S. Burns, C. F. Kaminski
Diode laser induced fluorescence for gas-phase diagnostics
Zeitschrift für Physikalische Chemie **225** (2011), 1343-1366.

[217] D. Gu, Z. Sun, G. J. Nathan, P. R. Medwell, Z. T. Alwahabi, B. B. Dally
Improvement of precision and accuracy of temperature imaging in sooting flames using two-line atomic fluorescence (TLAF)
Combustion and Flame **167** (2016), 481-493.

[218] S. Bejaoui, X. Mercier, P. Desgroux, E. Therssen
Laser induced fluorescence spectroscopy of aromatic species produced in atmospheric sooting flames using UV and visible excitation wavelengths
Combustion and Flame **161** (2014), 2479-2491.

[219] Y. Zhang, B. Xiao, Y. Li, P. Liu, R. Zhan, Z. Huang, H. Lin
LIF diagnostics for selective and quantitative measurement of PAHs in laminar premixed flames
Combustion and Flame **222** (2020), 5-17.

[220] X. Mercier, O. Carrivain, C. Irimiea, A. Faccinetto, E. Therssen
Dimers of polycyclic aromatic hydrocarbons: the missing pieces in the soot formation process
Physical Chemistry Chemical Physics **21** (2019), 8282-8294.

[221] Y. Wang, A. Makwana, S. Iyer, M. Linevsky, R. J. Santoro, T. A. Litzinger, J. O'Connor
Effect of fuel composition on soot and aromatic species distributions in laminar, co-flow flames. Part 1. Non-premixed fuel
Combustion and Flame **189** (2018), 443-455.

[222] I. Mulla, P. Desgroux, B. Lecordier, A. Cessou
Comprehensive characterization of sooting butane jet flames, Part 1: Soot, soot-precursor, and reaction zone
Combustion and Flame **233** (2021), 111595.

[223] R. L. Vander Wal
Soot precursor carbonization: Visualization using LIF and LII and comparison using bright and dark field TEM
Combustion and Flame **112** (1998), 607-616.

[224] L. Zhou, G. Xiong, M. Zhang, L. Chen, S. Ding, L. De Goey
Experimental study of Polycyclic Aromatic Hydrocarbons (PAHs) in n-Heptane laminar diffusion flames from1. 0 to 3.0 bar
Fuel **209** (2017), 265-273.

[225] R. L. Vander Wal, K. A. Jensen, M. Y. Choi
Simultaneous laser-induced emission of soot and polycyclic aromatic hydrocarbons within a gas-jet diffusion flame
Combustion and Flame **109** (1997), 399-414.

[226] M. Commodo, L. Sgro, X. Wang, C. De Lisio, P. Minutolo
Fluorescence anisotropy in a diffusion flame to shed light in the "dark region"
Proceedings of the Combustion Institute **34** (2013), 1845-1852.

[227] C. Sorensen
Light scattering by fractal aggregates: a review
Aerosol Science & Technology **35** (2001), 648-687.

[228] S. Talebi-Moghaddam, F. J. Bauer, F. J. T. Huber, S. Will, K. J. Daun
Inferring soot morphology through multi-angle light scattering using an artificial neural network
Journal of Quantitative Spectroscopy and Radiative Transfer **251** (2020), 106957.

[229] P. Kheirkhah, A. Baldelli, P. Kirchen, S. Rogak
Development and validation of a multi-angle light scattering method for fast engine soot mass and size measurements
Aerosol Science and Technology **54** (2020), 1083-1101.

[230] F. J. Martins, A. Kronenburg, F. Beyrau
Single-shot two-dimensional multi-angle light scattering (2D-MALS) technique for nanoparticle aggregate sizing
Applied Physics B **127** (2021), 1-15.

[231] F. J. T. Huber, S. Will, K. J. Daun
Sizing aerosolized fractal nanoparticle aggregates through Bayesian analysis of wide-angle light scattering (WALS) data
Journal of Quantitative Spectroscopy and Radiative Transfer **184** (2016), 27-39.

[232] H. Oltmann, J. Reimann, S. Will
Wide-angle light scattering (WALS) for soot aggregate characterization
Combustion and Flame **157** (2010), 516-522.

[233] S. Aßmann, B. Münsterjohann, F. J. T. Huber, S. Will
In Situ Determination of Droplet and Nanoparticle Size Distributions in Spray Flame Synthesis by Wide-Angle Light Scattering (WALS)
Materials **14** (2021), 6698.

[234] J. Yon, J. Morán, F. Lespinasse, F. Escudero, G. Godard, M. Mazur, F. Liu, A. Fuentes
Horizontal Planar Angular Light Scattering (HPALS) characterization of soot produced in a laminar axisymmetric coflow ethylene diffusion flame
Combustion and Flame **232** (2021), 111539.

[235] M. L. Botero, J. Akroyd, D. Chen, M. Kraft, J. R. Agudelo
On the thermophoretic sampling and TEM-based characterisation of soot particles in flames
Carbon **171** (2021), 711-722.

[236] M. Altenhoff, S. Aßmann, J. F. A. Perlitz, F. J. T. Huber, S. Will
Soot aggregate sizing in an extended premixed flame by high-resolution two-dimensional multi-angle light scattering (2D-MALS)
Applied Physics B **125** (2019), 1-15.

[237] M. Bouvier, J. Yon, G. Lefevre, F. Grisch
A novel approach for in-situ soot size distribution measurement based on spectrally resolved light scattering
Journal of Quantitative Spectroscopy and Radiative Transfer **225** (2019), 58-68.

[238] J.-Y. Zhang, H. Qi, Y.-F. Wang, B.-H. Gao, L.-M. Ruan
Retrieval of fractal dimension and size distribution of non-compact soot aggregates from relative intensities of multi-wavelength angular-resolved light scattering
Optics Express **27** (2019), 1613-1631.

[239] A. Karlsson, S. Török, A. Roth, P.-E. Bengtsson
Numerical scattering simulations for estimating soot aggregate morphology from nephelometer scattering measurements
Journal of Aerosol Science **159** (2022), 105828.

[240] J. Reimann, S.-A. Kuhlmann, S. Will
2D aggregate sizing by combining laser-induced incandescence (LII) and elastic light scattering (ELS)
Applied Physics B **96** (2009), 583-592.

[241] P. O. Witze, S. Hochgreb, D. Kayes, H. A. Michelsen, C. R. Shaddix
Time-resolved laser-induced incandescence and laser elastic-scattering measurements in a propane diffusion flame
Applied Optics **40** (2001), 2443-2452.

[242] R. K. Hanson, R. M. Spearrin, C. S. Goldenstein
Spectroscopy and optical diagnostics for gases
Springer, Switzerland (2016).

[243] K. C. Cossel, E. M. Waxman, I. A. Finneran, G. A. Blake, J. Ye, N. R. Newbury
Gas-phase broadband spectroscopy using active sources: progress, status, and applications
Journal of the Optical Society of America B **34** (2017), 104-129.

[244] L. Ma, K. Duan, K.-P. Cheong, C. Yuan, W. Ren
Multispectral infrared absorption spectroscopy for quantitative temperature measurements in axisymmetric laminar premixed sooting flames
Case Studies in Thermal Engineering **28** (2021), 101575.

[245] P. Fendt, M. Brandl, A. Peter, L. Zigan, S. Will
Herriott cell enhanced SMF-coupled multi-scalar combustion diagnostics in a rapid compression expansion machine by supercontinuum laser absorption spectroscopy
Optics Express **29** (2021), 42184-42207.

[246] L. H. Ma, L. Y. Lau, W. Ren
Non-uniform temperature and species concentration measurements in a laminar flame using multi-band infrared absorption spectroscopy
Applied Physics B **123** (2017), 83.

[247] J. Emmert, M. Baroncelli, H. Pitsch, S. Wagner
Axisymmetric linear hyperspectral absorption spectroscopy and residuum-based parameter selection on a counter flow burner
Energies **12** (2019), 2786.

[248] S. J. Grauer
Bayesian methods for gas-phase tomography
University of Waterloo (PhD thesis), (2018).

[249] I. E. Gordon, L. S. Rothman, C. Hill, R. V. Kochanov, Y. Tan, P. F. Bernath, M. Birk, V. Boudon, A. Campargue, K. Chance
The HITRAN2016 molecular spectroscopic database
Journal of Quantitative Spectroscopy and Radiative Transfer **203** (2017), 3-69.

[250] L. S. Rothman, I. Gordon, R. Barber, H. Dothe, R. R. Gamache, A. Goldman, V. Perevalov, S. Tashkun, J. Tennyson
HITEMP, the high-temperature molecular spectroscopic database
Journal of Quantitative Spectroscopy and Radiative Transfer **111** (2010), 2139-2150.

[251] A. Malarski, F. Beyrau, A. Leipertz
Interference effects of C2-radicals in nitrogen vibrational CARS thermometry using a frequency-doubled Nd: YAG laser
Journal of Raman Spectroscopy **36** (2005), 102-108.

[252] L. Bizet, R. Vallon, B. Parvitte, M. Brun, G. Maisons, M. Carras, V. Zeninari
Multi-gas sensing with quantum cascade laser array in the mid-infrared region
Applied Physics B **123** (2017), 1-6.

[253] G. Laurens, M. Rabary, J. Lam, D. Peláez, A.-R. Allouche
Infrared spectra of neutral polycyclic aromatic hydrocarbons based on machine learning potential energy surface and dipole mapping
Theoretical Chemistry Accounts **140** (2021), 1-12.

[254] A. Ciajolo, R. Barbella, A. Tregrossi, L. Bonfanti
Spectroscopic and compositional signatures of PAH-loaded mixtures in the soot inception region of a premixed ethylene flame
Symposium (International) on Combustion, (1998), 1481-1487.

[255] W. Karcher
Spectral Atlas of Polycyclic Aromatic Compounds: Including Data on Physico-Chemical Properties, Occurrence and Biological Activity
Springer Science & Business Media, Luxembourg (2013).

[256] M. Schnaiter, H. Horvath, O. Möhler, K.-H. Naumann, H. Saathoff, O. Schöck
UV-VIS-NIR spectral optical properties of soot and soot-containing aerosols
Journal of Aerosol Science **34** (2003), 1421-1444.

[257] A. Tregrossi, R. Barbella, A. Ciajolo, M. Alfè
Spectral properties of soot in the UV-visible range
Combustion Science and Technology **179** (2007), 371-385.

[258] J. Simonsson, N.-E. Olofsson, S. Török, P.-E. Bengtsson, H. Bladh
Wavelength dependence of extinction in sooting flat premixed flames in the visible and near-infrared regimes
Applied Physics B **119** (2015), 657-667.

[259] J. A. Dreyer, R. I. Slavchov, E. J. Rees, J. Akroyd, M. Salamanca, S. Mosbach, M. Kraft
Improved methodology for performing the inverse Abel transform of flame images for color ratio pyrometry
Applied Optics **58** (2019), 2662-2670.

[260] M. Leschowski, K. Thomson, D. Snelling, C. Schulz, G. Smallwood
Combination of LII and extinction measurements for determination of soot volume fraction and estimation of soot maturity in non-premixed laminar flames
Applied Physics B **119** (2015), 685-696.

[261] S. De Iuliis, M. Barbini, S. Benecchi, F. Cignoli, G. Zizak
Determination of the soot volume fraction in an ethylene diffusion flame by multiwavelength analysis of soot radiation
Combustion and Flame **115** (1998), 253-261.

[262] F. Migliorini, S. Belmuso, S. Maffi, R. Dondè, S. De Iuliis
In-flow optical characterization of flame-generated carbon nanoparticles sampled from a premixed flame
Physical Chemistry Chemical Physics **23** (2021), 15702-15712.

[263] J. Yon, R. Lemaire, E. Therssen, P. Desgroux, A. Coppalle, K. Ren
Examination of wavelength dependent soot optical properties of diesel and diesel/rapeseed methyl ester mixture by extinction spectra analysis and LII measurements
Applied Physics B **104** (2011), 253-271.

[264] H. Guo, J. A. Castillo, P. B. Sunderland
Digital camera measurements of soot temperature and soot volume fraction in axisymmetric flames
Applied Optics **52** (2013), 8040-8047.

[265] C. Russo, B. Apicella, A. Tregrossi, A. Ciajolo, K. C. Le, S. Török, P.-E. Bengtsson
Optical band gap analysis of soot and organic carbon in premixed ethylene flames: Comparison of in-situ and ex-situ absorption measurements
Carbon **158** (2020), 89-96.

[266] F. P. Hagen, R. Suntz, H. Bockhorn, D. Trimis
Dual-pulse laser-induced incandescence to quantify carbon nanostructure and related soot particle properties in transient flows–Concept and exploratory study
Combustion and Flame **(In Press)** (2022), 112020.

[267] B. Ma, M. B. Long
Combined soot optical characterization using 2-D multi-angle light scattering and spectrally resolved line-of-sight attenuation and its implication on soot color-ratio pyrometry
Applied Physics B **117** (2014), 287-303.

[268] J. C. Corbin, T. J. Johnson, F. Liu, T. A. Sipkens, M. P. Johnson, P. Lobo, G. J. Smallwood
Size-dependent mass absorption cross-section of soot particles from various sources
Carbon **192** (2022).

[269] G. A. Kelesidis, C. A. Bruun, S. E. Pratsinis
The impact of organic carbon on soot light absorption
Carbon **172** (2021), 742-749.

[270] R. Dastanpour, A. Momenimovahed, K. Thomson, J. Olfert, S. Rogak
Variation of the optical properties of soot as a function of particle mass
Carbon **124** (2017), 201-211.

[271] S. D. Forestieri, T. M. Helgestad, A. T. Lambe, L. Renbaum-Wolff, D. A. Lack, P. Massoli, E. S. Cross, M. K. Dubey, C. Mazzoleni, J. S. Olfert
Measurement and modeling of the multiwavelength optical properties of uncoated flame-generated soot
Atmospheric Chemistry and Physics **18** (2018), 12141-12159.

[272] M. R. Kholghy, V. G. DeRosa
Morphology, composition and optical properties of jet engine-like soot made by a spray flame
Combustion and Flame **231** (2021), 111480.

[273] K. Wan, X. Shi, H. Wang
Quantum confinement and size resolved modeling of electronic and optical properties of small soot particles
Proceedings of the Combustion Institute **38** (2021), 1517-1524.

[274] B. Apicella, M. Alfe, R. Barbella, A. Tregrossi, A. Ciajolo
Aromatic structures of carbonaceous materials and soot inferred by spectroscopic analysis
Carbon **42** (2004), 1583-1589.

[275] A. Tregrossi, B. Apicella, A. Ciajolo, C. Russo
Fast Analysis of PAH in Complex Organic Carbon Mixtures by Reconstruction of UV-Visible Spectra
Chemical Engineering Transactions **57** (2017), 1447-1452.

[276] W. Weng, J. Borggren, B. Li, M. Aldén, Z. Li
A novel multi-jet burner for hot flue gases of wide range of temperatures and compositions for optical diagnostics of solid fuels gasification/combustion
Review of Scientific Instruments **88** (2017), 045104.

[277] Q. Wang, G. Legros, C. Morin, M. Yao, W. Cai, L. Jiang
Optical measurements of temperature fields in sooting flames: influence of soot self-absorption
Applied Physics B **125** (2019), 1-11.

[278] J. Cruz, L. F. Figueira da Silva, F. Escudero, F. Cepeda, J. Elicer-Cortés, A. Fuentes
Soot pyrometry by emission measurements at different wavelengths in laminar axisymmetric flames
Combustion Science and Technology **194** (2020), 1-18.

[279] C. F. Bohren, D. R. Huffman
Absorption and scattering of light by small particles
John Wiley & Sons, New York (2008).

[280] T. A. Sipkens
Advances in the modeling of time-resolved laser-induced incandescence
University of Waterloo (PhD thesis), (2018).

[281] T. A. Sipkens, J. Menser, T. Dreier, C. Schulz, G. J. Smallwood, K. J. Daun
Laser-induced incandescence for non-soot nanoparticles: recent trends and current challenges
Applied Physics B **128** (2022), 1-31.

[282] R. Mansmann, T. A. Sipkens, J. Menser, K. J. Daun, T. Dreier, C. Schulz
Detector calibration and measurement issues in multi-color time-resolved laser-induced incandescence
Applied Physics B **125** (2019), 1-21.

[283] H. Michelsen, C. Schulz, G. Smallwood, S. Will
Laser-induced incandescence: Particulate diagnostics for combustion, atmospheric, and industrial applications
Progress in Energy and Combustion Science **51** (2015), 2-48.

[284] E. V. Gurentsov
A review on determining the refractive index function, thermal accommodation coefficient and evaporation temperature of light-absorbing nanoparticles suspended in the gas phase using the laser-induced incandescence
Nanotechnology Reviews **7** (2018), 583-604.

[285] S. Musikhin, P. Fortugno, J. C. Corbin, G. J. Smallwood, T. Dreier, K. J. Daun, C. Schulz
Characterization of few-layer graphene aerosols by laser-induced incandescence
Carbon **167** (2020), 870-880.

[286] S. Robinson-Enebeli, S. Talebi-Moghaddam, K. J. Daun
Time-Resolved Laser-Induced Incandescence Measurements on Aerosolized Nickel Nanoparticles
The Journal of Physical Chemistry A **125** (2021), 6273-6285.

[287] T. A. Sipkens, R. Mansmann, K. J. Daun, N. Petermann, J. T. Titantah, M. Karttunen, H. Wiggers, T. Dreier, C. Schulz
In situ nanoparticle size measurements of gas-borne silicon nanoparticles by time-resolved laser-induced incandescence
Applied Physics B **116** (2014), 623-636.

[288] R. L. Vander Wal, T. M. Ticich, J. R. West
Laser-induced incandescence applied to metal nanostructures
Applied Optics **38** (1999), 5867-5879.

[289] F. Goulay, P. E. Schrader, X. López-Yglesias, H. A. Michelsen
A data set for validation of models of laser-induced incandescence from soot: temporal profiles of LII signal and particle temperature
Applied Physics B **112** (2013), 287-306.

[290] H. A. Michelsen
Laser-induced incandescence of flame-generated soot on a picosecond time scale
Applied Physics B **83** (2006), 443-448.

[291] B. Kaldvee, C. Brackmann, M. Aldén, J. Bood
LII–lidar: range-resolved backward picosecond laser-induced incandescence
Applied Physics B **115** (2014), 111-121.

[292] C. J. Dasch
Continuous-wave probe laser investigation of laser vaporization of small soot particles in a flame
Applied Optics **23** (1984), 2209-2215.

[293] S. Musikhin, R. Mansmann, G. J. Smallwood, T. Dreier, K. J. Daun, C. Schulz
Spectrally and temporally resolved LII interference emission in a laminar diffusion flame
Proceedings of the Combustion Institute - Canadian Section, Spring Technical Meeting (2019).

[294] R. Mansmann, K. Thomson, G. Smallwood, T. Dreier, C. Schulz
Sequential signal detection for high dynamic range time-resolved laser-induced incandescence
Optics Express **25** (2017), 2413-2421.

[295] S. Will, S. Schraml, A. Leipertz
Comprehensive two-dimensional soot diagnostics based on laser-induced incandescence (LII)
Symposium (International) on Combustion, (1996), 2277-2284.

[296] J. Hult, A. Omrane, J. Nygren, C. Kaminski, B. Axelsson, R. Collin, P.-E. Bengtsson, M. Aldén
Quantitative three-dimensional imaging of soot volume fraction in turbulent non-premixed flames
Experiments in Fluids **33** (2002), 265-269.

[297] M. N. Slipchenko, T. R. Meyer, S. Roy
Advances in burst-mode laser diagnostics for reacting and nonreacting flows
Proceedings of the Combustion Institute **38** (2021), 1533-1560.

[298] Z. Sun, D. Gu, G. Nathan, Z. Alwahabi, B. Dally
Single-shot, Time-Resolved planar Laser-Induced Incandescence (TiRe-LII) for soot primary particle sizing in flames
Proceedings of the Combustion Institute **35** (2015), 3673-3680.

[299] Y. Chen, E. Cenker, D. R. Richardson, S. P. Kearney, B. R. Halls, S. A. Skeen, C. R. Shaddix, D. R. Guildenbecher
Single-camera, single-shot, time-resolved laser-induced incandescence decay imaging
Optics Letters **43** (2018), 5363-5366.

[300] T. R. Meyer, B. R. Halls, N. Jiang, M. N. Slipchenko, S. Roy, J. R. Gord
High-speed, three-dimensional tomographic laser-induced incandescence imaging of soot volume fraction in turbulent flames
Optics Express **24** (2016), 29547-29555.

[301] E. M. Hall, B. R. Halls, D. R. Richardson, D. R. Guildenbecher, E. Cenker, M. Paciaroni
Tomographic Time Resolved Laser Induced Incandescence
AIAA Scitech 2020 Forum, (2020), 2209.

[302] H. A. Michelsen, P. E. Schrader, F. Goulay
Wavelength and temperature dependences of the absorption and scattering cross sections of soot
Carbon **48** (2010), 2175-2191.

[303] C. Schulz, B. F. Kock, M. Hofmann, H. Michelsen, S. Will, B. Bougie, R. Suntz, G. Smallwood
Laser-induced incandescence: recent trends and current questions
Applied Physics B **83** (2006), 333-354.

[304] D. R. Snelling, G. J. Smallwood, F. Liu, Ö. L. Gülder, W. D. Bachalo
A calibration-independent laser-induced incandescence technique for soot measurement by detecting absolute light intensity
Applied Optics **44** (2005), 6773-6785.

[305] J. Cruz, I. Verdugo, N. Gutiérrez-Cáceres, F. Escudero, R. Demarco, F. Liu, J. Yon, D. Chen, A. Fuentes
Soot Volume Fraction Measurements by Auto-Compensating Laser-Induced Incandescence in Diffusion Flames Generated by Ethylene Pool Fire
Frontiers in Mechanical Engineering **7** (2021), 744283.

[306] H. A. Michelsen, F. Liu, B. F. Kock, H. Bladh, A. Boïarciuc, M. Charwath, T. Dreier, R. Hadef, M. Hofmann, J. Reimann, S. Will, P.-E. Bengtsson, H. Bockhorn, F. Foucher, K. P. Geigle, C. Mounaim-Rousselle, C. Schulz, R. Stirn, B. Tribalet, R. Suntz
Modeling laser-induced incandescence of soot: a summary and comparison of LII models
Applied Physics B **87** (2007), 503-521.

[307] R. Puri, T. Richardson, R. Santoro, R. Dobbins
Aerosol dynamic processes of soot aggregates in a laminar ethene diffusion flame
Combustion and Flame **92** (1993), 320-333.

[308] S. A. Kuhlmann, J. Reimann, S. Will
Laserinduzierte Inkandeszenz (LII) zur Partikelgrößenbestimmung von aggregierten Rußpartikeln
Chemie Ingenieur Technik **81** (2009), 803-809.

[309] M. W. Chase Jr
NIST-JANAF thermochemical tables
Journal of Physical and Chemical Reference Data **9** (1998), 535 pp.

[310] G. J. Smallwood, D. R. Snelling, F. Liu, Ö. L. Gülder
Clouds over soot evaporation: errors in modeling laser-induced incandescence of soot
Journal of Heat Transfer **123** (2001), 814-818.

[311] H. A. Michelsen
Understanding and predicting the temporal response of laser-induced incandescence from carbonaceous particles
The Journal of Chemical Physics **118** (2003), 7012-7045.

[312] R. Lemaire, S. Menanteau
Modeling laser-induced incandescence of Diesel soot—Implementation of an advanced parameterization procedure applied to a refined LII model accounting for shielding effect and multiple scattering within aggregates for α_T and E (m) assessment
Applied Physics B **127** (2021), 1-19.

[313] J. Mitrani, M. Shneider, B. Stratton, Y. Raitses
Modeling thermionic emission from laser-heated nanoparticles
Applied Physics Letters **108** (2016), 054101.

[314] T. A. Sipkens, P. J. Hadwin, S. J. Grauer, K. J. Daun
Using Bayesian model selection and time-resolved laser-induced incandescence to probe the sublimation properties of soot
Proceedings of the Combustion Institute - Canadian Section, Spring Technical Meeting (2018).

[315] F. Memarian, F. Liu, K. Thomson, K. Daun, D. Snelling, G. Smallwood
Effect of recondensation of sublimed species on nanoparticle temperature evolution in time-resolved laser-induced incandescence
Applied Physics B **119** (2015), 607-620.

[316] S. Török, M. Mannazhi, S. Bergqvist, K. C. Le, P.-E. Bengtsson
Influence of rapid laser heating on differently matured soot with double-pulse laser-induced incandescence
Aerosol Science and Technology **56** (2022), 1-14.

[317] P. J. Hadwin, T. A. Sipkens, K. A. Thomson, F. Liu, K. J. Daun
Quantifying uncertainty in soot volume fraction estimates using Bayesian inference of auto-correlated laser-induced incandescence measurements
Applied Physics B **122** (2016), 1-16.

[318] G. A. Kelesidis, S. E. Pratsinis
Santoro flame: The volume fraction of soot accounting for its morphology & composition
Combustion and Flame **240** (2022), 112025.

[319] M. Mannazhi, S. Török, J. Gao, P.-E. Bengtsson
Soot maturity studies in methane-air diffusion flames at elevated pressures using laser-induced incandescence
Proceedings of the Combustion Institute **38** (2021), 1217-1224.

[320] V. Beyer, D. Greenhalgh
Laser induced incandescence under high vacuum conditions
Applied Physics B **83** (2006), 455-467.

[321] K. J. Daun
Thermal accommodation coefficients between polyatomic gas molecules and soot in laser-induced incandescence experiments
International Journal of Heat and Mass Transfer **52** (2009), 5081-5089.

[322] D. R. Snelling, F. Liu, G. J. Smallwood, Ö. L. Gülder
Determination of the soot absorption function and thermal accommodation coefficient using low-fluence LII in a laminar coflow ethylene diffusion flame
Combustion and Flame **136** (2004), 180-190.

[323] H. Yang, G. Song, C. J. Hogan Jr
A molecular dynamics study of collisional heat transfer to nanoclusters in the gas phase
Journal of Aerosol Science **159** (2022), 105891.

[324] J. Simonsson, A. Gunnarsson, M. N. Mannazhi, D. Bäckström, K. Andersson, P.-E. Bengtsson
In-situ soot characterization of propane flames and influence of additives in a 100 kW oxy-fuel furnace using two-dimensional laser-induced incandescence
Proceedings of the Combustion Institute **37** (2019), 833-840.

[325] N. J. Kempema, M. B. Long
Effect of soot self-absorption on color-ratio pyrometry in laminar coflow diffusion flames
Optics Letters **43** (2018), 1103-1106.

[326] F. Liu, K. A. Thomson, G. J. Smallwood
Soot temperature and volume fraction retrieval from spectrally resolved flame emission measurement in laminar axisymmetric coflow diffusion flames: Effect of self-absorption
Combustion and Flame **160** (2013), 1693-1705.

[327] S. J. Grauer, K. Mohri, T. Yu, H. Liu, W. Cai
Volumetric emission tomography for combustion processes
Progress in Energy and Combustion Science **94** (2023), 101024.

[328] R. Hadef, K. P. Geigle, J. Zerbs, R. A. Sawchuk, D. R. Snelling
The concept of 2D gated imaging for particle sizing in a laminar diffusion flame
Applied Physics B **112** (2013), 395-408.

[329] B. Tian, Y. Gao, S. Balusamy, S. Hochgreb
High spatial resolution laser cavity extinction and laser-induced incandescence in low-soot-producing flames
Applied Physics B **120** (2015), 469-487.

[330] B. Tian, C. Zhang, Y. Gao, S. Hochgreb
Planar 2-color time-resolved laser-induced incandescence measurements of soot in a diffusion flame
Aerosol Science and Technology **51** (2017), 1345-1353.

Appendix

[M1] F. J. Bauer, M. U. J. Degenkolb, F. J. T. Huber, S. Will
In situ characterisation of absorbing species in stationary premixed flat flames using UV–Vis absorption spectroscopy
Applied Physics B **127** (2021), 1-15.
https://doi.org/10.1007/s00340-021-07664-z
The author was the person mainly responsible for the study conception and design, data collection, analysis and interpretation of the results and the draft of the manuscript.

[M2] F. J. Bauer, P. A. B. Braeuer, S. Aßmann, M. A. Thiele, F. J. T. Huber, S. Will
Characterisation of the transition type in optical band gap analysis of in-flame soot
Combustion and Flame **243** (2022), 111986.
https://doi.org/10.1016/j.combustflame.2022.111986
The author was the person mainly responsible for the study conception and design, data collection, analysis and interpretation of the results and the draft of the manuscript.

[M3] F. J. Bauer, K. J. Daun, F. J. T. Huber, S. Will
Can soot primary particle size distributions be determined using laser-induced incandescence?
Applied Physics B **125** (2019), 1-15.
https://doi.org/10.1007/s00340-019-7219-7
The author was the person mainly responsible for the study conception and design, analysis and interpretation of the results and the draft of the manuscript.

[M4] F. J. Bauer, T. Yu, W. Cai, F. J. T. Huber, S. Will
Three-dimensional particle size determination in a laminar diffusion flame by tomographic laser-induced incandescence
Applied Physics B **127** (2021), 1-10.
https://doi.org/10.1007/s00340-020-07562-w
The author was the person mainly responsible for the study conception and design, data collection, analysis and interpretation of the results and the draft of the manuscript.